CFD SIMULATION OF RISER VIV

A Dissertation

by

ZHIMING HUANG

Submitted to the Office of Graduate Studies of
Texas A&M University
in partial fulfillment of the requirements for the degree of

DOCTOR OF PHILOSOPHY

May 2011

Major Subject: Ocean Engineering

CFD Simulation of Riser VIV

CFD SIMULATION OF RISER VIV

A Dissertation

by

ZHIMING HUANG

Submitted to the Office of Graduate Studies of
Texas A&M University
in partial fulfillment of the requirements for the degree of

DOCTOR OF PHILOSOPHY

Approved by:

Chair of Committee,	Hamn-Ching Chen
Committee Members,	Richard S. Mercier
	Kuang-An Chang
	Jean-Luc Guermond
Head of Department,	John Niedzwecki

May 2011

Major Subject: Ocean Engineering

ABSTRACT

CFD Simulation of Riser VIV. (May 2011)

Zhiming Huang, B.S., Tsinghua University; M.S., University of Houston

Chair of Advisory Committee: Dr. Hamn-Ching Chen

The dissertation presents a CFD approach for 3D simulation of long risers. Long riser VIV simulation is at the frontier of the CFD research area due to its high demand on computational resources and techniques. It also has broad practical application potentials, especially in the oil and gas industry. In this dissertation, I used a time domain simulation program - Finite-Analytic Navier-Stokes (FANS) code to achieve the 3D simulations of riser VIV.

First, I developed a riser modal motion solver and a direct integration solver to calculate riser dynamic motions when subject to external forces. The direct integration solver provides good flexibility on inclusion of riser bending stiffness and structural damping coefficients. I also developed a static catenary riser solver based on trial and error iteration technique, which allowed the motion solvers to handle catenary risers and jumpers with arbitrary mass distribution. I then integrated the riser motion solvers to the existing FANS code, and applied the CFD approach to a series of riser VIV problems including a 2D fixed/vibrating riser, a 3D vertical riser in uniform and shear currents, a 3D horizontal riser in uniform and shear current, a hypothetic 3,000 ft marine top tensioned riser in uniform current, a practical 1,100m flexible catenary riser in uniform

current, and a hypothetic 265m flexible jumper partially submerged in uniform current. I developed a VIV induced fatigue calculation module based on rain flow counting technique and S-N curve method. I also developed a modal extraction module based on the least squares method. The VIV details, including flow field vorticities, rms a/D, riser motion trajectories, PSDs, modal components, VIV induced stress characteristics, and VIV induced fatigue damages were studied and compared to the published experimental data and results calculated using other commercial software tools. I concluded that the CFD approach is valid for VIV simulations in 3D. I found that the long riser VIV response shows complex behaviors, which suggests further investigation on the lock-in phenomenon, high harmonics response, and sensitivity to the lateral deflections.

DEDICATION

The dissertation is dedicated to my wife Tracy Hou who has supported me all the way since the beginning of this research work.

Also, this dissertation is dedicated to my daughter Chloe Huang who has been a great source of inspiration.

ACKNOWLEDGEMENTS

I would like to thank my committee chair, Dr. Chen, and my committee members, Dr. Mercier, Dr. Chang, and Dr. Guermond, for their guidance and support throughout the course of this research.

Thanks also go to my friends and colleagues and the department faculty and staff for making my time at Texas A&M University a great experience. I also want to extend my gratitude to the Department of Interior, Minerals Management Service (MMS), Offshore Technology Research Center (OTRC), and American Bureau of Shipping (ABS) for their kind funding of this research work.

Finally, thanks to my mother and father for their encouragement and to my wife for her patience and love.

NOMENCLATURE

2D	2-Dimension
3D	3-Dimension
a	VIV Response Amplitude
α_i	Modal Component Corresponding to the i^{th} Mode
C_a	Added Mass Coefficient
C_d	Drag Coefficient
CF	Cross-Flow
CFD	Computational Fluid Dynamics
C_L	Lift Coefficient
D	Riser Diameter
D_o	Pipe Outer Diameter
D_s	Riser Structural Damping Coefficient
E	Riser Pipe Young's Modulus
f_{z0}	The Mean Zero-Up-Crossing Frequency
h	Riser Mesh Length
I	Riser Sectional Moment of Inertia
IL	In-Line
ξ^0	Initial Error for Numerical Scheme Stability Check
ξ_i	Riser Modal Shape Function Corresponding to the i^{th} Mode
L	Riser Overall Length

m	Riser Unit Mass
N	Riser Mesh Total Element Number
PSD	Power Spectral Density
ρ	Fluid Density
rms	Root-Mean-Square
Re	Reynolds Number
θ	Riser Declination Angle
τ	Simulation Time Step
T	Riser Effective Tension
U	Current Velocity
U_1	Current Velocity at Riser 1st End
U_2	Current Velocity at Riser 2nd End
U_{max}	Maximum Current Velocity
VIV	Vortex Induced Vibration

TABLE OF CONTENTS

CHAPTER Page

CHAPTER Page

LIST OF FIGURES

Page

Page

Page

Page

Page

Page

Page

Page

LIST OF TABLES

Page

CHAPTER I

INTRODUCTION AND LITERATURE REVIEW

Deepwater oil and gas exploration and developments have been moving fast toward increasingly deeper water depth, i.e. 3,000m in Gulf of Mexico. Majority of the subsea wells are tied back to a surface platform through long risers, including steel catenary risers, flexible risers, free standing risers, bundled risers, or top tensioned risers (ASME B31.4, 2002, ASME B31.8a, 2001, API 1111, 1999). These risers provide fluid conduit for fluid transport between subsea wells and surface platform, and protect the environment from reservoir fluid exposure. Many offshore facilities are designed for a service life up to 30 years, including the riser systems. For riser system fatigue design, one of the challenging areas is the VIV induced fatigue excited by ocean current flow. Usually riser VIV is in high frequency range (~1Hz) comparing to the wave induced dynamics (~0.1Hz). And it is one of the main sources of fatigue damage for the marine riser design. Although the VIV could be suppressed by strakes or fairings, the cost associated with the hardware and installation is high. Therefore, the research interest on the riser VIV has been growing in the oil and gas industry to achieve safe and economical design.

This dissertation follows the style of *Journal of Offshore Mechanics and Arctic Engineering*.

The oil and gas industry has been heavily relying on the experimental data for riser VIV design. During the last several years many VIV experiments have been carried out on deepwater risers with large L/D, and the related publications are numerous. The Norwegian Deepwater Program measured on a 38 m (L/D=1,400) long riser model for various linearly shear and uniform flow velocity cases corresponding to bare and straked riser configurations, and the experimental results are discussed in Trim et al. (2005). British Petroleum measured the VIV of a drilling riser under different riser conditions, such as drilling, hung-off rig move, and connected non-drilling. The experiments were conducted in the Gulf of Mexico in various water depths from 1,182 ft (L/D=300) to 6,800 ft (L/D=1,700) (Tognarelli et al. 2008). Deepstar JIP also carried out VIV experiments in Gulf Stream in 2006. The experiments were done on a 500 ft long and 1.43 in. diameter (L/D=4,200) pipe with and without strakes. Part of the experimental results was discussed by Vandiver et al. (2006) and Jhingran et al. (2008). In April of 2008, selected results of the above VIV experiments were released to the public and hosted on web site oe.mit.edu/VIV/, along with some data sets donated by several others, including two sets donated by ExxonMobil measured on a 10 m riser model with and without strakes, and for various linearly shear and uniform flow velocity cases.

However, experiment has limitations as well, such as facility availability and capacity limits, model scale limit, difficulty of current profile generation, cost concerns, etc. Under such condition, software and computer models have been developed to meet this need. Some software tools were developed based on experimental data and empirical formula. These tools used model superposition approach, and the modal responses were

partially or fully based on the test data. Other tools were based on CFD simulation approach. Some of the popular tools for riser VIV prediction were discussed by Chaplin et al. (2005).

As a trend in recent years, the CFD approach received more and more attention due to the ever-improving computational capability, i.e. computer speed and storage space. Furthermore, the CFD approach also provides flow field and riser motion details that are essential to understand the VIV phenomena, and is regarded as a valuable compensation and good alternative to water basin experiments.

The application of the 3D CFD approach to cylinder VIV study is still a relatively new research area due to its onerous computational requirement. Some early work can be traced back to 1996. Newman and Karniadakis (1996) presented a 3D CFD simulation of flexible cable VIV with aspect ratio (L/D) of 45, and low Reynolds number (~300). Lucor et al. (2000) presented simulation results of a flexible cable with aspect ratio of 500, and Reynolds number of 10^3. Willden & Graham et al. (2001) also published the simulation results of VIV simulation of a flexible cylinder with aspect ratio of 100, and Reynolds number of 300. Yamamoto et al (2004) simulated the VIV of a 120 m marine riser with aspect ratio of 500, and Reynolds number $2x10^5$. Meneghini et al. (2004) used two-dimensional discrete vortex method (DVM) to simulate long marine risers with L/D up to 4,600. Pontaza, Chen & Chen (2006, 2007a, 2007b) presented simulations of riser VIV with aspect ratio of 20, and Reynolds number up to 10^7. Holmes & Oakley et al. (2006) simulated VIV of a long riser with aspect ratio of 1,400, and Reynolds number of 10^4. They used unstructured data grid consisting of 10 million finite

elements. Constantinides and Oakley (2008a, 2008b) also presented the VIV simulations of long cylinders with L/D=4,200. The prospect of increasing need for CFD simulation has also attracted some commercial FEA software vendors. Chen and Kim (2010) presented simulation results obtained through ANSYS MFX package, a newly released feature by the ANSYS Inc. And Chen et al. studied the VIV of a vertical riser with aspect ratio of 500, and Reynolds number of 10^4. In summary, the available publications showed the latest research on CFD simulation of long riser VIV is mainly in three areas:

1. Quasi-3D or strip theory. In this approach the CFD simulation is down graded to 2D strips, and the fluid field on each strip is independent of each other. The advantage is that the data grids are in 2D and compatible with many existing turbulence models. The vortex shedding in 2D planes could be simulated in good resolution with relatively less elements. The disadvantage is the fluid fields on different plane are not coupled, and riser spanwise vorticity has been ignored.
2. Full 3D with unstructured data grid. In this approach the fluid field is discretised by 3D elements. The advantage is that the fluid field is solved in 3D and riser spanwise flow could be captured in detail. The disadvantage is that it requires significantly more elements near the riser surface to achieve good resolution for turbulence model. Consequently the computational effort could be tremendous even with the fastest computer to date. When riser has large deflection, the data grid could be highly distorted to accommodate the relative riser movement. This would compromise its validity for large riser

deflection situations, which are fairly common in the physical world, especially in deepwater applications.

3. Full 3D with structured data grid. First, it is a full 3D approach. The flow field around the riser is calculated by numerically solving the unsteady, incompressible 3D Reynolds-Averaged Navier-Stokes (RANS) in conjunction with a large eddy simulation (LES) model (Pontaza et al. 2004, 2005a, 2005b, 2005c). The governing equations are transformed from physical space (x,y,z) into numerical space (ξ,η,γ). The continuity equation is then solved by a finite-volume scheme. The transport equations are solved by the finite-analytic method of Chen et al. (1990) assuming the pressure field is known. The pressure is then updated by a hybrid PISO/SIMPLER algorithm (Chen & Patel, 1988, 1989). Second, it uses structured data grid, which possesses all advantages of the strip theory. Particularly, the Chimera technique could be applied to allow for data grid overset. The Chimera technique is well suited for CFD involving moving objects such as risers. A very fine data grid (body grid) is attached to the riser and on top of a relatively coarse grid (wake or background grid). When riser moves, the body grid moves relative to the background grid. The data consistency between the body grid and the background grid on the overlapped region is enforced by data interpolation. Theoretically the data grids can be overlapped and nested as many levels as possible. In some of our studies we added an intermediate data grid (wake grid) to resolve the vortex shedding and traveling. By using

the Chimera technique, the data grids can be generated with great attention to the details, such as the regions near the riser surface and vortex shedding and traveling area, yet without worrying about the re-generation of data grid at each time step when the riser moves.

The objective of this dissertation is to further develop the 3rd approach (FANS code), and extend the capability of the existing code from 2D and 3D with short L/D to 3D with large L/D, with Reynolds number up to $1.5x10^5$. The research scope of work includes the following tasks:

1. Development of CFD capabilities: riser motion modal solver.
2. Development of CFD capabilities: riser motion direct integration solver.
3. Development of fatigue calculation capabilities: riser VIV induced fatigue calculation module.
4. Development of a riser catenary static solver for arbitrary weight distribution using a trial and error method.
5. Development of a riser modal extraction module using the least squares method.
6. 2D simulations of flow past a fixed riser at high Reynolds numbers ($Re=3x10^5$).
7. 2D simulations of flow past a forced motion riser at high Reynolds numbers ($Re=3x10^5$).
8. 3D simulations of flow past a vertically positioned riser in uniform current ($L/D=480$, $Re=1.5x10^4$).

9. 3D simulations of flow past a vertically positioned riser in shear current (L/D=480, Re=$1.5x10^4$).
10. 3D simulations of flow past a horizontally positioned riser in uniform current (L/D=1,400, Re=$1.7x10^4$).
11. 3D simulations of flow past a horizontally positioned riser in shear current (L/D=1,400, Re=$1.7x10^4$).
12. 3D simulations of flow past a vertically positioned riser in uniform current (L/D=3,350, Re=$8x10^4$).
13. 3D simulations of flow past a catenary riser in uniform current (L/D=3,300, Re=$1.1x10^5$).
14. 3D simulations of flow past a catenary, partially submerged jumper in uniform current (L/D=800, Re=$1.5x10^5$).

The simulation results were compared to the published experimental data, and/or the results calculated using other commercial software tools.

CHAPTER II

VIV SIMULATION TECHNIQUES

This Chapter describes the numerical approach used for the riser VIV simulations, and additional techniques developed throughout the research and case studies.

Numerical Approach

The numerical approach we adopted is a time domain simulation code - Finite-Analytic Navier-Stokes (FANS) code. It has been previously validated through various applications (Pontaza, Chen & Chen, 2004, 2005a, 2005b; Pontaza, Chen & Reddy, 2005; Pontaza & Chen 2006) on 2D riser VIV simulations and 3D rigid riser VIV simulations. The flow field around a riser is calculated by numerically solving the unsteady, incompressible Navier-Stokes equations. The turbulent flow was solved using Large Eddy Simulation (LES):

$$\frac{\partial \overline{u}_i}{\partial t} + \frac{\partial}{\partial x_j}\left(\overline{u}_i \overline{u}_j\right) = -\frac{1}{\rho}\frac{\partial \overline{p}}{\partial x_i} + \nu \frac{\partial^2 \overline{u}_i}{\partial x_j \partial x_j} - \frac{\partial \tau_{ij}}{\partial x_i} \quad , \tag{1}$$

where the subgrid stresses are given by

$$\tau_{ij} = \overline{u_i u_j} - \overline{u}_i \overline{u}_j \, ,$$

with the Smagorinsky subgrid-scale turbulence model:

$$\tau_{ij} = -2\nu_T \overline{S}_{ij} \, ,$$

$$\nu_T = \left(C_S \Delta\right)^2 \sqrt{2\overline{S}_{ij}\overline{S}_{ij}} \, ,$$

The local strain rate tensor $\overline{S}_{ij}$ is defined as

$$\overline{S}_{ij} = \frac{1}{2}\left(\frac{\partial \overline{u}_i}{\partial x_j} + \frac{\partial \overline{u}_j}{\partial x_i} \right) \quad ,$$

and the filter-width is taken as the local grid size, i.e.

$$\Delta = \left(\Delta_x \Delta_y \Delta_z \right)^{1/3} \quad .$$

The Smagorinsky coefficient C_S is chosen as 0.1. No damping is included in this model. Refer to Chen et al. (2006) for more details.

The formulation is fully 3D without omitting any terms in the Navier-Stokes equations. Therefore, it is not the same as 2D strip theory, which assumes that the flow is purely two-dimensional without spanwise correlation. To limit the computational effort, we used relatively coarse grids in spanwise direction. As a result, the flow in the spanwise direction is "under-resolved". The effect of the spanwise velocity correlations has been studied in Pontaza and Chen (2006) on a short cylinder with sufficiently fine mesh in the spanwise direction. Nevertheless, we were able to predict the riser motion responses with reasonable accuracy and will leave the further improvement in spanwise grid resolution to future investigations.

The overset grid (Chimera) technique is used to handle the riser movement and grid overlapping. We adopted fine meshes on the riser cross-sectional planes and coarse meshes in the riser spanwise direction. This would reduce the total element number and the computational effort. The coordinate system is selected as (unless otherwise noted in the content): x direction coincides with riser axis, y is in the flow direction, and z is the cross flow direction. The data grid system consists of three sets (or two sets when the

background grid is not used) of data grids and has a total of less than 1.5 million grid nodes. The three sets of data grids are: (1) body grid – the data grid adjacent to the riser surface that provides fine resolution to calculate the fluid-riser surface interaction and vortex generation, (2) wake grid – it interfaces with body grid and background grid and provides good resolution for vortex propagation, (3) background grid – as the name suggests, it defines the outer boundary of the computational fluid domain, provides the far field fluid boundary conditions, interfaces with and provides a physical extension to the wake grid using relatively coarse mesh. The data grid sizes are different for each simulation, and more details are presented in the simulation result sections. When the riser vibrates, the data grids also move with the riser so there is no gap between the riser and the grids at any time.

The riser has various length and diameter, depending on the load case definitions. During the simulations, the drag (C_d) and lift (C_L) coefficients are calculated along the riser at each time step. The riser is descritized using fine segments (usually 250 to 500 segments – a typical range for riser global dynamic analysis). Its two ends are pinned to the ground with zero rotational stiffness. Then the riser motions are solved by a motion solver (either the modal solver or the direct integration solver) assuming that the drag and lift force variation is negligible at each time step. This is an explicit approach without iteration between the flow field and the riser motion. When the VIV response dominant modes are not very high (~ 1Hz), the riser bending stiffness should not impact the VIV response. However, the riser direct integration motion solver allows for

inclusion of the bending stiffness, and structural damping as well. Fig. 1 shows the time domain simulation procedures.

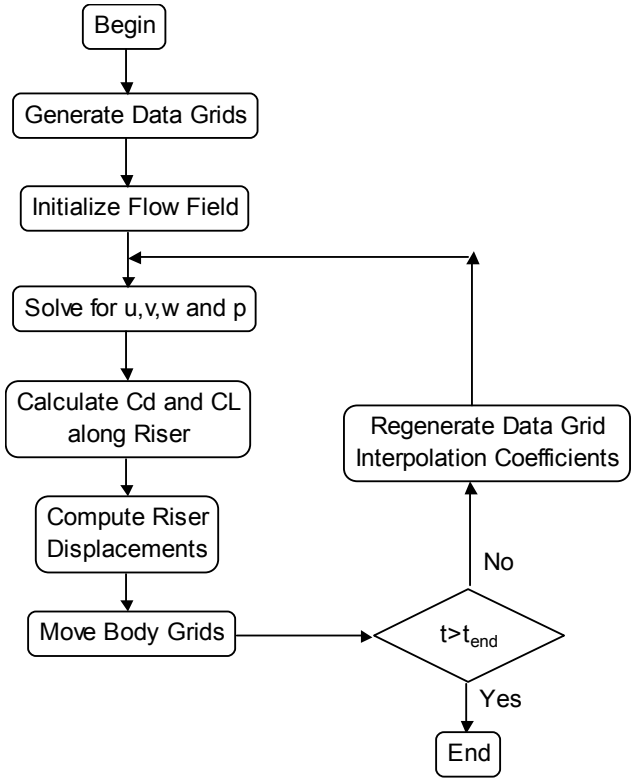

Fig. 1 CFD Simulation Procedures

Riser Motion Modal Solver

For a tensioned beam, the motion equation is expressed as Eq. (2):

$$T\frac{d^2y}{dx^2}+\frac{dy}{dx}\frac{dT}{dx}-\frac{d^2}{dx^2}\left(EI\frac{d^2y}{dx^2}\right)+f_y=m\ddot{y}+D_s\dot{y} \quad , \tag{2}$$

where T is the effective tension, EI is the bending stiffness, f_y is the external force, m is the unit mass of the riser, and x is the riser axial direction, y is perpendicular to the riser. Note that the riser motion in z direction is similar to Eq. (2) by replacing the y with z. Therefore the derivation in z direction is not repeated. When the riser is positioned horizontally, or the tension variation along the riser is small, we have $\frac{dT}{dx}\approx 0$. Because the riser is relatively long (L/D~10^2), the effect of EI is negligible. Therefore, the Eq. (2) is simplified as Eq. (3):

$$T\frac{d^2y}{dx^2}+f_y=m\ddot{y} \quad . \tag{3}$$

Express y as the superposition of the modal shapes, or

$$y(x,t)=\sum_i \alpha_i(t)\xi_i(x) \quad , \tag{4}$$

where α_i is the modal coefficient, and ξ_i is the modal shape, which is given by Eq. (5) for pinned boundary condition at both riser top and bottom.

$$\xi_i(x)=\sin\frac{i\pi\cdot x}{L}=\sin\lambda_i x \quad , \tag{5}$$

Substitute Eq. (4) into Eq. (3), and take inner product to ξ_j, note that $\langle\xi_i * \xi_j\rangle$=0 for $i\neq j$, and $\xi_i''=-\lambda_i^2\xi_i$, we have Eq. (6):

$$m\alpha_j'' + T\lambda_j^2\alpha_j = \frac{\langle f_y * \xi_j \rangle}{\|\xi_j\|^2} \quad , \tag{6}$$

where m is the modal mass, $T\lambda_j^2$ is the modal stiffness, and RHS is the modal excitation force. The natural periods are $\omega_j = \sqrt{\frac{T\lambda_j^2}{m}} = j\pi\sqrt{\frac{T}{mL^2}}$, which is the standard solution of a taut string.

Once we have f_y at each time step, the modal coefficient α_j could be solved using Eq. (6). The lateral displacement $y(x,t)$ is then calculated through modal superposition. Note that the RHS of the Eq. (6) will be integrated in y and z direction separately to give modal excitation forces in the in-line and cross flow directions. Hence Eq. (6) is solved in both y and z directions individually for the modal responses in in-line and cross flow directions. No artificial or structural damping is included, although they can be included by adding a damping term to Eq. (2) and following the same procedures to derive the equivalent form of Eq. (6).

We used the 4th order Runge-Kutta method to integrate equation (5). This scheme is explicit and stable for small time step integrations ($\Delta t = \tau \le \frac{mL^2}{i^2\pi T}$).

Riser Motion Direct Integration Solver

The tensioned beam equation can also be solved through a finite difference scheme with direct integration at each time step. Notice that Eq. (2) is a parabolic system of PDEs, with fourth order derivative in space and second order derivative in time. We select the finite difference scheme of each term in Eq. (2) as:

$$\frac{d^2y}{dx^2} = \frac{y_{j+1}^n - 2y_j^n + y_{j-1}^n}{h^2}, \text{ for j=2..N-1, and } \frac{d^2y}{dx^2} = \frac{y_{j+2}^n - 2y_{j+1}^n + y_j^n}{h^2}, \text{ for j=1,}$$

$$\frac{d^2y}{dx^2} = \frac{y_j^n - 2y_{j-1}^n + y_{j-2}^n}{h^2}, \text{ for j=N,} \tag{7}$$

$$\frac{dy}{dx} = \frac{y_{j+1}^n - y_{j-1}^n}{2h}, \text{ for j=2..N-1, and } \frac{dy}{dx} = \frac{-3y_j^n + 4y_{j+1}^n - y_{j+2}^n}{2h}, \text{ for j=1}$$

$$\frac{dy}{dx} = \frac{y_{j-2}^n - 4y_{j-1}^n + 3y_j^n}{2h}, \text{ for j=N,} \tag{8}$$

$$\frac{d^4y}{dx^4} = \frac{y_{j+2}^n - 4y_{j+1}^n + 6y_j^n - 4y_{j-1}^n + y_{j-2}^n}{h^4}, \text{ for j=3..N-2,}$$

$$\frac{d^4x}{dz^4} = \frac{x_{j+3}^n - 4x_{j+2}^n + 6x_{j+1}^n - 4x_j^n + x_{j-1}^n}{h^4}, \text{ for j=2,}$$

$$\frac{d^4y}{dx^4} = \frac{y_{j-3}^n - 4y_{j-2}^n + 6y_{j-1}^n - 4y_j^n + y_{j+1}^n}{h^4}, \text{ for j=N-1,}$$

$$\frac{d^4y}{dx^4} = \frac{y_{j+4}^n - 4y_{j+3}^n + 6y_{j+2}^n - 4y_{j+1}^n + y_j^n}{h^4}, \text{ for j=1,}$$

$$\frac{d^4y}{dx^4} = \frac{y_{j-4}^n - 4y_{j-3}^n + 6y_{j-2}^n - 4y_{j-1}^n + y_j^n}{h^4}, \text{ for j=N,} \tag{9}$$

$$\frac{d^2y}{dt^2} = \frac{y_j^n - 2y_j^{n-1} + y_j^{n-2}}{\tau^2}, \text{ for n>=3,} \tag{10}$$

$$\frac{dy}{dt} = \frac{y_j^n - y_j^{n-1}}{\tau}, \text{ for n>=2,} \tag{11}$$

Initial conditions are set as $y_j^1 = y_j^2 = 0$, j=1..N. Assume *EI* is constant, $w = \frac{dT}{dx}$, and assemble Eqs (7) to (11), we have the discretized governing Eq. (12)

$$\begin{aligned} &\frac{EI}{h^4} y_{j-2}^n - \left(\frac{T_j}{h^2} - \frac{w_j}{2h} + \frac{4EI}{h^4}\right) y_{j-1}^n + \left(\frac{2T_j}{h^2} + \frac{6EI}{h^4} + \frac{m}{\tau^2} + \frac{D_s}{\tau}\right) y_j^n \\ &- \left(\frac{T_j}{h^2} + \frac{w_j}{2h} + \frac{4EI}{h^4}\right) y_{j+1}^n + \frac{EI}{h^4} y_{j+2}^n = RHS_j^n \end{aligned}, \tag{12}$$

where $RHS_j^n = f_{xj}^n + \left(\frac{2m}{\tau^2} + \frac{D_s}{\tau}\right) y_j^{n-1} - \frac{m}{\tau^2} y_j^{n-2}$, h is the riser segment length, and τ is the time step. Note that this is an implicit scheme. Its matrix dimension is *N* x *N*, and can be solved by LU decomposition method. The same discretization scheme is also used to solve for the riser cross flow motion in z-direction.

At each time step, the pressure and viscous force on the riser surface are integrated circumferentially and mapped to the riser structural elements. The riser in-line and cross flow motions are then calculated and fed back to the body grid as boundary conditions. The riser is typically discretized into 250 to 500 structural elements. If the riser has constant sectional properties then the element sizes will be uniform through out the riser string. It is worth noting that this method is a linearized motion solver with consideration that the riser VIV is usually in the order of several diameters. The riser motions are solved in in-line and cross flow directions separately.

Numerical Scheme Stability Check

The stability of the numerical scheme is checked through von Neumann method. The stability check considers only the finite difference solution of the structural response, and does not include the fluid structure interaction. With an initial error vector ξ^0, the error distribution at time step *n* and node *j* is expressed as $\xi_j^n = (G)^n e^{i\theta j}$, where $\theta = k\pi\Delta y$. Substitute it to Eq. (13), we have

$$\frac{EI}{h^4}(G)^n e^{i\theta(j-2)} - \left(\frac{T_j}{h^2} - \frac{w_j}{2h} + \frac{4EI}{h^4}\right)(G)^n e^{i\theta(j-1)} + \left(\frac{2T_j}{h^2} + \frac{6EI}{h^4} + \frac{m}{\tau^2} + \frac{D_s}{\tau}\right)(G)^n e^{i\theta j} - \left(\frac{T_j}{h^2} + \frac{w_j}{2h} + \frac{4EI}{h^4}\right)(G)^n e^{i\theta(j+1)} + \frac{EI}{h^4}(G)^n e^{i\theta(j+2)} = \left(\frac{2m}{\tau^2} + \frac{D_s}{\tau}\right)(G)^{n-1} e^{i\theta j} - \frac{m}{\tau^2}(G)^{n-2} e^{i\theta j}, \quad (13)$$

Dividing both sides of Eq. (13) by $\frac{m}{\tau^2} G^n e^{i\theta \cdot j}$, and let

$$A = \frac{EI\tau^2}{mh^4} 2\cos(2\theta) - \left(\frac{T_j\tau^2}{mh^2} + \frac{4EI\tau^2}{mh^4}\right) 2\cos(\theta) + \left(\frac{2T_j\tau^2}{mh^2} + \frac{6EI\tau^2}{mh^4} + 1 + \frac{D_s\tau}{m}\right) - i\left(\frac{w_j\tau^2}{2mh}\right) 2\sin(\theta),$$

$$B = -\left(2 + \frac{D_s\tau}{m}\right),$$

$$C = 1,$$

Eq. (13) is simplified as $A * G^2 + B * G + C = 0$, and the amplification factor *G* is given by:

$$G_{1,2} = \frac{-B \pm \sqrt{B^2 - 4AC}}{2A}.$$

For the special case of $D_s = 0$ and $w = 0$ (i.e., T_j = const), the present numerical scheme is unconditionally stable with $\left|G_{1,2}\right| = \frac{1}{\sqrt{1+\alpha+\beta}} < 1$, where $\alpha = \frac{16EI\tau^2}{mh^4}\sin^4\frac{\theta}{2}$ and $\beta = \frac{4T\tau^2}{mh^2}\sin^2\frac{\theta}{2}$. The inclusion of damping term $\delta = \frac{D_s\tau}{m}$ usually improves the numerical stability. It can be shown analytically that $-1 \le G_{1,2} = \frac{(2+\delta) \pm \sqrt{\delta^2 - 4(\alpha+\beta)}}{2(1+\alpha+\beta+\delta)} \le 1$ for all combinations of α, β and δ as given below:

$$\begin{cases} \left|G_{1,2}\right| = \dfrac{1}{\sqrt{1+\alpha+\beta+\delta}} < 1, & if \quad \delta^2 - 4(\alpha+\beta) < 0 \\ 0 \le \dfrac{1}{1+\alpha+\beta+\delta} \le G_{1,2} \le \dfrac{1+\delta}{1+\alpha+\beta+\delta} \le 1, & if \quad \delta^2 - 4(\alpha+\beta) \ge 0 \end{cases}.$$

Therefore, Eq. (13) is unconditionally stable. For illustration purpose, a typical 0.273 m (10.75 in) production riser for 900 m (3,000 ft) water depth is used for the von Neumann stability check. It has uniform mass of 180 kg/m (121 lb/ft), mean tension of 500 kN. It is discretized by 250 elements and with simulation time step τ=0.007 s. Fig. 2 shows the von Neumann stability under different bending to tension ratios. The higher the bending stiffness, the better the stability. Fig. 3 shows the von Neumann stability under different damping coefficients. In this case the bending was set to zero (EI=0). It indicates that the damping has limited effect on the stability of the numerical scheme.

A riser motion solver is then established based on this numerical difference scheme to predict the riser dynamic motions during VIV simulations.

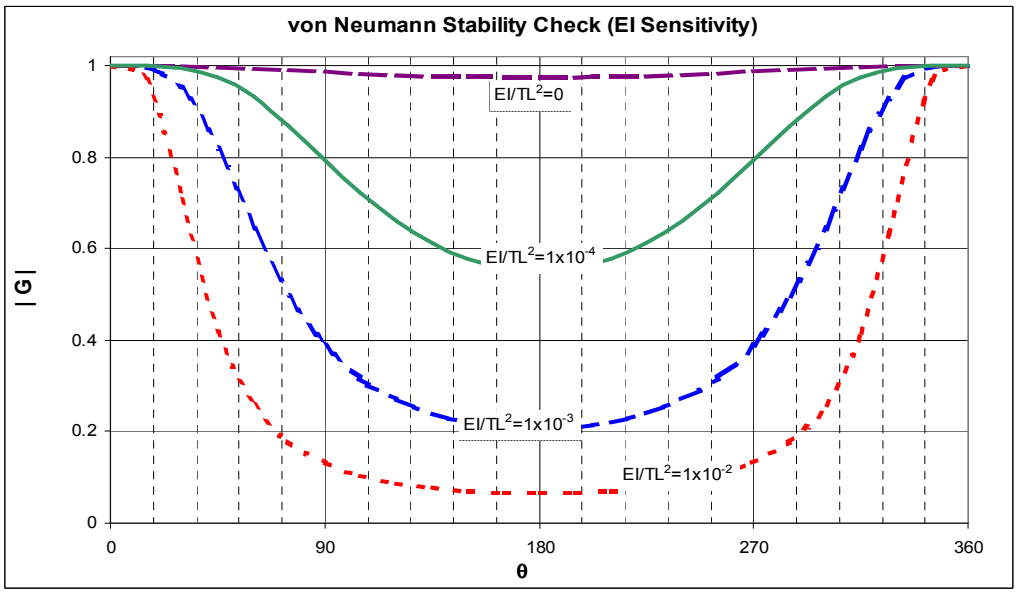

Fig. 2 von Neumann Stability Check (*EI* Sensitivity)

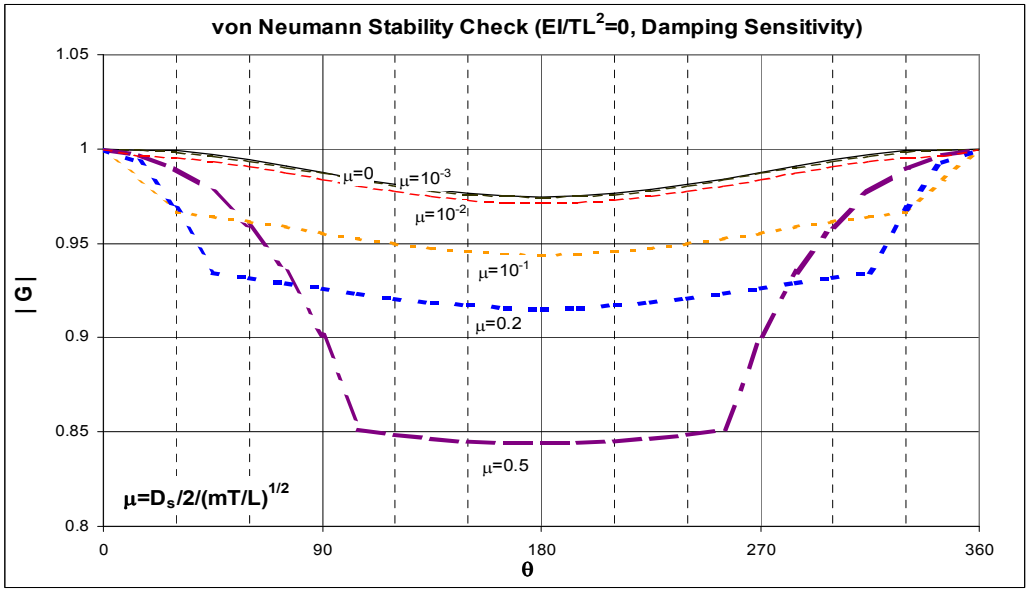

Fig. 3 von Neumann Stability Check (Damping Sensitivity)

Motion Solver Static Case Validation

The riser motion solver is applied to solve for the riser deflection under constant loads. Two cases were checked against the theoretical solution: (1) a 0.273 m (10.75 in) riser with constant tension, (2) a 0.273 m (10.75 in) riser with linearly varying tension distribution. In the reality the top tensioned risers have the highest tension at the top, and lowest tension at the bottom due to its own submerged weight. The results are shown in Figs. 4 and 5 for these two cases respectively. For the constant tension case, the riser deflection is symmetric and the maximum riser deflection occurs in the middle of the riser string. However, for the varying tension case, the riser deflection is not symmetric and the maximum riser deflection occurs in the lower portion of the riser. The comparisons in both cases show exact match between motion solver and theoretical solution.

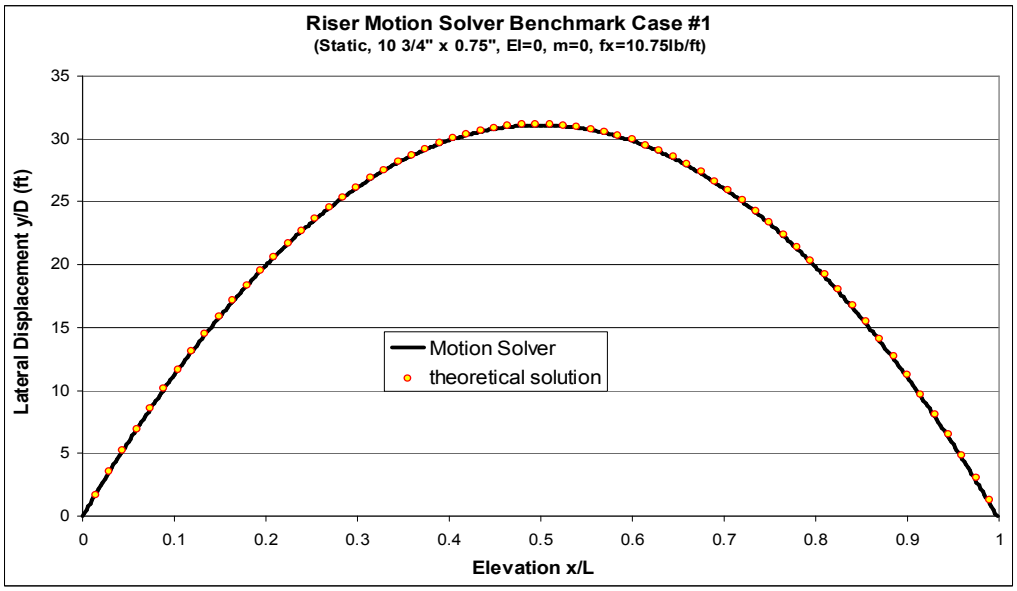

Fig. 4 Riser Static Displacement Comparison (Riser Constant Tension)

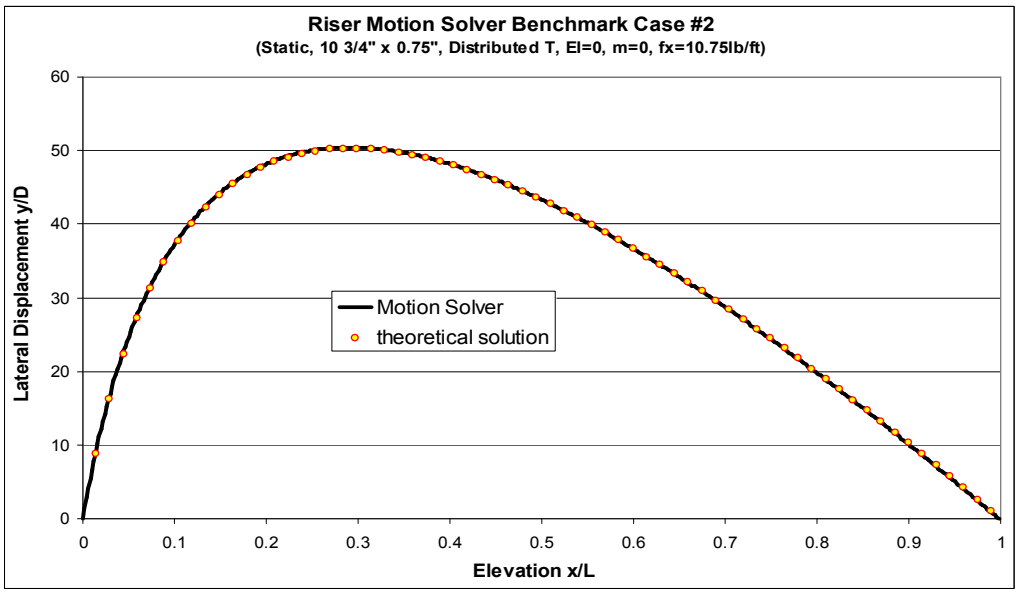

Fig. 5 Riser Static Displacement Comparison (Varying Tension)

Motion Solver Dynamic Case Validation

When the riser is suddenly subject to a uniform load, it will start to move and vibrate until its energy dissipates completely. Fig. 6 shows the vibrating time history at location x/L=1/3, where the maximum riser deflection occurs. Typical structural damping coefficient of 0.3% was included. Solutions of dynamic response from the finite difference method were compared to those from a commercial finite element code (Flexcom) to test this aspect of the finite difference method. And the comparison also confirms that the riser motion solver with the proposed difference schemes is able to predict riser dynamic motions correctly.

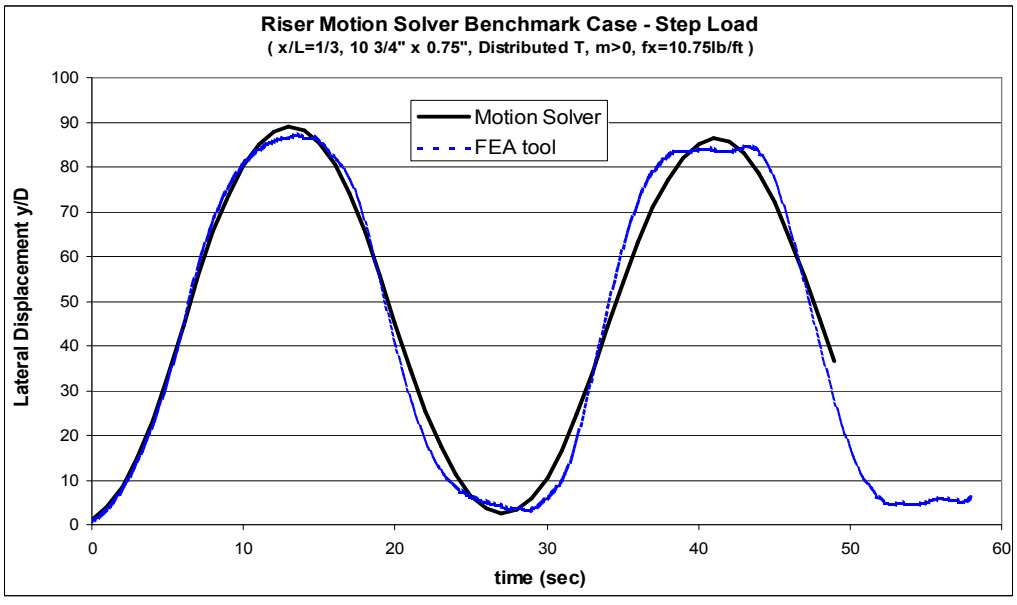

Fig. 6 Riser Dynamic Motion Comparison (Time History at x/L=1/3)

A forced vibration case was also used to check the riser motion solver. A sinusoidal motion with amplitude of two diameters and period of one second is applied to the riser top, and the riser lateral deflection time histories have been recorded and plotted. Again, these riser deflections are compared to a FEA tool, as shown in Fig. 7. It shows the riser dynamic motions are very similar.

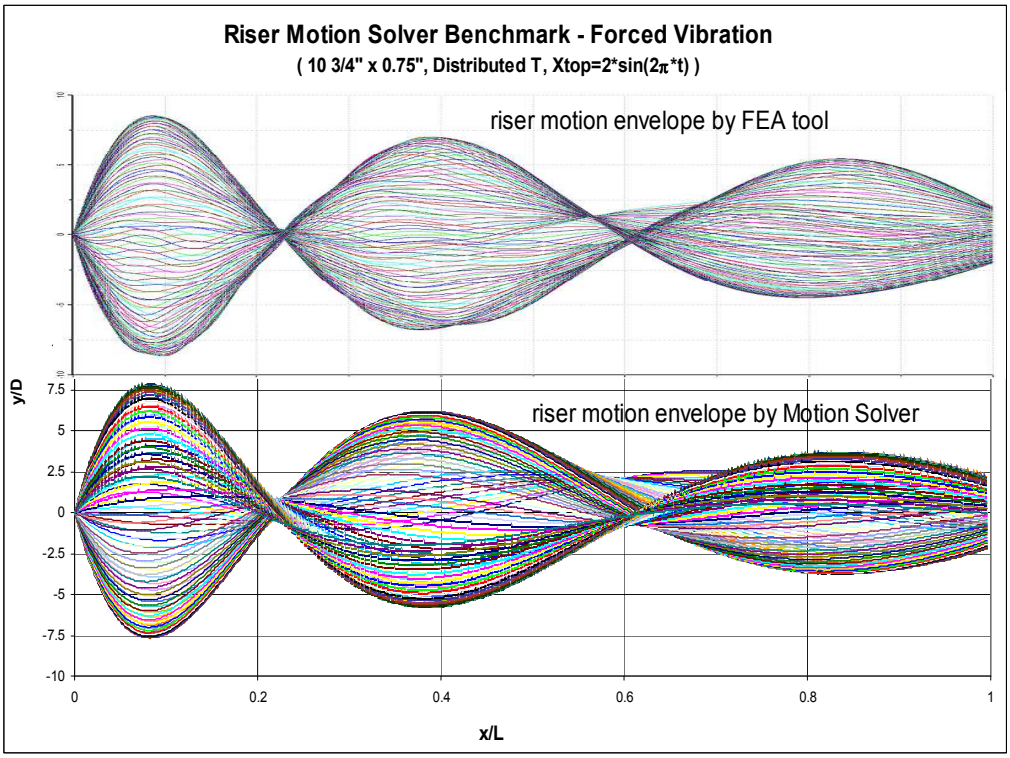

Fig. 7 Riser Dynamic Motion Comparison (Forced Vibration)

.

VIV Induced Fatigue Calculation

Riser VIV could cause large quantity of fatigue stress cycles. Although the stress includes tension induced stress from riser length variation and bending induced stress from curvature variation, usually bending induced stress is dominant. For long risers, the VIV induced bending stress at the outer diameter can be calculated as $\sigma(x,t) = \frac{ED_o}{2} y''(x,t)$, where E is the Young's modulus, D_o is the outer diameter of the riser. Therefore, the Eq (14) can be derived:

$$\sigma(x,t) = \frac{ED_o}{2} \sum_i \alpha_i \xi_i'' \quad , \tag{14}$$

where $\alpha_j(t) = \frac{\langle y(x,t) * \xi_j \rangle}{\|\xi_j\|^2}$.

There are many different ways to calculate fatigue. We adopted rain flow counting in conjunction with S-N curve approach since it is popularly used and regarded as the most accurate method. The procedures are as follows:

1. Simulate riser VIV in time domain for sufficiently long duration.
2. Calculate the curvatures at each time step for all the riser elevations.
3. Generate riser stress time histories at riser locations of interest.
4. Count the stress cycles using Rain Flow Counting techniques.
5. Accumulate the fatigue damage through Palmgren-Miner's rule and S-N curve approach.

In step 3 the stress time histories are dependent of the circumferential angle if both the in-line and cross flow VIV induced fatigue are to be considered. We calculate the in-

line and cross flow stresses first and then combine them at the riser outer diameter. An alternative method is to calculate the riser 3D curvature in step 2.

Stress Histogram Characteristics

Once the riser dynamic motions are known, the bending stress responses can be calculated from the riser curvatures. Tension stress variation is neglected since it is usually much lower than the bending stress variations. For a steady VIV response, the stress time history can be expressed as a series of sinusoidal components with modal frequencies:

$$\sigma(t) = \sum_{i=1}^{\infty} b_i \sin(i\omega \cdot t + \varphi_i) \quad , \tag{15}$$

where ω is the riser fundamental frequency, b_i and φ_i are the response amplitude and phase angle of mode i respectively.

Let's assume mode n is the most dominant mode, and rearrange Eq. (15) as:

$$\sigma(t) = \sum_{i=1}^{\infty} b_i \sin(n\omega \cdot t + (i-n)\omega \cdot t + \varphi_i) \quad . \tag{16}$$

Note that

$$\begin{aligned} &\sin(n\omega \cdot t + (i-n)\omega \cdot t + \varphi_i) = \sin(n\omega \cdot t)\cos((i-n)\omega \cdot t + \varphi_i) \\ &+ \cos(n\omega \cdot t)\sin((i-n)\omega \cdot t + \varphi_i) \end{aligned} \quad . \tag{17}$$

Substitute Eq. (17) into Eq. (16), we have

$$\sigma(t) = \sin(n\omega \cdot t)\sum_{i=1}^{\infty} b_i \cos((i-n)\omega \cdot t + \varphi_i) + \cos(n\omega \cdot t)\sum_{i=1}^{\infty} b_i \sin((i-n)\omega \cdot t + \varphi_i) \, . \tag{18}$$

During stress cycle counting, only stress peaks and troughs are needed. At the stress peaks and troughs, the stress derivatives with respect to time must be zeroes, or:

$$\frac{d\sigma(t)}{dt} = 0 \,. \tag{19}$$

Take derivative of both sides in Eq. (18), we have:

$$\frac{d\sigma(t)}{dt} = \cos(n\omega \cdot t)\sum_{i=1}^{\infty} i\omega \cdot b_i \cos((i-n)\omega \cdot t + \varphi_i) - \sin(n\omega \cdot t)\sum_{i=1}^{\infty} i\omega \cdot b_i \sin((i-n)\omega \cdot t + \varphi_i) \cdot \tag{20}$$

Combine Eqs. (19) and (20), Eq. (21) is derived finally:

$$\tan(n\omega \cdot t) = \frac{\sum_{i=1}^{\infty} i\omega \cdot b_i \cos((i-n)\omega \cdot t + \varphi_i)}{\sum_{i=1}^{\infty} i\omega \cdot b_i \sin((i-n)\omega \cdot t + \varphi_i)} \quad . \tag{21}$$

The stress peaks and troughs occur at the time steps where Eq. (21) is satisfied. As an example of the riser with L/D=1,400, assume n=4, the LHS and RHS of equation (21) are plotted in Fig. 8. It shows for each riser fundamental period, there are usually eight peaks/troughs expected. In other words, there likely exist four distinct groups of cycle ranges.

We used rain flow counting technique (Huang et al., 2008) to count the stress cycle numbers and ranges. Then the stress cycles are grouped into histograms. Fig. 9 shows the stress histograms of U=0.4m/s case at x/L=0.87. It confirmed that: (1) the stress cycle ranges are discrete, (2) if we discount the lowest stress range since it stands alone, the stress histogram consists of four distinct groups, which is what we expected from Fig. 8.

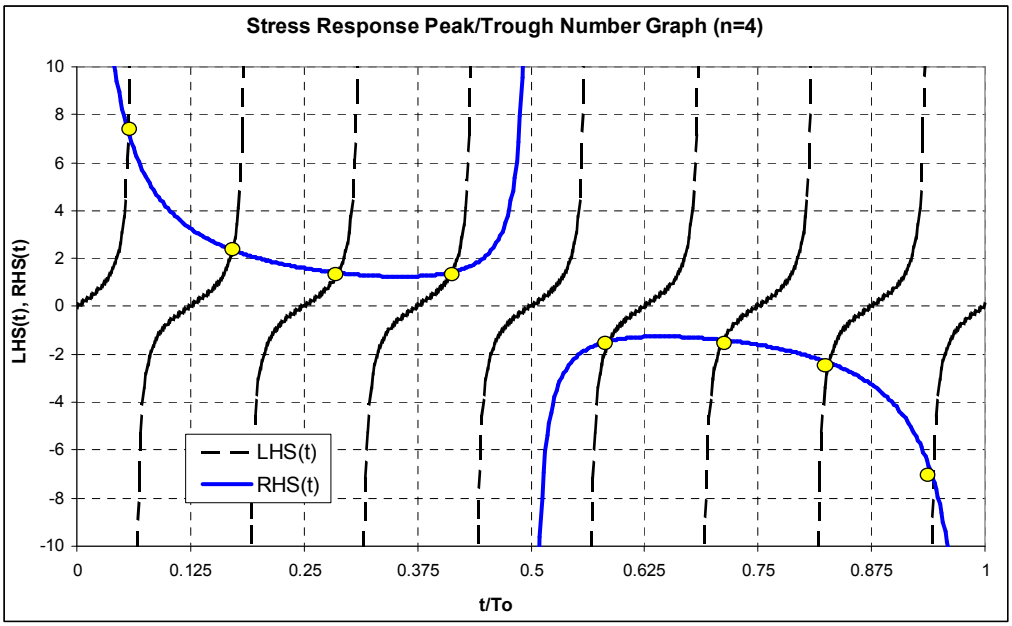

Fig. 8 Distinct Stress Cycle Number Calculation

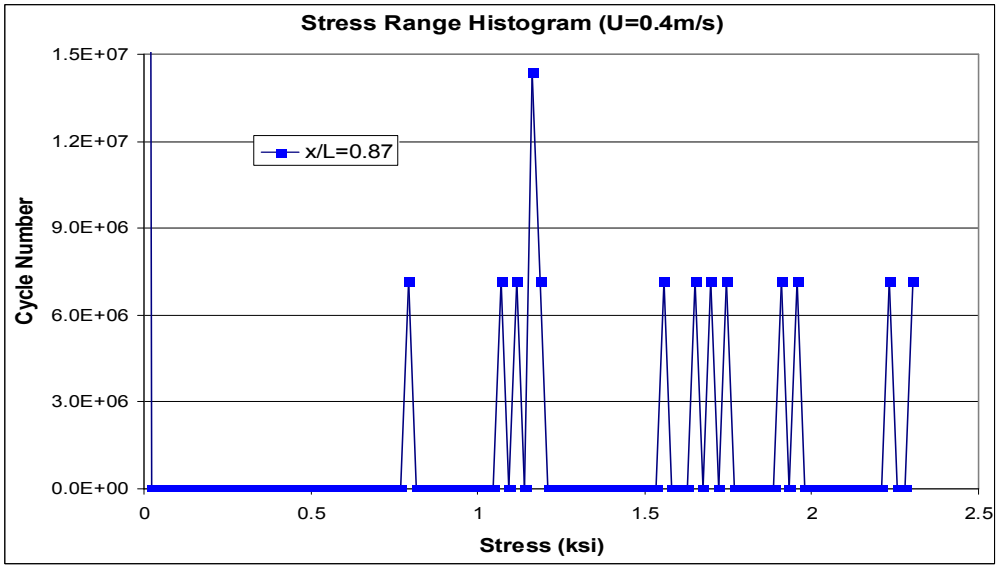

Fig. 9 Stress Range Histograms

S-N Curve Approach

The riser fatigue is calculated based on Palmgren-Miner's rule and S-N curve approach. For demonstration purpose, we calculated the fatigue damage using DNV S-N B1 curve (seawater with cathodic protection, DNV RP-C203), which applies to steel riser parent material. Its parameters are listed in Table 1. In this dissertation all the fatigue results are based on this curve, unless otherwise noted in the appropriate content.

Table 1 S-N Curve Parameters

S-N Curve	$N \le 10^6$		$N > 10^6$	
	m_1	$\log \bar{a}_1$	m_2	$\log \bar{a}_2$
B1	3	12.513	5	16.856

The fatigue damages consist of two components: in-line VIV induced fatigue and cross flow VIV induced fatigue. In-line VIV usually has lower motion amplitudes than cross flow VIV, but it doubles the modal number and frequency. To combine these two simultaneously, we need to combine the stress time histories ($\sigma_y(t)$ and $\sigma_z(t)$) first as Eq. (22):

$$\sigma(t) = \sigma_y(t)\sin\beta - \sigma_z(t)\cos\beta \quad , \tag{22}$$

where β=0° to 360° is the circumferential angle on the riser section, as defined in Fig. 10, and $\sigma_y(t)$ and $\sigma_z(t)$ are the bending stress in y and z direction respectively. The

combined stress time histories are then processed for stress histograms and fatigue damages. Both of them are functions of β and x/L.

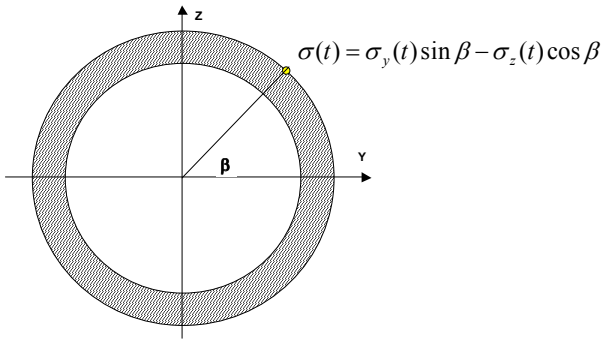

Fig. 10 Stress Combination Sketch

The fatigue calculation requires only the output results from the VIV simulations, and it can be performed after the simulations are completed. Therefore, it was designed as a stand-alone module that reads in the simulation results, and processes the curvatures and fatigue distributions along the riser.

The fatigue damage index (DI) (Tognarelli et al., 2004) is a parameter approximately proportional to the fatigue damage. For S-N curves with single slope m_1=3, the expression is as $DI = f_{z0} rms_z^3$, where the rms_z is the standard deviation of the bending strain time histories, which is related to the bending stress (Eq. 22) through Young's modulus E. And f_{z0} is the mean zero-up-crossing frequency for the stress response.

Partially Submerged Catenary Jumper Static Configuration

Flexible jumpers are special risers with relatively short length and low bending stiffness. The flexible jumpers are widely used in oil and gas industry to transport liquid or gas content between two facility units, usually located close to each other and have relative movement. In many of its applications, the jumper is positioned near the water surface, sometimes surface piecing, hence subject to severe environmental loads, including strong surface currents. To study a flexible jumper VIV, its catenary shape needs to be determined first.

Fig. 11 shows a typical jumper arrangement. In this hypothetical case the jumper's first end is attached to a submerged facility at 50 m below the mean surface level, and its second end is attached to a hang-off porch at 30 m above the mean surface level. The nominal horizontal span is 200 m. The jumper has a diameter of 0.33 m, and total length is 265 m (L/D=800). Its air weight is 100 kg/m, and submerged weight 20 kg/m (mass ratio=1.0). The mass ratio is $m/\rho D^2$ (Vandiver, 1993). A uniform current of 0.5 m/s (1 knot) is applied in the direction perpendicular to the jumper catenary plane. The upper section (about 10% of overall length) of the jumper is in the air, and the lower section (about 90% of the overall length) is submerged in the water.

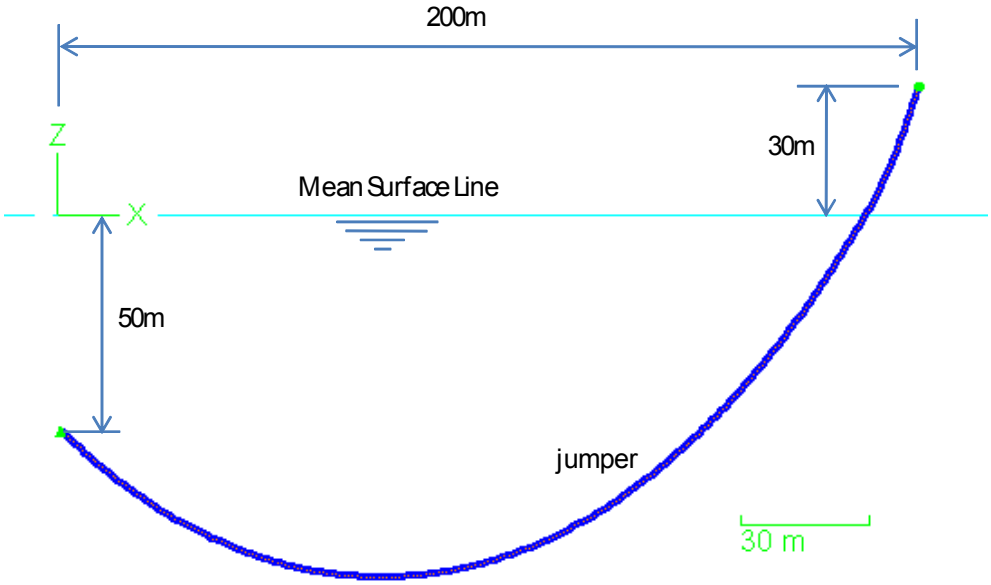

Fig. 11 Jumper General Arrangement

We developed a static catenary solver to determine the jumper configuration with arbitrary apparent weight distribution. It is based on a "trial and error" iteration approach. The jumper can be simplified as two segments with different apparent weights: the top section is above mean surface line, and has an apparent weight of 100 kg/m, and the bottom section is submerged in the sea water, and has an apparent weight of 20 kg/m. The jumper static configuration is not a simple catenary shape due to this apparent weight distribution disconnection. We adopted a finite element numerical scheme to calculate the jumper static configuration. First the jumper is discretized into 265 elements. At each element, the free body diagram is as illustrated in Fig. 12.

Based on the free body diagram, we have Eqs. (23) and (24).

$$T_i \bullet \sin\theta_i - T_{i+1} \bullet \sin\theta_{i+1} = 0\,, \tag{23}$$

$$T_i \bullet \cos\theta_i - T_{i+1} \bullet \cos\theta_{i+1} = w_i, \tag{24}$$

where T_i is the jumper effective tension, θ_i is the angle between the effective tension and the vertical line, and w_i is the apparent weight.

This algorithm allows us to calculate T_{i+1} and θ_{i+1} when T_i and θ_i are given. A trial and error approach was used since the jumper length and its two ends' coordinates are known. The iteration procedures are as follows:

1. Select an initial departure angle θ_1, usually 45 degrees is a good start point.
2. Select an initial associated top tension T_1.
3. Apply Eqs. (23) and (24) to each element i, from $i = 1$ to $N - 1$, where N =266 is the total nodal number. Note that the total element number is then equal to N -1.
4. Check the vertical elevation of the last node. If it is higher than the specified coordinate, then T_1 needs to be increased, otherwise T_1 needs to be reduced.
5. Adjust T_1 and repeat step 3 and 4 until the vertical elevation matches the target value.
6. Check the horizontal coordinate of the last node. If it is more than the specified coordinate, then θ_1 needs to be reduced, otherwise θ_1 needs to be increased.
7. Adjust θ_1 and repeat step 2 to 6, until the horizontal coordinate of the last node matches the target value.

This iteration process is fast. It took less than 100 iterations to achieve an accuracy of 0.1m at the second end coordinates for the studied jumper.

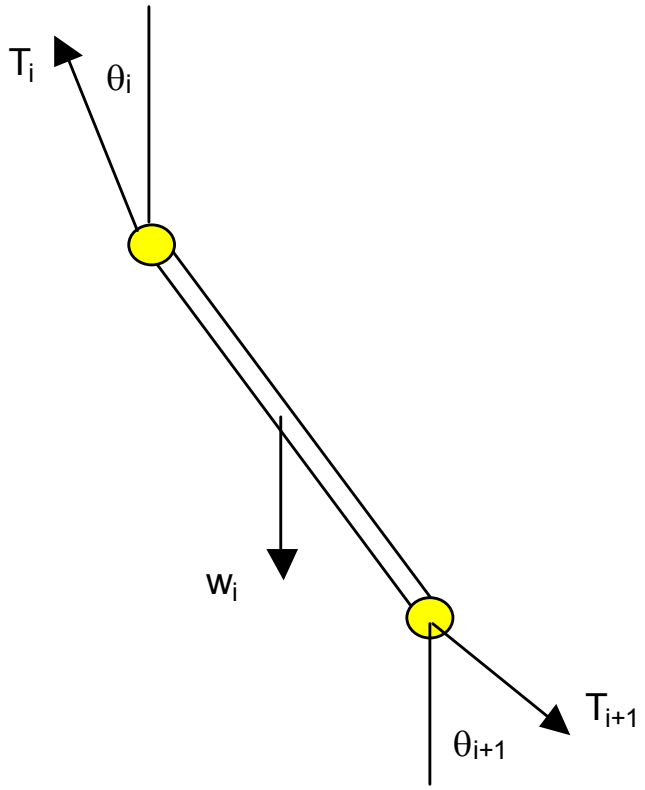

Fig. 12 Jumper Element Free Body Diagram

In this hypothetical case, the jumper overall length is 265 m, the horizontal span (the horizontal distance between the jumper's two ends) is 200 m, and vertical span (the vertical distance between the jumper's two ends) is 80 m. By applying the trial and error approach, we calculated T_1=28 kN, and θ_1=45.4 ^{o}. The jumper static configuration and effective tension distribution are as shown in Figs. 13 and 14 respectively. As a

validation of this approach, the results calculated by a commercial software tool (Orcaflex) are also presented. The comparisons show good agreements on both the jumper catenary shape and effective tension distribution. The jumper catenary shape shows a kink at the mean surface line (vertical axis=0) because of the jumper apparent weight discontinuity. For the same reason, the effective tension distribution also shows a sharp turn at the mean surface line.

The static configuration was fed into the dynamic VIV simulations as the initial boundary condition. And the jumper effective tension was applied to the modal analysis.

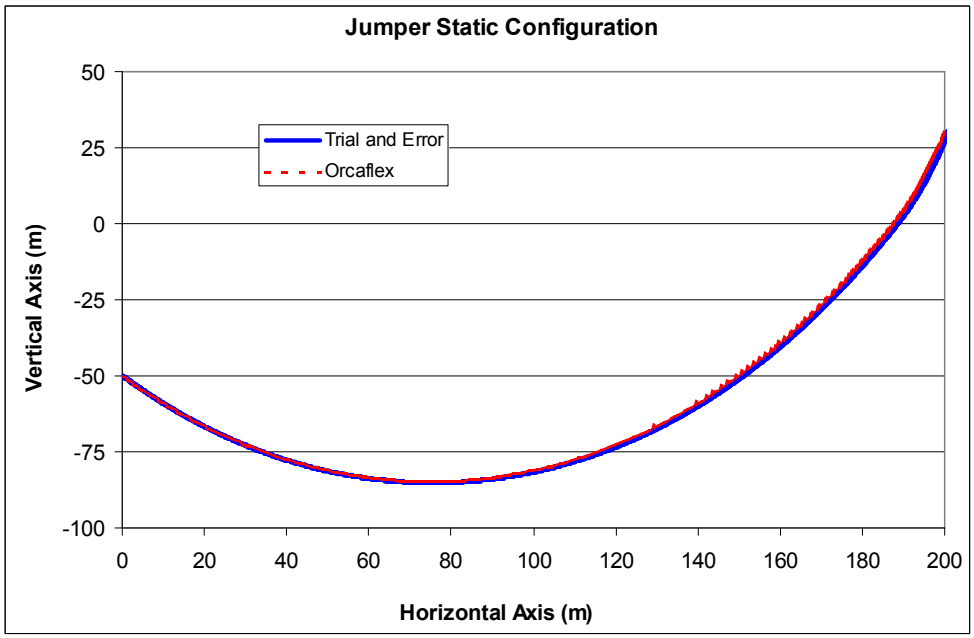

Fig. 13 Jumper Static Configuration

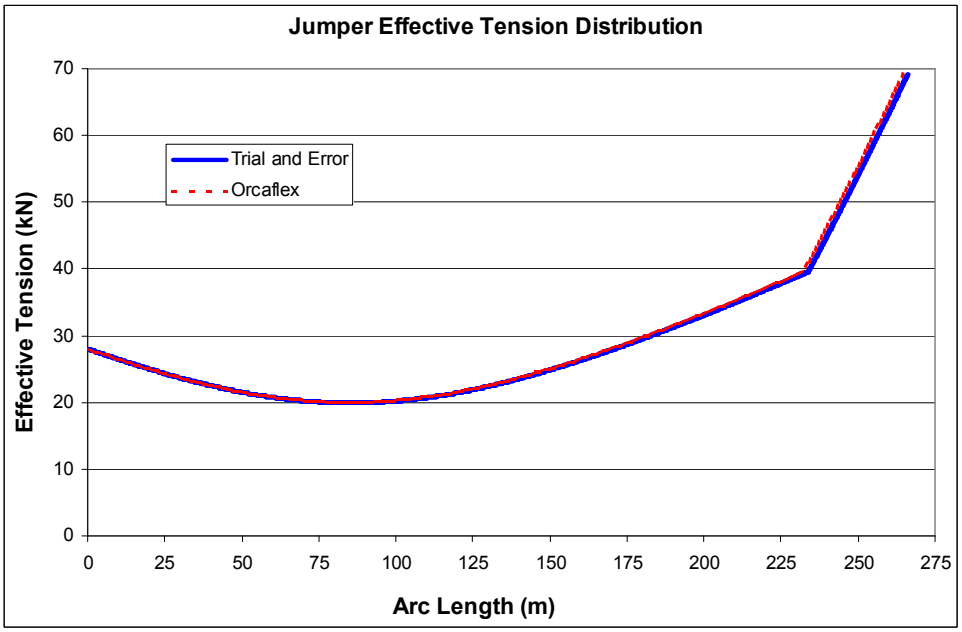

Fig. 14 Jumper Effective Tension Distribution

VIV Response Modal Extraction

The riser modal frequencies and modal shapes can be calculated numerically. Usually the riser (or flexible jumper) modal shapes are not orthogonal to each other unless $dT_i / ds = w_i$ =0. This can be demonstrated as following derivation.

We start from the linearized riser dynamic motion equation, which is given by Eq. (2). To include the catenary riser (jumper) situation, we replaced the parameter x by the curve length parameter *s*. Also we are specifically concerned in cross flow direction, and replaced y with z, as shown in Eq. (25).

$$T\frac{d^2z}{ds^2}+\frac{dz}{ds}\frac{dT}{ds}-\frac{d^2}{ds^2}\left(EI\frac{d^2z}{ds^2}\right)+f_z=m\ddot{z}+D_s.\dot{z} \quad , \tag{25}$$

where T is the riser effective tension, EI is the riser bending stiffness, f_z is the external force, m is the riser unit mass, and D_s is the riser structural damping. z is defined as the cross flow direction (+z up, -z down). s is the riser (jumper) curve length measured from the one end. Eq. (25) can be discretized using finite difference scheme:

$$\frac{dz}{ds}=\frac{z_{j+1}^n-z_{j-1}^n}{2h},\ \frac{d^2z}{ds^2}=\frac{z_{j+1}^n-2z_j^n+z_{j-1}^n}{h^2},$$

$$\frac{d^4z}{ds^4}=\frac{z_{j+2}^n-4z_{j+1}^n+6z_j^n-4z_{j-1}^n+z_{j-2}^n}{h^4},$$

$$\frac{d^2z}{dt^2}=\frac{z_j^n-2z_j^{n-1}+z_j^{n-2}}{\tau^2},\ \frac{dz}{dt}=\frac{z_j^n-z_j^{n-1}}{\tau},$$

where *h* is the arc segment length, τ is the simulation time step. And the final finite difference equation is similar to Eq. (12):

$$\begin{aligned}&\frac{EI}{h^4} z_{j-2}^n - \left(\frac{T_j}{h^2} - \frac{w_j}{2h} + \frac{4EI}{h^4}\right) z_{j-1}^n + \left(\frac{2T_j}{h^2} + \frac{6EI}{h^4} + \frac{m}{\tau^2} + \frac{D_s}{\tau}\right) z_j^n \\ &- \left(\frac{T_j}{h^2} + \frac{w_j}{2h} + \frac{4EI}{h^4}\right) z_{j+1}^n + \frac{EI}{h^4} z_{j+2}^n = RHS_j^n\end{aligned}, \tag{26}$$

where $RHS_j^n = f_{z\,j}^{\ n} + \left(\frac{2m}{\tau^2} + \frac{D_s}{\tau}\right) z_j^{n-1} - \frac{m}{\tau^2} z_j^{n-2}$.

When w_i=0, the coefficient matrix in the left hand side (LHS) of Eq. (26) is then symmetric. Consequently, the coefficient matrix has real eigenvalues (modal frequencies) and orthogonal eigenvectors (modal shapes). The coefficient matrix is not symmetric when $w_i \neq 0$. And its eigenvectors are usually not orthogonal.

In certain cases w_i is not important for modal frequencies and shapes (Sparks, 1980). However, it is important in some of the riser cases, such as the flexible jumper case since the jumper effective tension distribution mainly depends on the apparent weight.

When the modal shapes are orthogonal, the riser motions could be decomposed into its modal components through inner products. Assume the modal shapes are ξ_i. The riser response can be expressed as (w.r.t. curve length *s*):

$$z(s,t) = \sum_i \alpha_i(t)\xi_i(s), \tag{27}$$

where α_i is the modal response amplitude, and is a real value. It can also be expressed as complex value as Lucor et al. (2006). When w_i=0, the modal shapes are orthogonal, i.e. $\langle \xi_i * \xi_j \rangle$=0 for $i \neq j$, and $\langle\ \rangle$ represents the inner product of two vectors. Therefore, $\alpha_i(t) = \langle z(s,t) * \xi_i \rangle / \langle \xi_i * \xi_i \rangle$. When $w_i \neq 0$, the least squares method can be used to extract the modal response amplitudes. Let $\Lambda = [\xi_1 \quad \xi_2 \quad ... \quad \xi_n]$, where n is the maximum modal shapes considered in the calculation. Λ has a dimension of N x n, and N>n. The modal response amplitudes are then expressed as:

$$[\alpha_1 \quad \alpha_2 \quad ... \quad \alpha_n]^T = \left(\Lambda^T \Lambda\right)^{-1} \Lambda^T z(s,t). \tag{28}$$

As an illustration, let $z(s,t) = \sin(s)$, and Fig. 15 shows the decomposed modal response amplitude comparisons for the 265 m jumper case. The first 10 modes were used in the calculations. Both the inner product and the least squares methods show that the first mode has the largest response amplitude. And the modal amplitudes decrease as the modal number gets higher. Both methods would yield the same results if the jumper modal shapes were orthogonal. The difference confirms that the effect of w_i cannot be neglected during jumper VIV simulation.

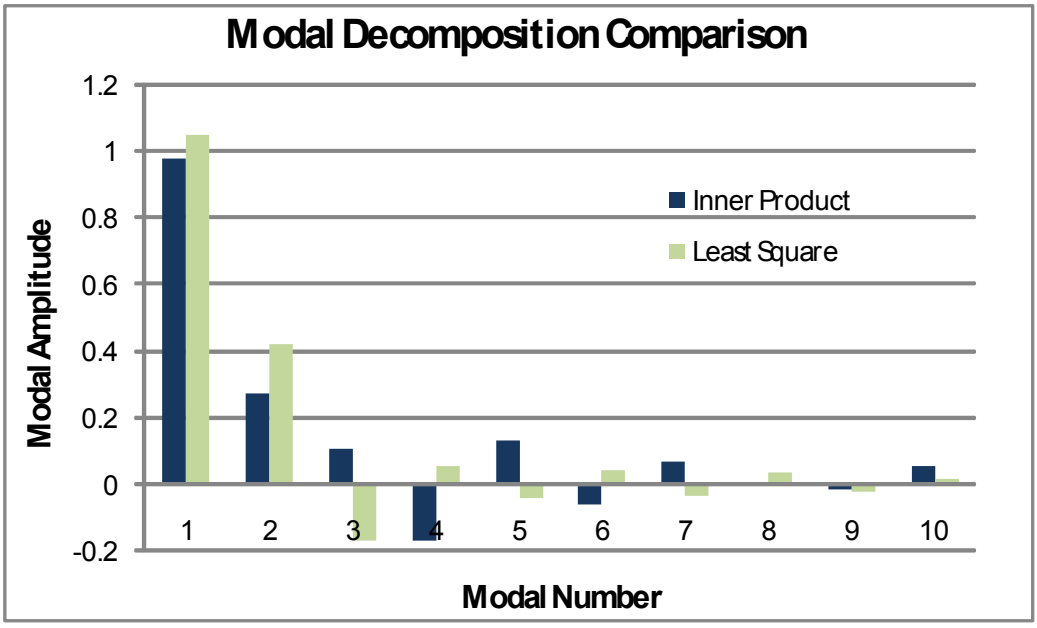

Fig. 15 Modal Amplitude Comparison

Jumper Transient Response

For long cylinder VIV simulation in 3D, the cylinder motion is complicated by many factors. Transient effect is one of them. Transient effect is not only introduced by the startup of the numerical simulation (when the cylinder is suddenly exposed to a current), but also continuously excited through the mean position (in-line direction) fluctuations, and kinetic energy redistribution among different modes. This section presents an approach that could be used to estimate the jumper (or other similar catenary risers) transient response, hence filter it from the jumper cross flow motions.

The jumper response to an impulse force is first studied. A constant load of 100 kg is applied to the 265 m jumper vertex at t=0, and then removed after t=1s, as shown in Fig. 16. The jumper will first deform due to the impulse load, and then experience free vibration after that. The jumper motion amplitude decays to 10% of its initial amplitude after 70 seconds. The riser motion time histories at each node between t=30s and 60s were used for modal extraction. And the modal response root-mean-square (rms) were calculated and normalized by the fundamental modal response rms. Then the data were plotted against the normalized modal frequency (f_i / f_1) as shown in Fig. 17. The data distribution could be approximated by a simple exponential function:

$rms_i = rms_1 \cdot e^{1-f_i/f_1}$.

The good approximation of the exponential function provides a possible method to eliminate the transient response from the jumper cross flow response. The procedures are as follows:

1. Perform the jumper VIV simulations in time domain.
2. Extract the modal response for all modes in the study ranges through least squares method.
3. Estimate the model response due to transient effect through exponential function approximation.
4. Filter the transient response from the total motion. The filtered response rms is: $rms_{filtered} = \sqrt{rms_{total}^2 - rms_{transient}^2}$.

Note that this approach is mainly based on observations on the jumper transient response, and its validity on other riser configurations (other than the catenary arrangement) needs to be investigated on case-by-case basis.

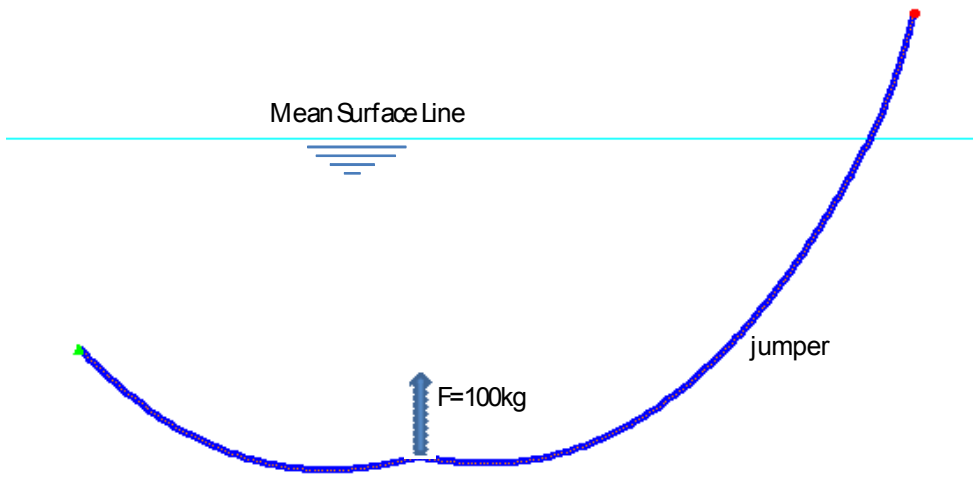

Fig. 16 Jumper Deformation under Impulse Load

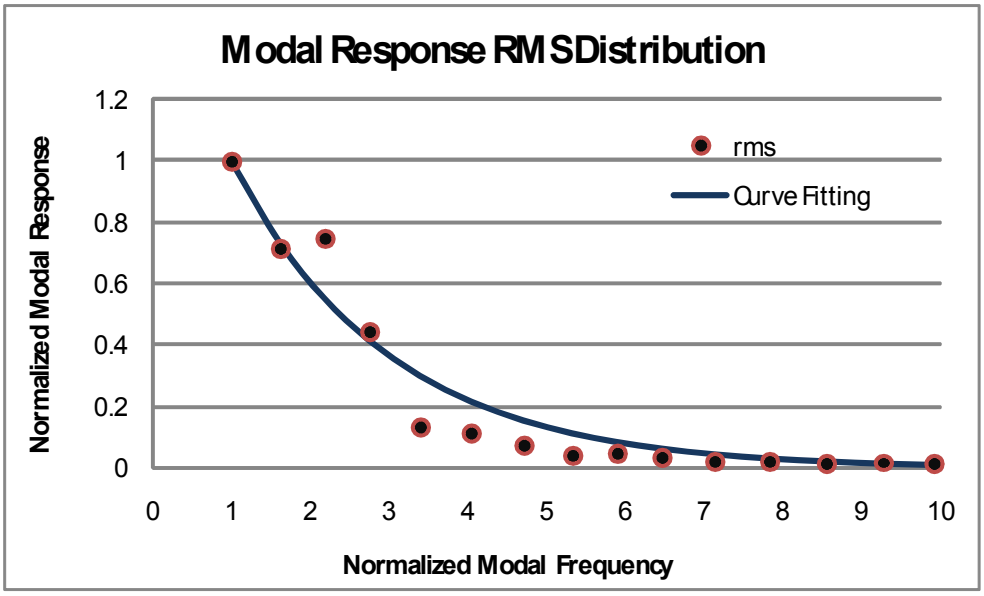

Fig. 17 Jumper Response Distribution

Integration of Riser Motion Solver to Parallel Fluid Solver

The riser VIV simulations presented in this dissertation were mainly performed using a single processor computer, i.e. all the computations by the fluid solver and riser motion solver used only one processor. However, recently the fluid solver of the FANS codes were expanded to parallel computation, and allowed for utilizing the multi-processor cluster. This section is to document the details of integration of the riser motion solver to the parallel version of the FANS codes.

In most of the practical riser VIV simulations, it is sufficient to discretize the riser string into a total element of less than 1000. Comparing to the total element number of the fluid domain (more than 1 million), it is negligible. And its computational effort is also insignificant. Therefore, it is reasonable that only one processor will handle the riser motion solver itself, i.e. all the riser motion computations will be carried out on the master processor.

The integration of the riser motion solver to the FANS parallel version includes the following tasks:

1. Locate the drag and lift force calculation codes in the parallel version, and implant new codes to output the drag and lift forces along the riser. In the force_moment module, additional codes were added to compute the forces at each different layer, i.e. k=1..nk if k is the riser spanwise dimension, on riser surface. The riser surface has a surface identification number of 3 or 4, i.e. i=1..ni, and j=1. The viscous friction force and pressure induced force were integrated on each cell, and on each processor. MPI_BARRIER subroutine

was called after the calculation to synchronize the computations on different processors, and MPI_REDUCE subroutines were called to sum up the total forces. Finally, the drag and lift coefficients were normalized from the drag force and lift force. And this normalization was carried out by the master processor only. The drag and lift coefficients were saved into a global array, which could be accessed from the motion solver subroutine to solver for the riser dynamics.

2. Locate the riser motion calculation section (2D), and replace it with 3D motion calculation codes (direct integral motion codes). The riser motion codes were implemented into the grid_motion module. Additional input data for riser motion calculation was listed in data file "riser.inp". The additional data includes a motion solver identification number ("motion"), characteristic length ("charl"), characteristic current velocity ("charu"), actual current velocity, and riser sectional properties.
3. Locate the data grid movement codes, and revise the codes to move the data grids based on riser 3D displacement. The riser motions were computed on the master processor only. However, the motion results were broadcasted to all processors through subroutine MPI_BCAST. The data grids then moved based on the riser instantaneous positions on each processor. Note that the data grid at each riser station has the same movement as the riser at that location.

A test case has been selected to confirm the successful integration of the riser motion solver to the parallel fluid solver. The selected riser configuration has following parameters:

- Riser length 9.63 m, diameter 0.02 m, top tension 817 N, unit mass 0.7 kg/m.
- Uniform current with speed of 0.42 m/s.
- Data grid consists of : (1) body grid 182 x 35 x 50, total node number 318,500, (2) wake grid 121 x 101 x 50, total node number 611,050, (3) background grid 121 x 91 x 50, total node number 544,500. The dimension in riser spanwise direction is 50, or 50 stations along the riser.
- Riser is vertically positioned with pin connections at both ends.

Three cases with different processor number were considered:

1. Single processor. In this case the fluid domain of all data grids were computed on one processor. This is equivalent to the serial code, and no parallel computation at all.
2. Two processors. In this case, the fluid domains of the body grid and wake grid were computed by the master processor, and the fluid domain of the background grid was computed by a second processor. The riser motions were solved on the master processor only.
3. Three processors. In this case, the fluid domain of the body grid was computed by the master processor, the fluid domain of the wake grid was computed by a second processor, and the fluid domain of the background grid

was computed by a third processor. The riser motions were solved on the master processor only.

Theoretically there is no limit on the processor number used for the CFD simulations. However, the data grids must be divided into smaller segments in order to utilize more processors. In other words, the maximum processor number could be utilized is the total data grid number, where each processor is assigned only one data grid. To achieve the minimum computational time, it is recommended to distribute the data grids to each processor with similar total nodal number. This would ensure the work load on each processor is roughly the same, and reduce the processor idle time.

The simulation results are presented in Appendix A. It is found that the parallel version of the FANS codes (with the riser motion solver integrated) functioned well, and provided similar cross flow response as the serial version. The minor discrepancy is due to the fluid solver difference: the fluid solver in the parallel version adopted an improved velocity-pressure iteration algorithm. The results also confirmed that the computational time could be significantly reduced by using the parallel computational techniques.

CHAPTER III

2D SIMULATION OF FLOW PAST A FIXED/VIBRATING RISER

Interference is an important design consideration for deepwater applications. In many design practices no collisions are allowed between objects such as risers, flowlines, umbilicals, tendons/mooring lines, and hull structures. Among them interference between top tensioned risers is of particular interest. The reason is that top tensioned riser array has strict limitations on surface wellheads layout and subsea wellhead layout. When water depth reaches 10,000ft, the riser string experiences much larger lateral displacement due to current force. To avoid riser clashing, a very large subsea wellhead pattern might be required. This would impose challenges to riser system design, especially when large quantity of top tensioned risers is planned (Huang and Chen, 2006).

In conventional design approach (API RP 2RD, 1998), riser interference analysis is usually carried out quasi-statically. The wake field behind the upstream riser is calculated by using Huse's formula (Huse 1993, 1996). The VIV induced drag coefficient amplification of upstream riser is approximated by multiplying the base drag coefficient by an amplification factor. And an effective drag diameter is used to calculate the wake field behind the upstream riser undergoing VIV. This approach is simple and straightforward. However, it might also introduce conservatism and uncertainty into the design. Consequently, it is desirable to evaluate the VIV effect on upstream riser effective drag coefficient and wake field.

Therefore, the analysis results presented in this section is served as following purposes:

1. Compare the wake flow field to the experimental data (Huse's formula) and validate the data grids and CFD approach.
2. Discover localized features of the flow fields that are not included in the Huse' formula.
3. Provide a riser interference example case and illustrate the significance of the findings.

In this simulation the effective drag coefficients and wake fields are obtained for both fixed riser and vibrating riser. The Reynolds number was chosen as $3x10^5$. A study case is selected with typical Gulf of Mexico 10-year loop current and a typical single casing production riser. The riser system data, including air weight, submerged weight, and top tensions, are then developed. In the example case, the riser interference analysis is performed based on the obtained effective drag coefficients, and the results are compared to those obtained by Huse's formula.

Data Grid

Overset grid (Chimera) technique provides an effective way to handle riser movement. Figs. 18 and 19 show the data grids used in this study. The body grid has a dimension of 182x41x12, while the background grid has a dimension of 201x101x12. The data grids have been delicately generated with very fine grid sizes at the riser boundary layer and vortex shedding zones. The body grid and background grid are

overlapped to an extent such that these two grid sets could “communicate” with each other efficiently and accurately. The overlapping region depends on the instantaneous riser position, and is dynamically determined at each time step.

The data grids are normalized by the characteristic length, which is chosen as the riser diameter. Therefore, these data grids are genetic and applicable to problems with different riser sizes and far field velocity. The background grid covers a region of 20D in flow direction, and 14D in transverse direction. The simulation starts with an initial uniform flow on the background data grid, and reaches a relatively periodic state after a period of transitional flow.

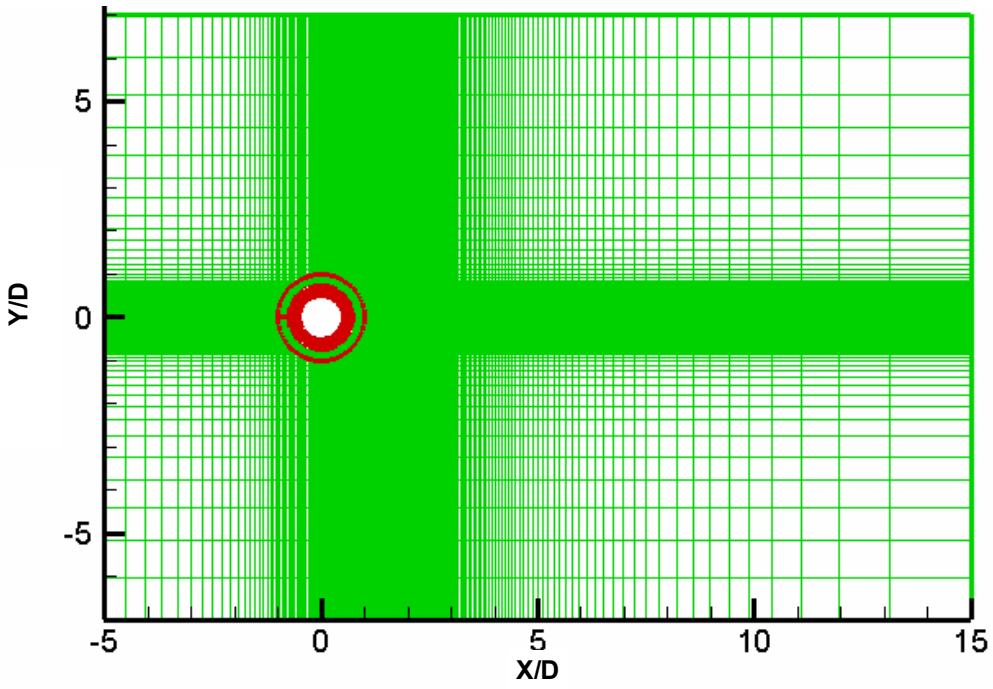

Fig. 18 Overset Grid for Wake Field Computation

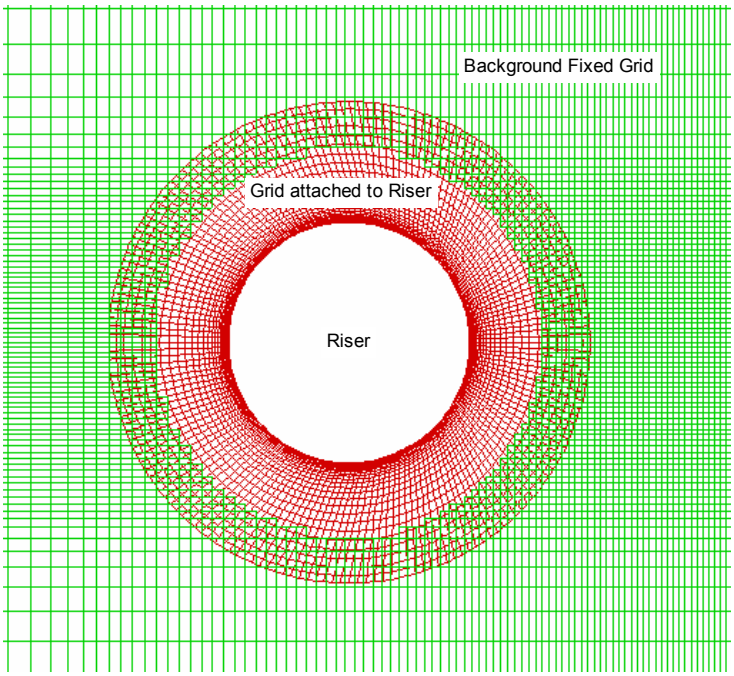

Fig. 19 Overset Grid for Wake Field Computation – Riser Surface Vicinity

Riser Interference Analysis Procedures

The riser interference is checked by using a quasi-static approach under typical 10-year loop current profile in Gulf of Mexico. The effective drag coefficients of the downstream risers are calculated based on obtained wake field. The analysis procedures are as shown in Fig. 20. Since at the beginning both of the downstream riser deflection and effective drag coefficients are unknown, initial assumptions are needed to start the iterations. The riser string is divided into small segments. Each segment has its own effective drag coefficient, which is calculated based on Huse's formula or CFD approach. Both of them are used in this section, and the results are compared as well. In the CFD approach, a more accurate way is to position two risers in the same

computational domain, and compute the effective drag coefficients on both risers directly. However, this would require a CFD simulation on each different riser position pairs, and introduce tremendous computational effort, hence it is not adopted here.

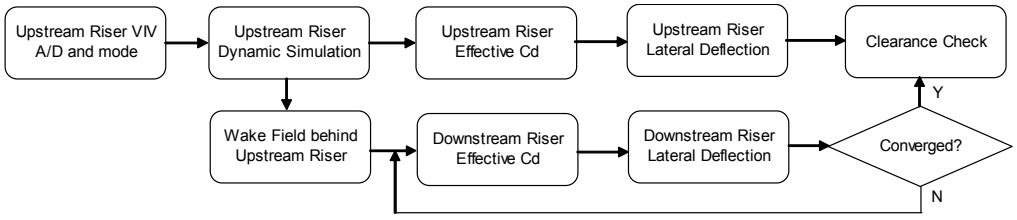

Fig. 20 Riser Interference Analysis Flow Chart

Simulation Results

A typical 10 ¾" single casing production riser has been sized for 10,000ft water depth as shown in Table 2. Conventional hydro-pneumatic tensioners are assumed, and pipe properties were obtained from API 5L (2000) and API 5C3 (1994).

Table 2 10 ¾" Riser Top Tensions

Riser Type	Riser Mode	Nominal T_o (kips)	Wet Wt (kips)	TF
10 3/4" Single Casing Riser	Normal Operating	1026	769	1.34
	Well Killed	1350	1036	1.31

The riser clearance is checked in 10-yr loop current condition in Gulf of Mexico. The current profile has a maximum speed of about 3 knots at 1,500 ft below the mean sea surface. In this section the upstream riser VIV a/D and frequency are calculated by using a separate VIV analysis tool as:

- Single mode excited: 86^{th},
- a/D=0.28,
- Frequency = 1.6Hz.

The upstream riser is assumed to be in heavy mode (well killed) and with VIV. The downstream riser is assumed in normal operating condition and without VIV. Typical riser spacing at the topsides wellbay is used. The riser spacing on the sea floor is usually a design parameter. Here we chose this parameter based on previous TLP project experience with water depth extrapolation.

Simulations have shown a rapidly varying effective drag coefficient within each vortex shedding and riser vibrating cycle. Considering the varying frequency is high, the riser vibrating amplitudes in the current plane (in-line vibration) is expected to be small. Therefore, time averaged mean drag coefficients are used to calculate the riser deflections. This quasi-static approach is valid if the clearance satisfies certain minimum value.

Fig. 21 shows the flow field vorticity contours for fixed riser. Figs. 22 and 23 show the comparisons of the wake field velocity distributions by using Huse's formula and CFD approach. The comparisons show very good agreement. It also confirms the

validity of the CFD approach. Fig. 24 provides the time history of the effective drag coefficient. It has a mean value of 1.0, which is consistent with published Cd vs Re curve and design codes such as API RP 2RD.

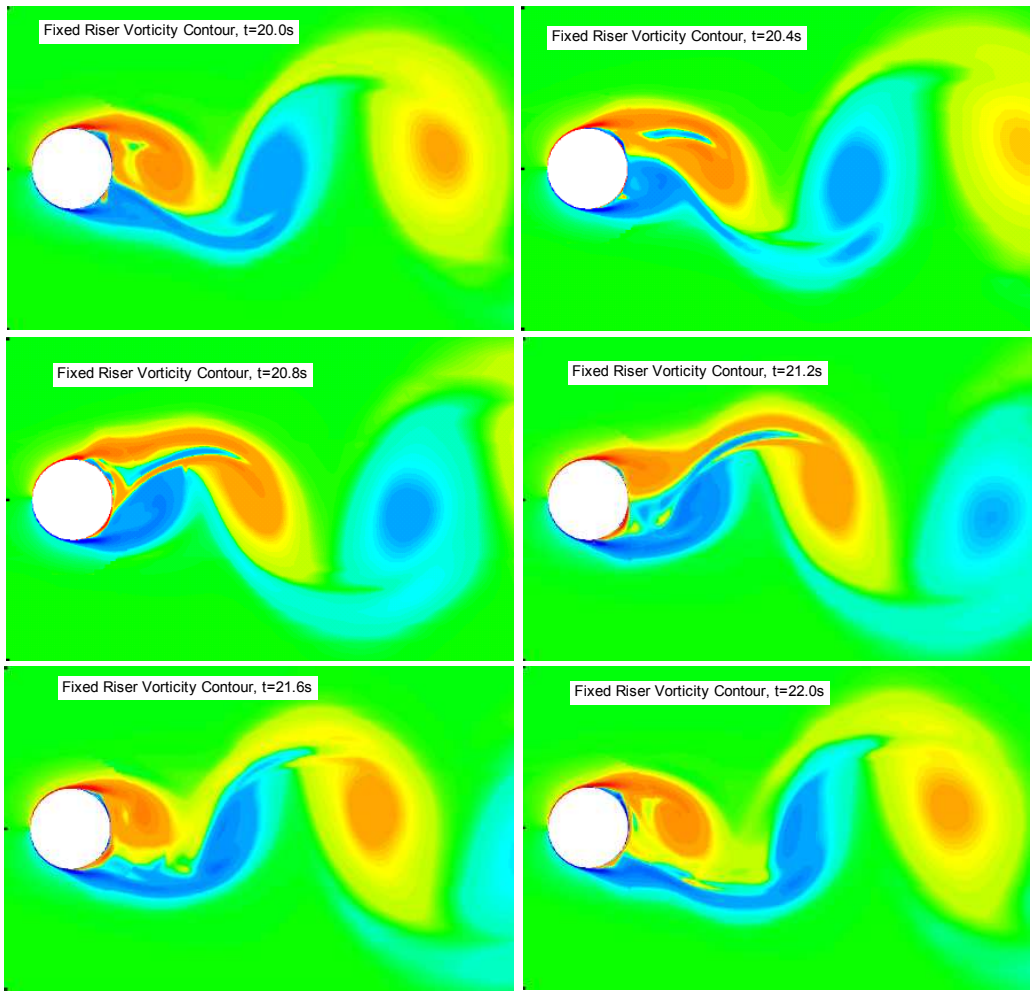

Fig. 21 Vorticity Contours for Fixed Riser

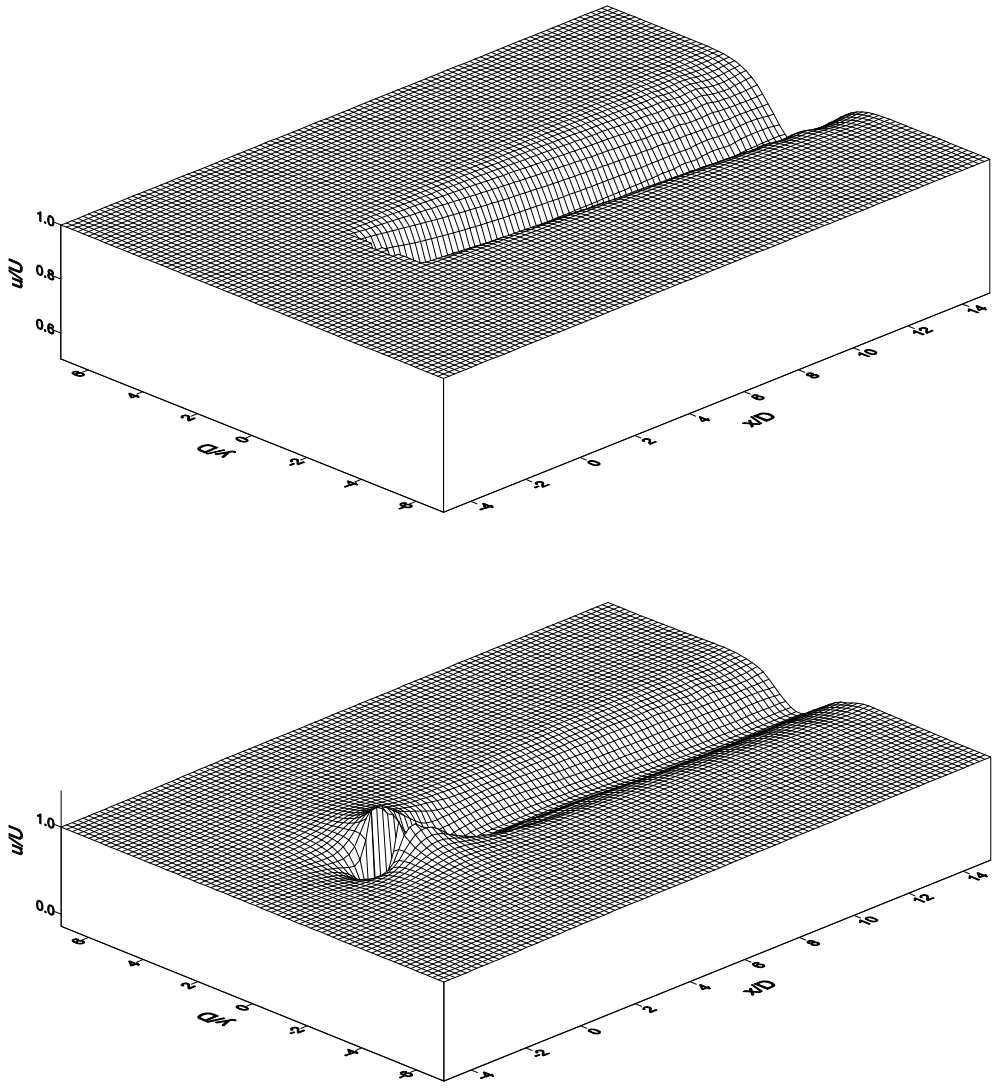

Fig. 22 Wake Field 3D View – Top:Huse's Formula, Bottom:CFD

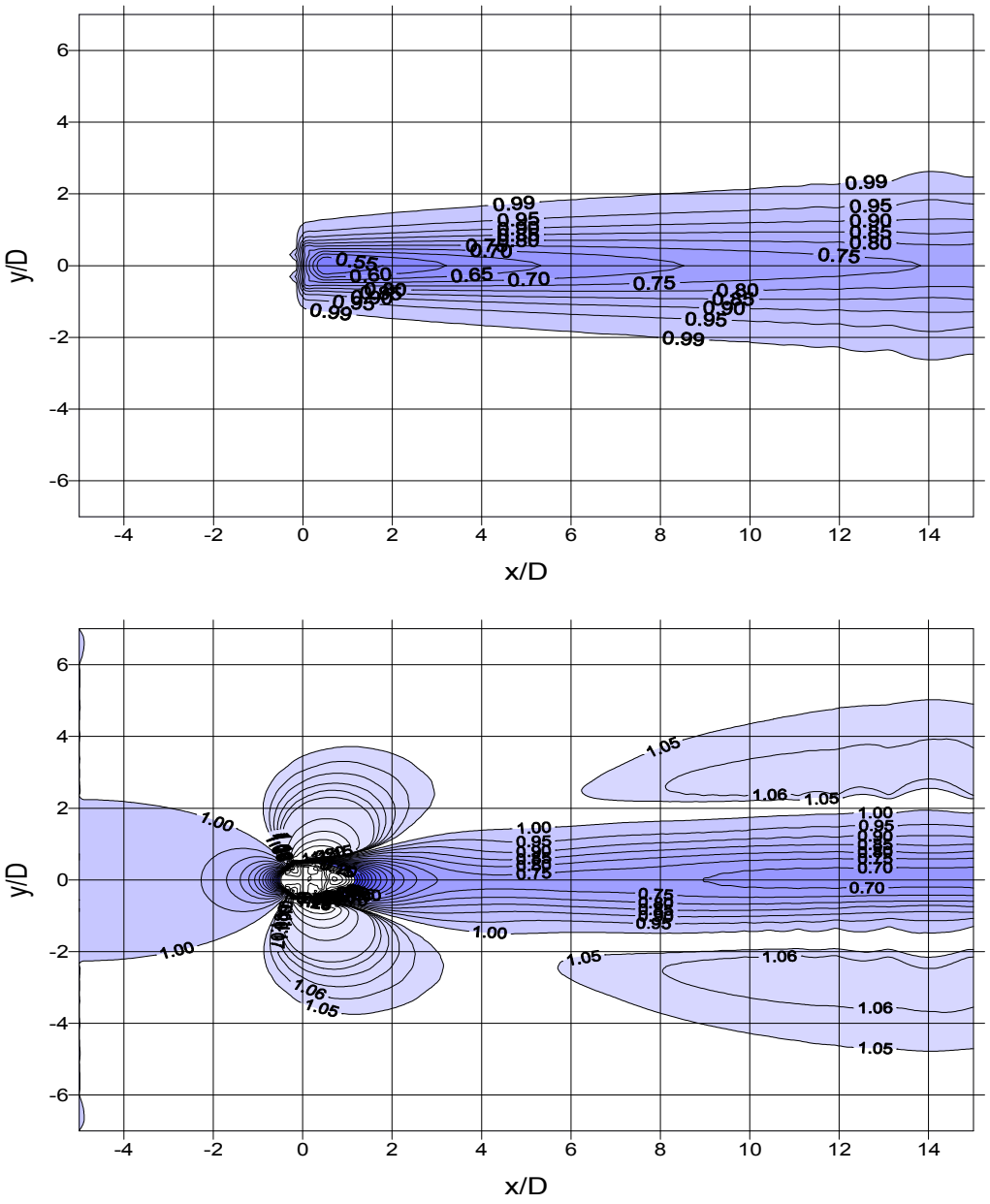

Fig. 23 Wake Field Contour – Top:Huse's Formula, Bottom:CFD

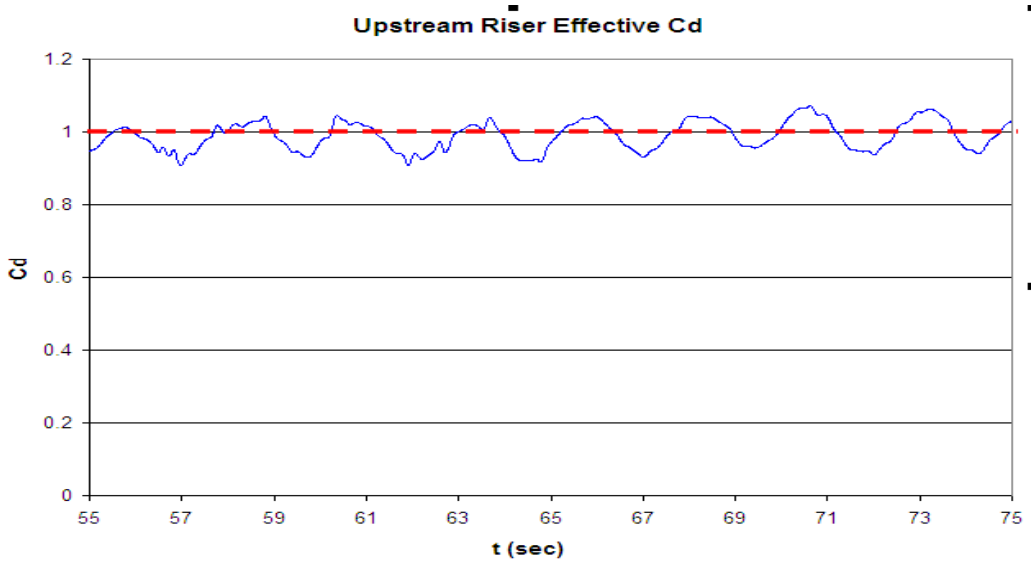

Fig. 24 Effective Drag Coefficient

Fig. 25 shows the flow field vorticity contours for the vibrating riser. Fig. 26 shows the wake field velocity distributions. The observations are as follows:

- The wake half-width is not sensitive to the riser VIV, at least when a/D does not exceed the order of 1.
- The fluid velocity directly behind the riser is slightly lower than fixed riser case. In other words, the wake velocity at the centerline y=0 increases slightly when the riser vibrates.
- The fluid velocity is higher than far field inlet current speed at regions y>2D and y<-2D. As a result, the downstream riser would be subject to higher drag force at these regions, which alleviates the riser interference problem.

Fig. 27 presents the effective drag coefficient time history. It varies in riser vibrating frequency, with values ranging from 0.5 to 2.8. The drag force variation is mainly due to the pressure zone shifting on the riser surface. The averaged mean value of 1.37 is then used for the upstream riser with VIV.

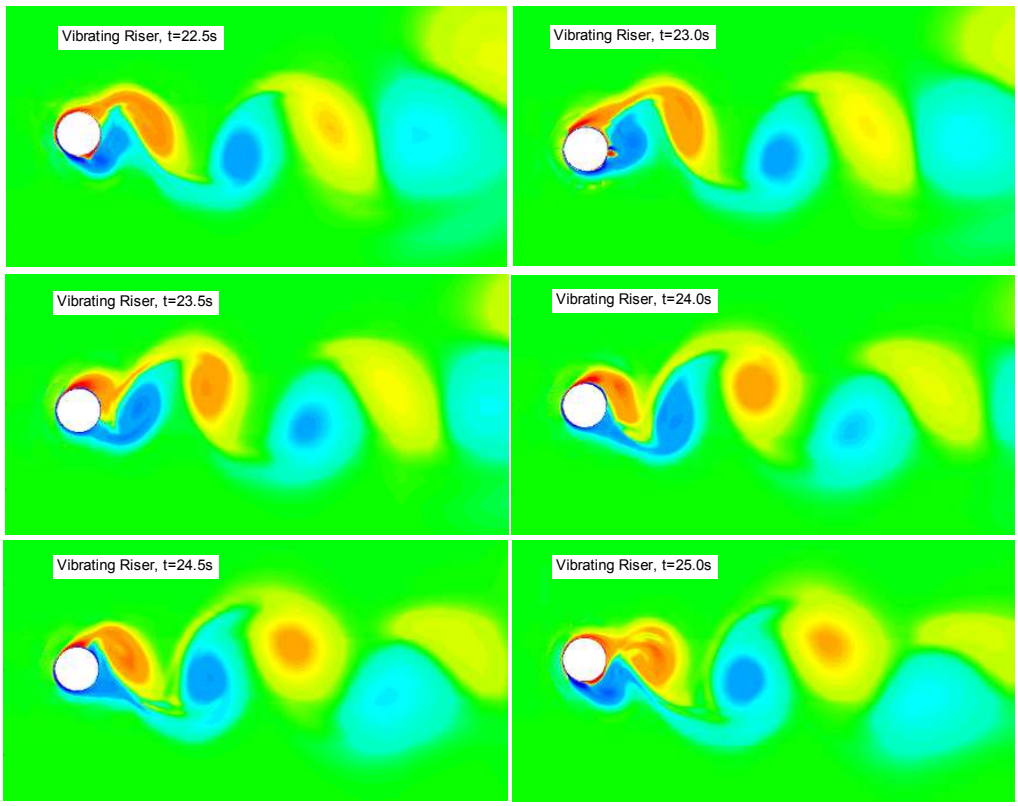

Fig. 25 Vorticity Contours for Vibrating Riser

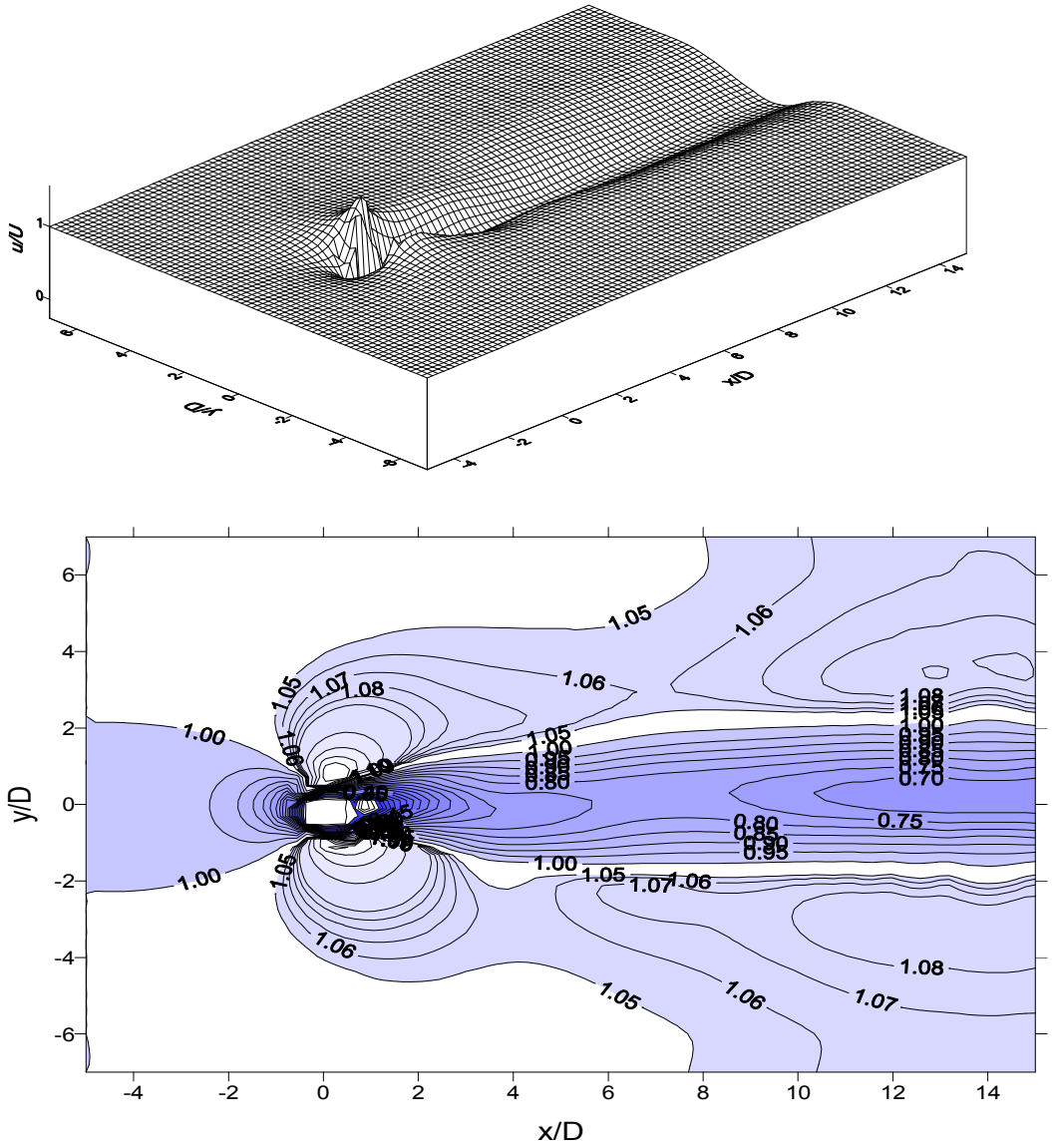

Fig. 26 Wake Field behind a Vibrating Riser

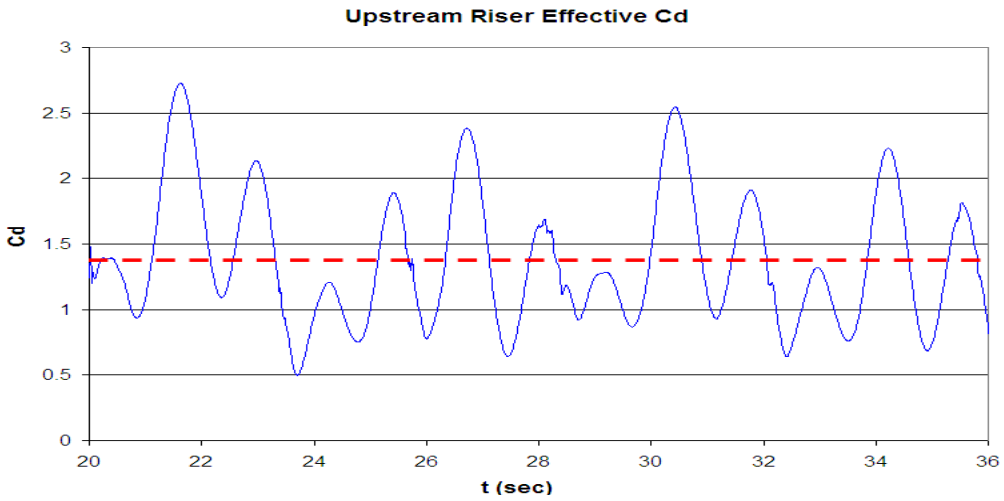

Fig. 27 Effective Drag Coefficient on Vibrating Riser

Riser Clearance Check Results

Riser clearance has been checked in 10-yr loop current based on the methodology presented in previous sections. The riser string is modeled with about 400 elements in different sizes. Fine elements have been used on the specialty joints and transitional sections. Figs. 28 and 29 show the riser lateral displacements by using Huse's formula and CFD method respectively. It is found that for the same riser arrangement, Huse's formula predicts a negative clearance (collision occurs), while CFD approach predicts a narrow positive clearance (no collision). This is critical since the potential collision is very difficult to avoid by simply increasing the riser spacing on the sea floor. Without using the CFD approach, it would be impossible to demonstrate the designed riser system has sufficient clearance up to 10-yr loop current conditions.

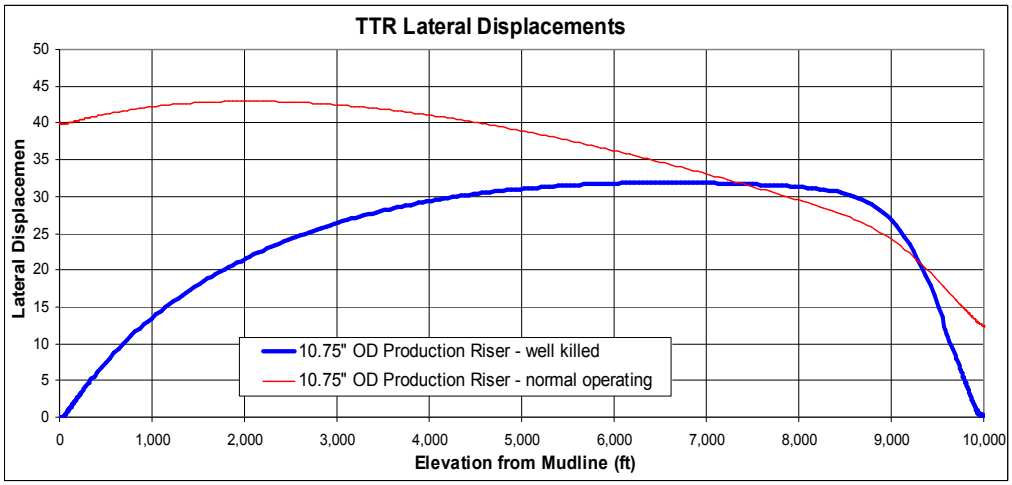

Fig. 28 Riser Displacement along Riser – Huse's Formula

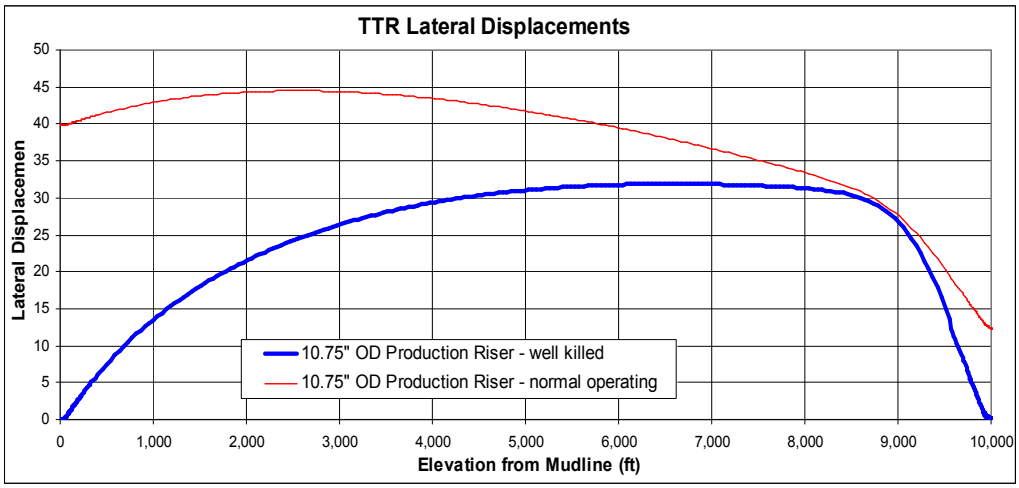

Fig. 29 Riser Displacement along Riser – FANS

Discussions

This section preliminarily studied the ultra deepwater riser interference by using an unsteady, overset-grid (Chimera), incompressible Navier-Stokes (RANS) method. It is found that risers could have very large lateral deflections in strong and deep currents, and riser interference could impose serious challenges to riser system design. Under certain design conditions, such as 10-yr loop current eddy as studied in this section, the riser interference results are sensitive to drag coefficients. Therefore, accurate assessment of the effective drag coefficients on both the upstream and downstream riser becomes critical. The CFD time domain simulation approach has predicted a narrow wake field and a high-speed zone outside the wake field. Both of them positively affected the interference results. It is also indicated that the “no collision” design criteria could be hold up to 10-yr extreme current events in ultra deep water riser systems (Huang and Chen, 2006).

CHAPTER IV

3D SIMULATION OF FLOW PAST A VERTICAL RISER IN UNIFORM CURRENT

During the last several years many VIV experiments have been carried out on deepwater risers with large L/D. With the some of the newly released experimental data, it becomes possible now to extend the comparisons between CFD results and experimental data to greater detail, such as modal response amplitudes and phase angles, response power spectral densities (PSD), and motion trajectories, etc. In this chapter, two uniform current profiles were chosen form the experimental database (oe.mit.edu/VIV/) with constant speed of 0.42 m/s (test case 1105) and 0.84 m/s (test case 1108) respectively. During the experiment, the riser was vertically positioned under the water. Both ends were fixed to the test rig, which rotates at a constant speed. This would simulate a uniform current condition. Note that after the rig completes one cycle, the riser moves into its own wake field. This fluid disturbance is expected to be negligible and not considered in the present numerical simulations (Huang et al., 2009a, 2009b).

In the present simulations, 1.5 million elements for this 10 m long top-tensioned riser (L/D=482) were used. The riser lateral motion is solved in the time domain using the direct integration solver. Both in-line and cross flow riser responses are computed and compared with the published experimental data.

Data Grid

The simulation data grid consists of three sets of data grids and has a total of 1.5 million grid points. The three sets of data grids are: (1) body grid – the data grid adjacent to the riser surface that provides fine resolution to calculate the fluid-riser surface interaction and vortex generation, it has dimensions of 50 x 182 x 35, (2) wake grid – it interfaces with body grid and background grid and provides good resolution for vortex propagation, it has dimensions of 50 x 121 x 101, (3) background grid – as the name suggests, it defines the outer boundary of the computational fluid domain, provides the far field fluid boundary conditions, interfaces with and provides a physical extension to the wake grid using relatively coarse mesh. It has dimensions of 50 x 121 x 91. Figs. 30 and 31 show the fine meshes near the riser surface, and the overlapping region between the body grid and wake grid. Fig. 32 shows the data grids with riser deflection (only three layers are shown for clarity). When the riser vibrates, the data grids also move with the riser so there is no gap between the riser and the grids at any time.

It was modeled as a beam with top tension of 817 N, and discretized using 250 segments – a typical number for riser global dynamic analysis. Its two ends are pinned to the ground with zero rotational stiffness. Its unit mass is 0.7 kg/m, and bending stiffness is 135 N-m. No damping has been included. It is estimated that the dominant mode should be less than the sixth mode. The Reynolds numbers are 7.5×10^3 for U=0.42 m/s and 1.5×10^4 for U=0.84 m/s respectively.

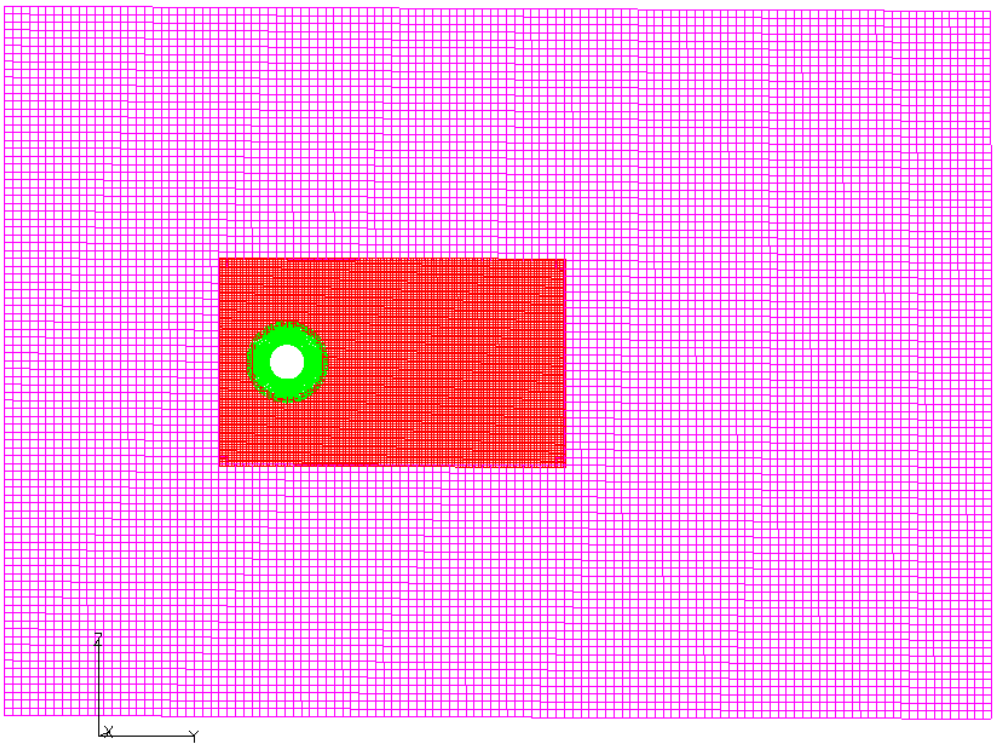

Fig. 30 Data Grids at x/L=Constant

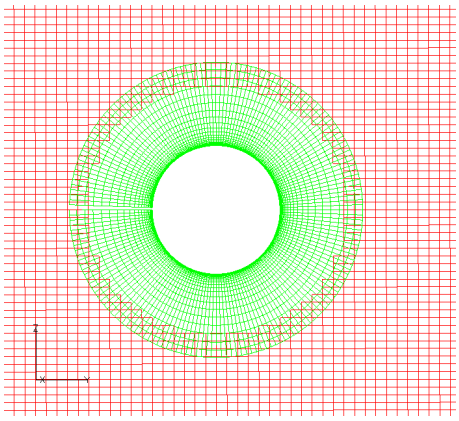

Fig. 31 Grid Details on Riser Surface and Overlapping Region

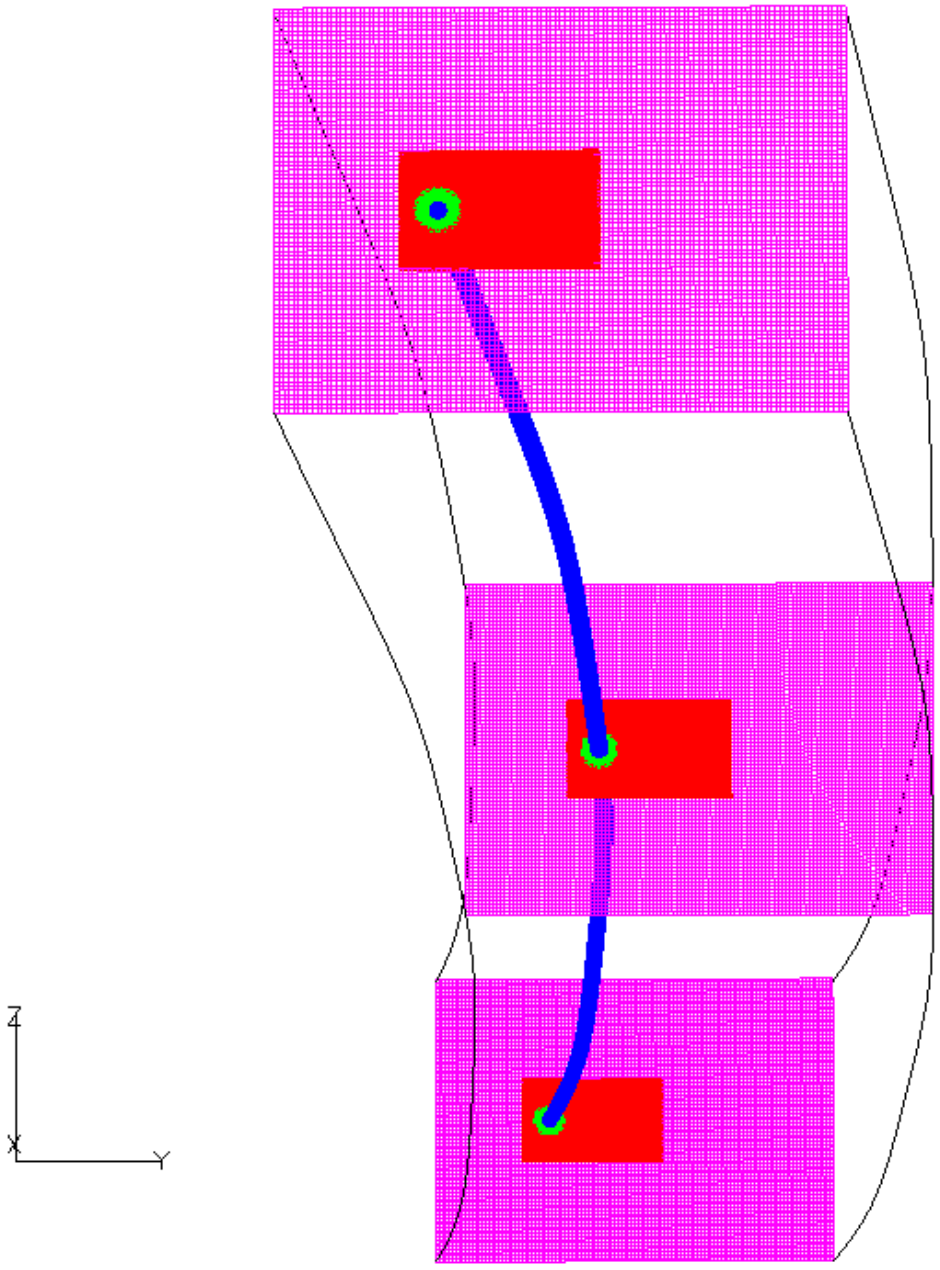

Fig. 32 Data Grids with Riser Deflection

Simulation Results

The riser VIV responses in two uniform current profiles are analyzed. The current speeds are U=0.42 m/s and 0.84 m/s. The corresponding experimental load case numbers are 1105 and 1108 respectively. These two current profiles were chosen to cover the typical current speed range that could occur in offshore fields. The cross flow VIV is generally more important than the in-line VIV, hence it was the primary focus of this study.

First we performed the modal analysis of the vertical riser. Table 3 shows the natural frequencies of the riser under three conditions: (1) the riser is horizontally positioned in the air with constant tension 817 N. Its fundamental frequency is 1.78 Hz; (2) the riser is vertically positioned in the water, with constant added mass coefficient Ca=1.0. Its fundamental frequency is reduced to 1.44 Hz based on averaged tension 797 N; (3) discretize the riser into segments and calculate the eigenvalues and eigenvectors, with constant added mass coefficient Ca=1.0, and distributed tension (top 817 N, bottom 777 N). Its fundamental frequency is calculated as 1.38 Hz, which is slightly different (5%) from condition (2). We also calculated the modal shapes. They are similar to the sinusoidal shapes, but not exactly the same. The riser effective tension varies along the pipe and causes the modal shapes to deviate from simple sinusoidal function, especially for deepwater risers. The modal analysis is important because we need the modal frequencies to assess the dominant modes, and we also need the modal shapes for almost all the post-processing work, including modal component extraction, modal response PSD, modal added mass, etc. In our present method the modal shapes are not involved in

the numerical simulations because we are using the direct integration riser solver. The FANS codes also include a riser modal motion solver, which calculate the riser segment instantaneous positions based on modal superposition.

Table 3 Riser Modal Frequency Summary

Mode No	In Air, 817N		In Water, 817N/777N		FEA Calculated	
	ϖ (rad/s)	f (Hz)	ϖ (rad/s)	f (Hz)	ϖ (rad/s)	f (Hz)
1	11.2	1.78	9.1	1.44	8.6	1.38
2	22.3	3.55	18.1	2.88	17.3	2.75
3	33.5	5.33	27.2	4.33	26.0	4.13
4	44.6	7.10	36.3	5.77	34.6	5.51
5	55.8	8.88	45.3	7.21	43.3	6.89
6	66.9	10.65	54.4	8.65	52.0	8.28
7	78.1	12.43	63.4	10.10	60.7	9.67
8	89.2	14.20	72.5	11.54	69.5	11.06

The simulations start with an initially straight riser. The riser begins to deflect after it is exposed to a uniform current, and it deflects increasingly until its internal restoring force is sufficiently large to overcome the drag forces. The time domain simulations are carried out to a total of 20,000 time steps, or the fluid travels a total distance of 200 OD (4m) for both cases. Fig. 33 shows the evolution of the riser VIV and vortex shedding under different current profiles. The left hand side riser is undergoing VIV in uniform current 0.42 m/s, while the right hand side riser is undergoing VIV in uniform current 0.84 m/s. Both risers start with straight configuration. After a period (approximately 2 seconds) of transient response, both risers reach nearly equilibrium

positions. The maximum riser deflection occurs at the middle section for risers in uniform currents. The maximum riser deflection amplitude for the U=0.84 m/s case is approximately four times of that for the U=0.42 m/s case. This is reasonable since the drag force is proportional to the square of the current speed. The majority of the vortex shedding shows a clear 2S pattern (Williamson and Roshko, 1988). The cross flow VIV amplitudes are in the order of 1D. No obvious 2T patterns (Williamson and Jauvtis, 2004) have been observed in these two simulations.

Fig. 34 shows two snap shots of the vorticity contours for U=0.42 m/s and U=0.84 m/s respectively. The riser maximum lateral deflection for U=0.84 m/s case is approximately 20D (riser diameter), and it reduces to 5D for the U=0.42 m/s case.

Fig. 35 shows the riser deflection time history. The riser achieves its balanced position through two steps: (1) riser deflects toward current downstream with no or negligible cross flow VIV. In this case the drag coefficient on the riser is approximately 1.1 along the riser (time averaged); (2) the riser starts cross flow VIV. The drag coefficient on the riser is suddenly increased due to cross flow VIV. The VIV-enhanced drag coefficients are much higher than the initial value (or 1.1), and the exact values are expected to be related to many parameters such as fluid conditions, x/L, etc. As a result of the cross flow VIV, the riser deflects further downstream until a new balanced position is reached.

Figs. 36 and 37 compare the riser cross flow VIV responses to the experimental results for U=0.42 m/s and U=0.84 m/s, respectively. The comparisons show general agreement. The CFD simulations slightly overshoot the cross flow VIV amplitudes during the ramp-up time. A possible reason is that the riser is suddenly exposed to the uniform current while in the experiments the test rig rotating speed is gradually increased to the desired values. The riser motions at x/L=0.44 are compared because (1) the experimental data were provided at this location, (2) it is near the center of the riser and has large deflection, which is expected to be a good location for cross flow motion comparisons. While more comparisons can be carried out at different riser locations, it is generally more desirable to compare the rms a/D along the riser length, as discussed in the next section.

Fig. 33 Vortex Shedding Evolution, Left: U=0.42 m/s, Right: U=0.84 m/s

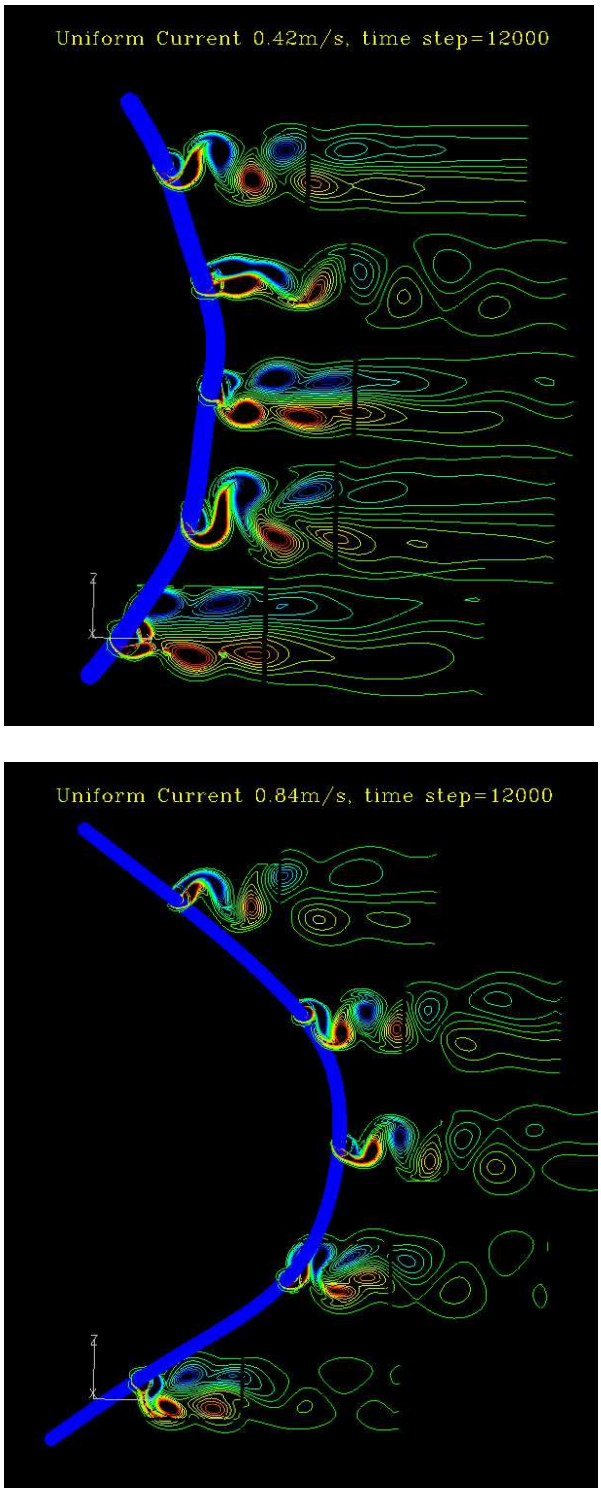

Fig. 34 Vortex Contour, Top: U=0.42 m/s, Bottom: U=0.84 m/s

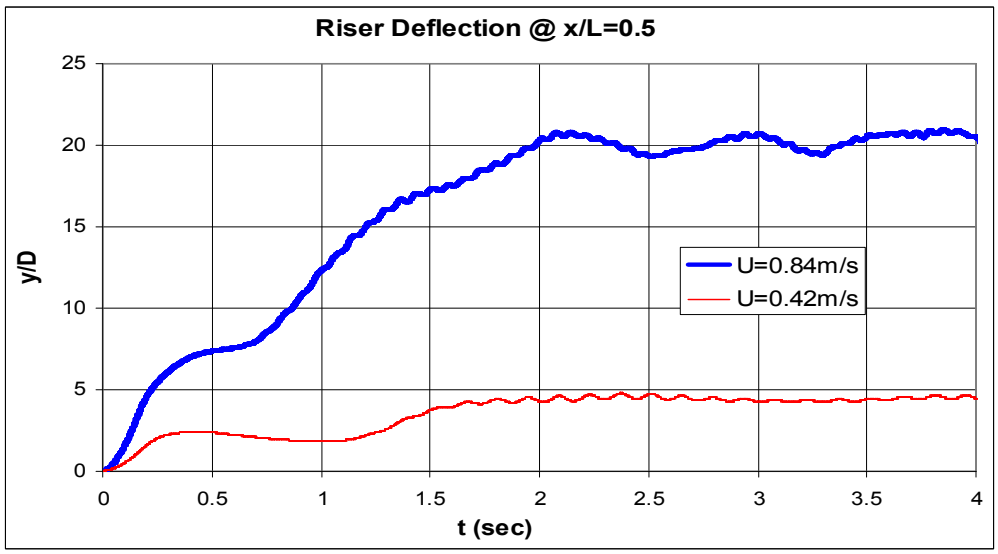

Fig. 35 Riser Deflection Time History, x/L=0.5

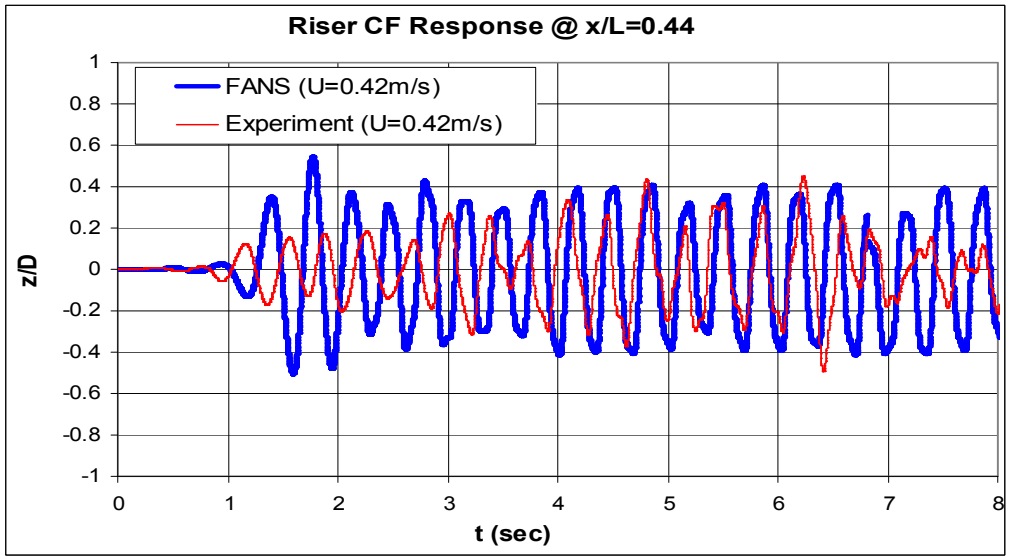

Fig. 36 Riser CF Response (U=0.42 m/s)

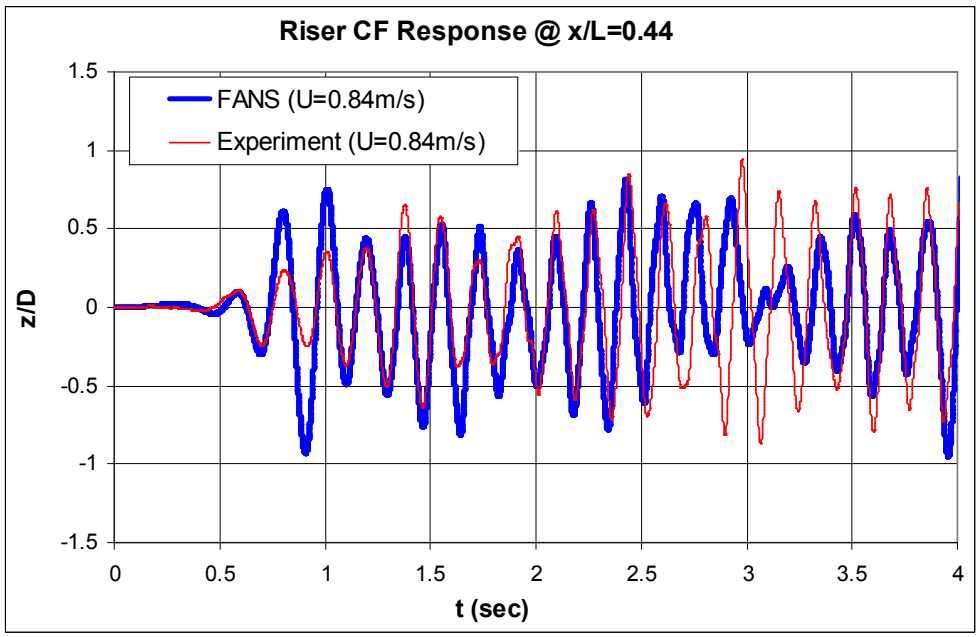

Fig. 37 Riser CF Response (U=0.84 m/s)

The riser-response rms a/D is of particular interest in the riser VIV simulations. Figs 38 and 39 show the cross flow VIV response rms a/D comparison between the simulation results and experimental data. The experimental data are plotted in dots for easy identification. It shows the CFD predicts similar response as the experimental for the U=0.42 m/s case, with only minor discrepancy in the riser lower portion. For the U=0.84 m/s case, the CFD predicts similar response range and trend as the experimental data. Note that the wave tank experiments last about 100 seconds, while in our numerical simulations, the duration is around 10 seconds.

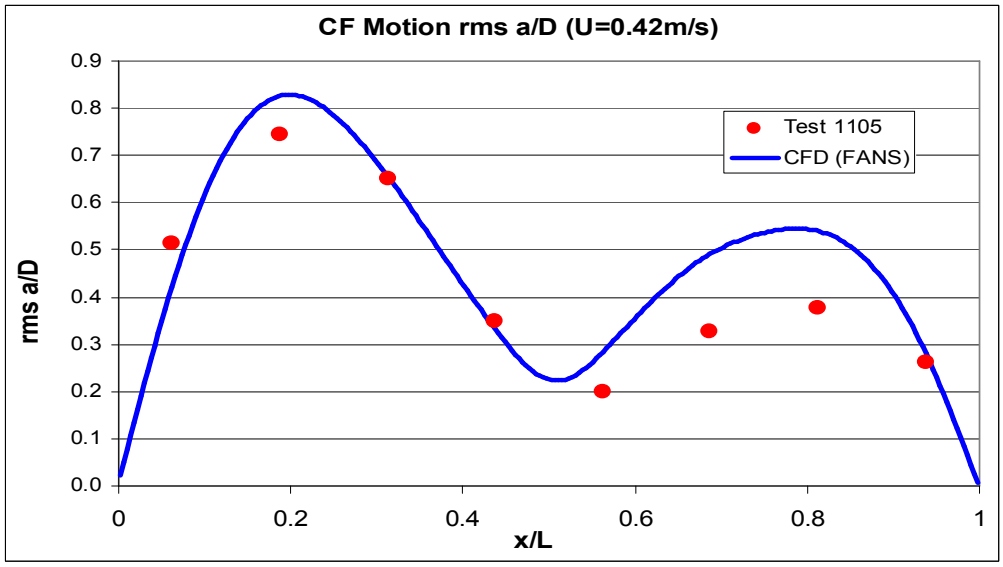

Fig. 38 Cross Flow VIV RMS a/D, U=0.42 m/s

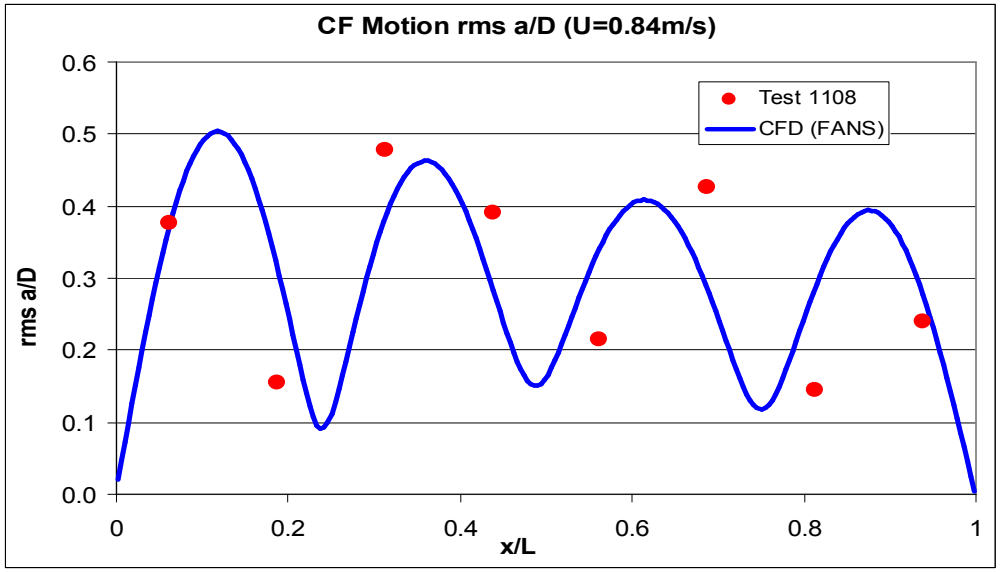

Fig. 39 Cross Flow VIV RMS a/D, U=0.84 m/s

For illustration, the riser movement trajectories for uniform current U=0.42m/s are shown in Figs. 40 and 41. We compared the riser motions at x/L=0.44, which is in the middle section of the riser. In 3D simulations, the riser usually has large deflection in flow direction due to mean drag force. And fluctuations of C_d impact the maximal displacements in z direction as well as y direction. Therefore, the riser motion trajectories show more complexity or randomness than 2D simulations. In our comparisons both the CFD and experiment show similar motion trajectory – deformed figure "8".

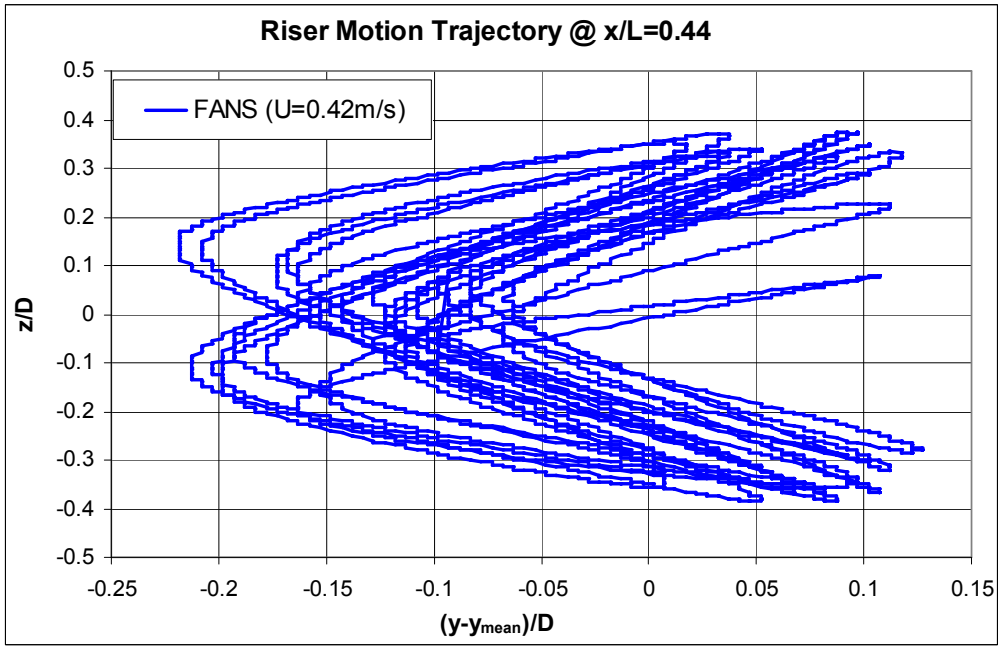

Fig. 40 Riser Motion Trajectory Comparison (CFD)

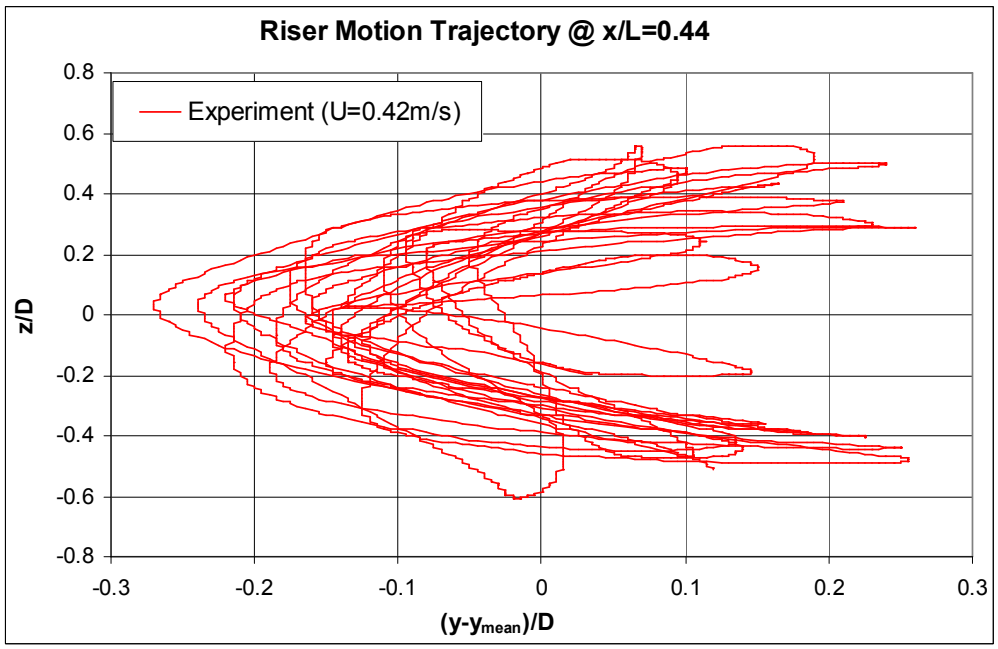

Fig. 41 Riser Motion Trajectory Comparison (Experimental Data)

Higher harmonics refer to the VIV high frequency components having integer multiple numbers of the cross flow or the in-line VIV frequency. It has been observed and measured during actual drilling operations (Tognarelli et al., 2008). Our numerical simulations provide a good tool to investigate this higher harmonics. We plotted the lift coefficient time histories for U=0.42 m/s and U=0.84 m/s, as shown in Figs. 42 to 45 . The lift coefficients are plotted in two locations on riser: x/L=0.3 and x/L=0.5. In those figures we noticed the lift coefficient time histories show the third high frequency component (3x). This indicates that the 3x harmonics could be related to the vortex shedding patterns and lift force. Fig. 46 shows the cross flow VIV PSD of the experimental data 1105. There are three peaks on the PSD graph: the cross flow dominant mode (first peak), in-line VIV (second peak), and the higher harmonics (third

peak). Fig. 47 is the plot of the cross flow VIV PSD of the CFD simulation U=0.42 m/s. It shows the same peaks, with the same frequencies as the experiments. The PSD from the CFD simulation appears to have much larger band width than the experimental data. This is due to the different time history durations for FFT analysis. The experimental data covers a fairly long duration (~100seconds) while the CFD simulations are relatively short (<10seconds). Therefore, the frequency resolution ($d\omega$) for the CFD simulation PSDs are 10 times coarser than that of the experimental data. This explains that the PSDs of the CFD simulations are wider and shorter than that of the experiments while the total energies are about the same. Theoretically the steady VIV response PSDs consist of a series of Dirac delta functions centered at each modal frequencies. In other words, only the response energies and frequencies are important. The band width of the PSDs is meaningless and does not impact the major conclusions. Figs. 48 and 49 repeat the same information for the U=0.84 m/s case. It confirms (1) the existence of the higher harmonics, and (2) the validity of using CFD time-domain simulation for further study. It is interesting to see that, based on the observation from these figures, the lift coefficients show fairly strong response at higher frequency harmonics, such as 3x. However, the motions do not show same level of the response. One possible reason is that the lift forces are acting on the riser segments locally, while the riser cross flow VIV response depends on the integrated effect of all the segments. Therefore, if the high frequency lift forces are out-of-phase with each other, then they would cancel each other and the higher harmonics would be weak. If the lift forces were synchronized along the riser, then we would expect very strong higher harmonics. Further investigation is

required to provide better understanding on this explanation, and verify under what conditions the higher harmonics will show up strong - or cause significant fatigue damages to the riser pipe. However, this part is not included in the scope of the present paper. Also this study concerns only the VIV-induced modal responses and does not study phenomenon such as traveling wave, even though it might exist in numerical simulation or experiments.

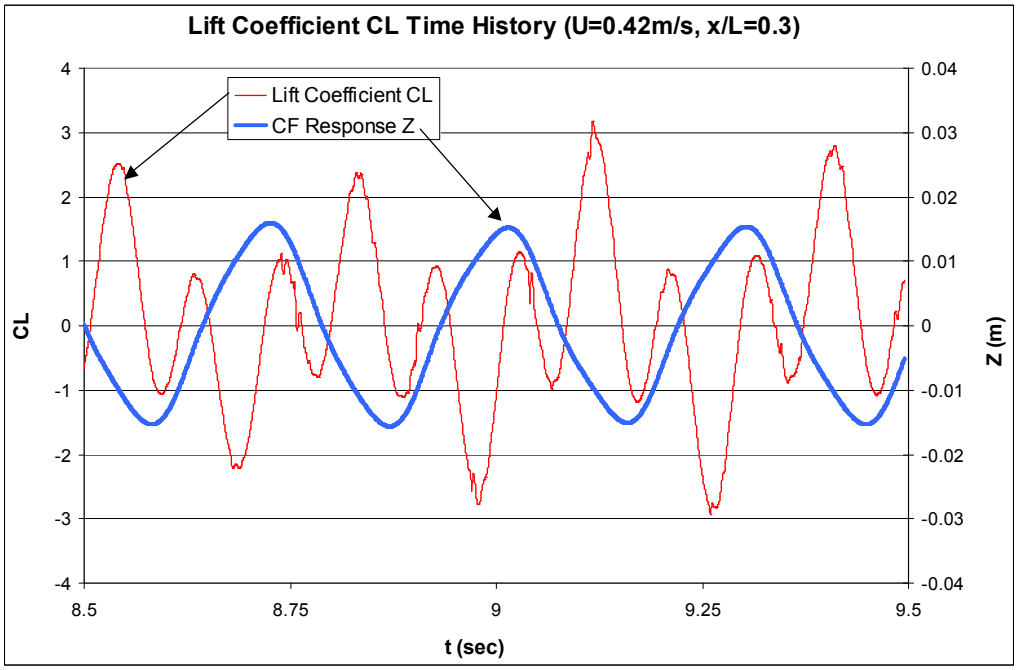

Fig. 42 Lift Coefficient (U=0.42 m/s, x/L=0.3)

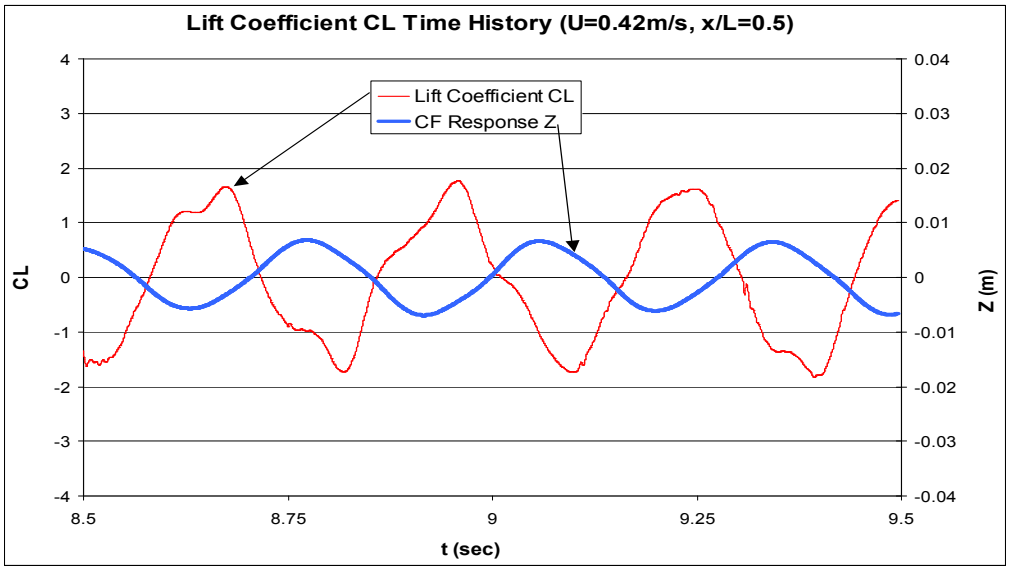

Fig. 43 Lift Coefficient (U=0.42 m/s, x/L=0.5)

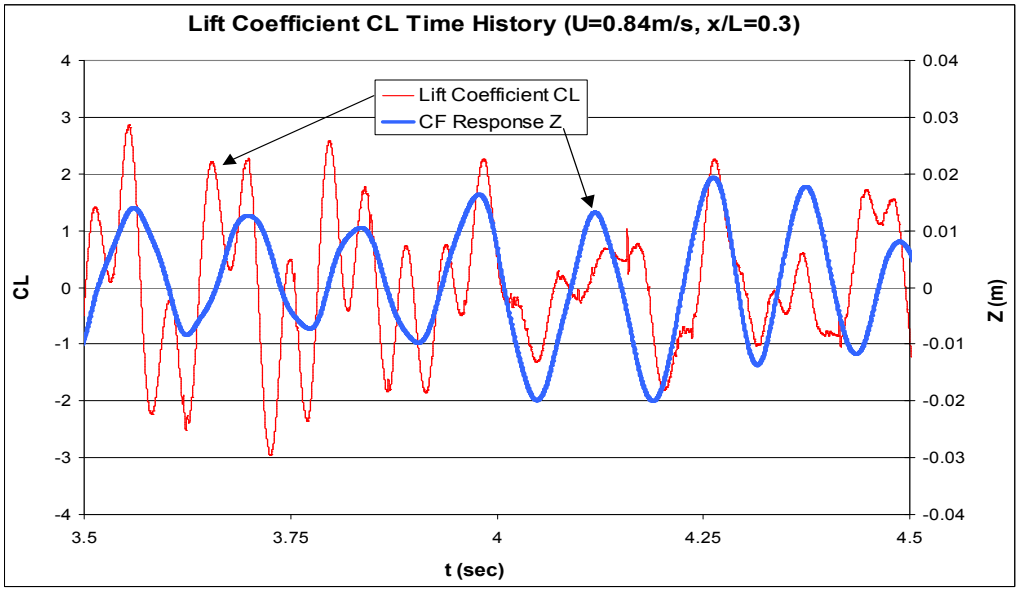

Fig. 44 Lift Coefficient (U=0.84 m/s, x/L=0.3)

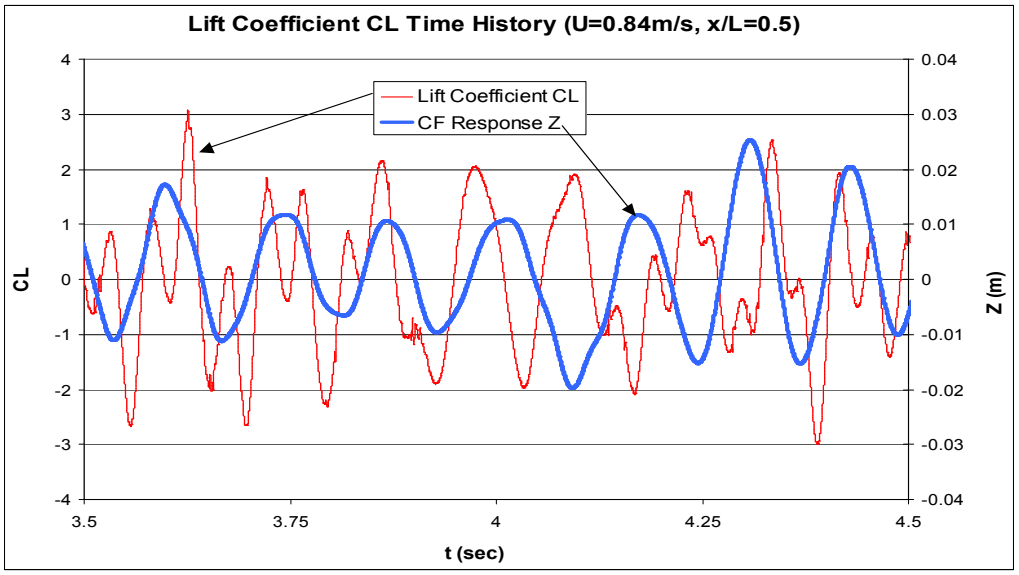

Fig. 45 Lift Coefficient (U=0.84 m/s, x/L=0.5)

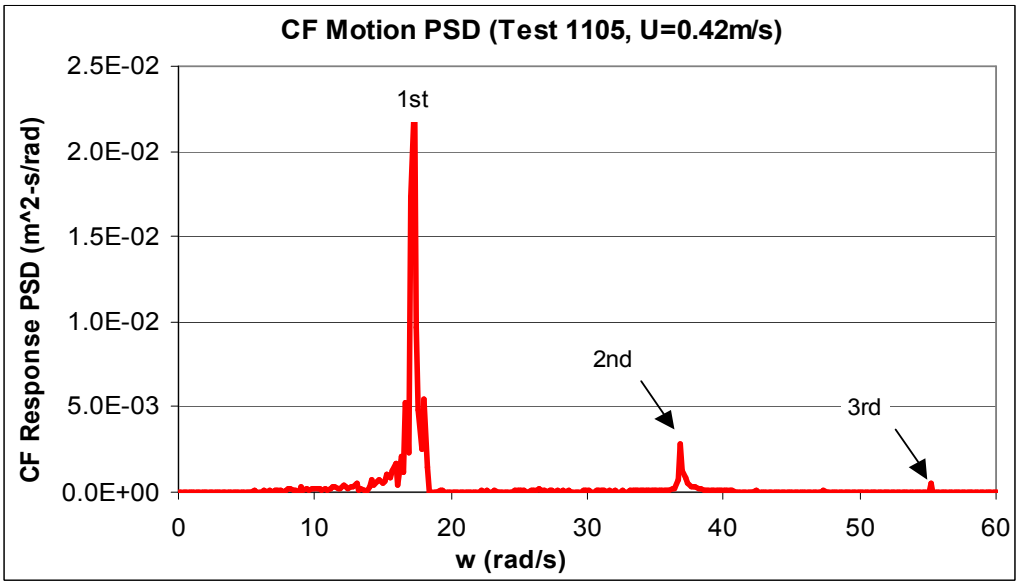

Fig. 46 CF Motion PSD (Experiment 1105)

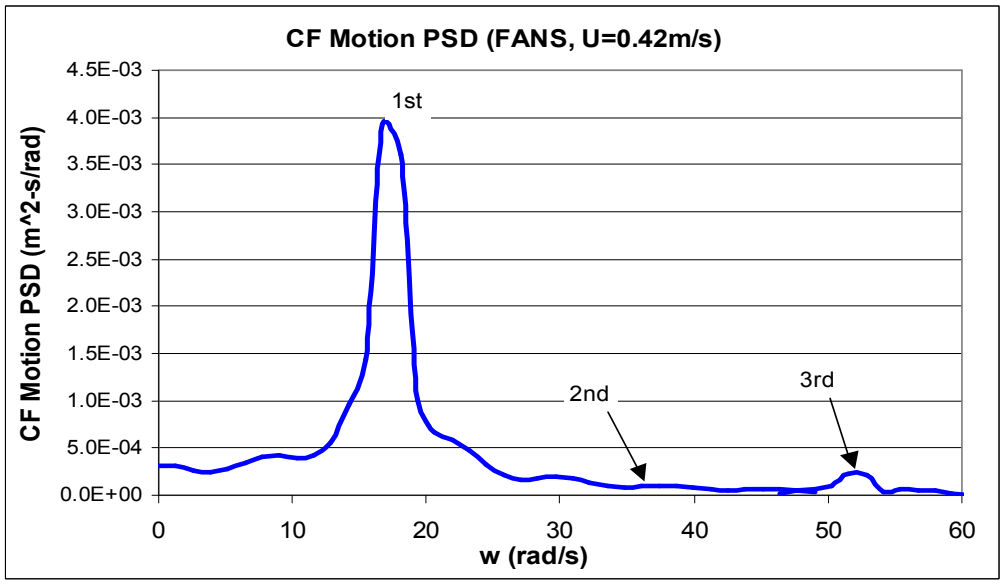

Fig. 47 CF Motion PSD (FANS, U=0.42 m/s)

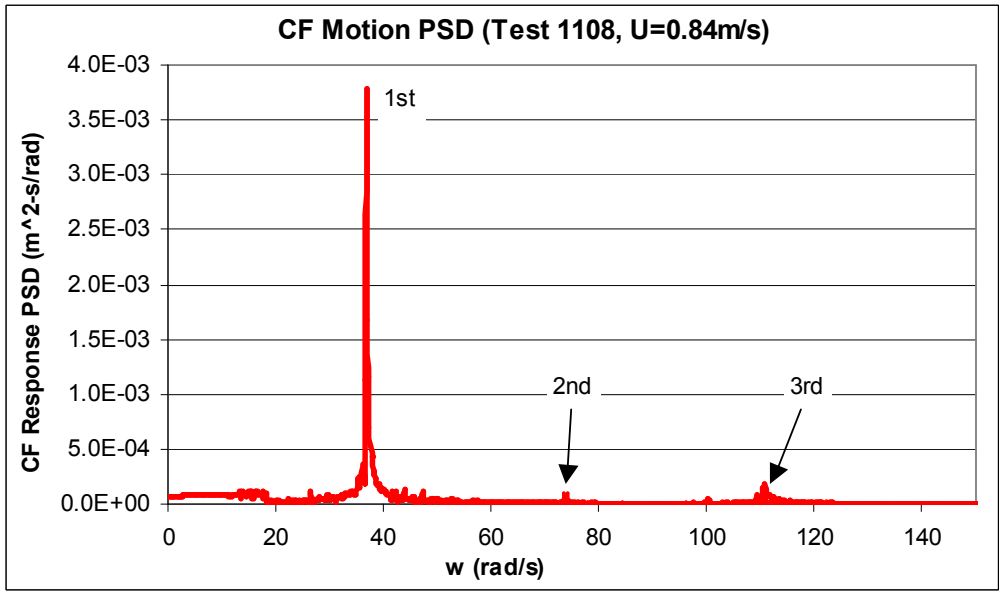

Fig. 48 CF Motion PSD (Experiment 1108, U=0.84 m/s)

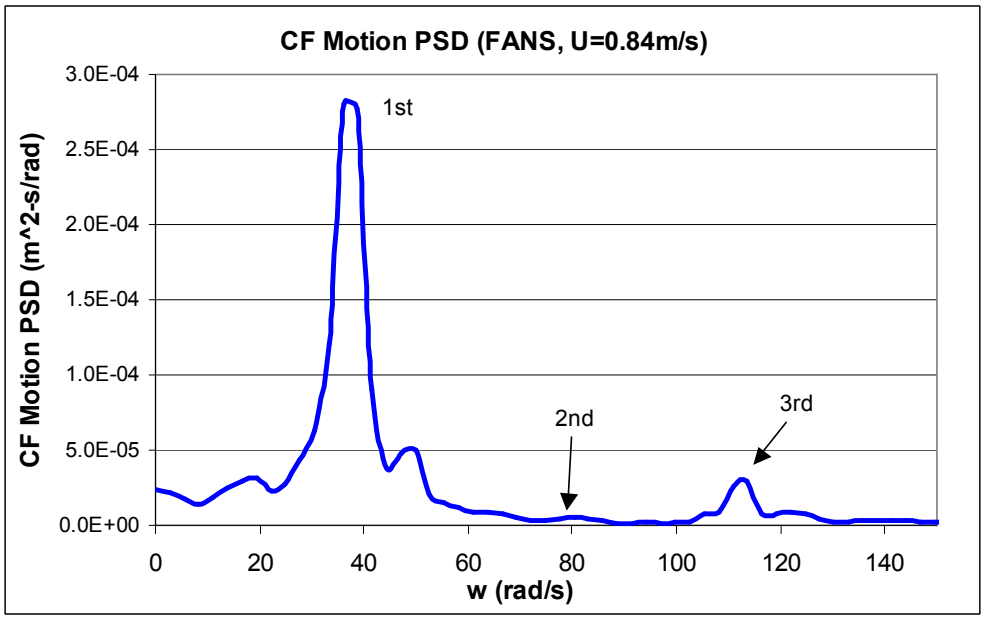

Fig. 49 CF Motion PSD (FANS, U=0.84 m/s)

Discussions

This chapter studied a long riser VIV response using an unsteady 3D, overset-grid (Chimera), Reynolds-Averaged Navier-Stokes (RANS) method. We presented two case studies with uniform current speed of 0.42 m/s and 0.84 m/s. The results agree with the published experimental data very well. It indicates that the FANS code is capable of predicting reasonable results for long risers using the refined data grids. It is worthwhile to note that FANS can be readily generalized to handle much more complex current conditions, such as highly shear current and submerged current. Some findings of the study are:

1. The vortex shedding pattern in the uniform current is mainly within the “2S” category, while its appearance varies significantly at different elevations along the riser.
2. Mode lock-in occurs in both uniform current cases. The cross flow VIV dominant frequency is similar to the riser in-water natural frequency. In other words, the modal added mass coefficients of the dominant modes are around 1.0. However, the modal added mass coefficients for non-dominant modes could vary. It is also an area deserves further study.
3. Higher harmonics have been observed in both the experimental data and the CFD numerical simulations. It is likely the 3x higher harmonics is due to the lift force high frequency components, hence the vortex shedding pattern. Further investigation is required to disclose more details on this relationship, and evaluate the impact on riser fatigue and associated mitigation options.

In conclusion, we used a CFD approach to simulate a large L/D riser VIV response in uniform current. The simulation details are presented, analyzed, and validated against the experimental data. Furthermore, it is also an effective tool for disclosing insightful data and pictures that could lead to problem identification and solutions in the riser-fluid interaction area (Huang et al. 2007a, 2007b, 2007c, 2007d).

CHAPTER V

3D SIMULATION OF FLOW PAST A VERTICAL RISER IN SHEAR CURRENT

We compared our CFD simulation results to the experimental data for the uniform currents and achieved good agreement in Chapter X. In this chapter we further compared the CFD simulation results to the experimental data for the shear currents.

In the experiment the inclined riser rotates about the rig axis. The top and bottom of the riser are positioned 0.646 m and 4.645 m away from the rotating center respectively, as shown in Fig. 50.

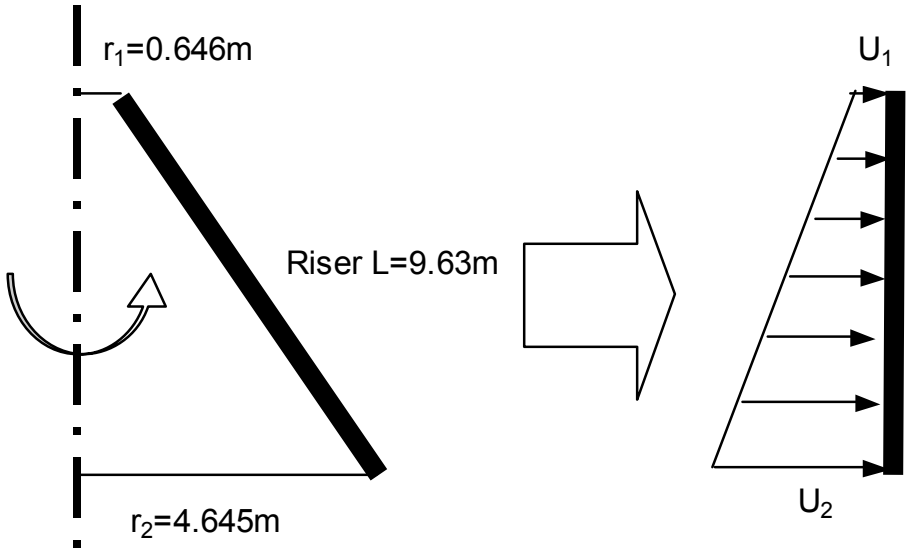

Fig. 50 Inclined Riser and Equivalent Shear Current

The shear current speed has a linear profile with U_1 at top and U_2 at bottom, where U_1/U_2=0.14. The two cases we selected for comparison are U_2=0.42m/s (test case #1205) and U_2=0.84m/s (test case #1210). During the experiment, the riser was positioned under the water. Both ends were pinned to the test rig, which rotates at a constant angular velocity. This would simulate a linearly shear current condition. Note that after the rig completes one cycle, the riser moves into its own wake field. This fluid disturbance is expected to be negligible and not considered in our numerical simulations.

Simulation Results

The vortex shedding and riser motions are visualized for all the simulations. Fig. 51 shows some of the video frames illustrating the riser deflections and axial vorticity contours. Nearly all of the vortices follow "2S" pattern. The vortices develop at the riser bottom first because it is subject to the highest current speed. The risers have in-plane deflection due to the current induced drag force. The largest deflection is less than 10D, which is relatively small comparing to the L/D (=482) and validates the tensioned beam equation for riser motion calculation. For the case U_2=0.42 m/s, the 2^{nd} mode dominates the cross flow VIV. While for the case U_2=0.84 m/s, the 4^{th} mode is dominant. The riser has a fundamental frequency of about 1.5 Hz. Therefore, the 2^{nd} mode has a frequency of 3Hz, and 4^{th} mode has a frequency of 6 Hz. To accurately simulate the VIV in such high frequency, the time step has to be sufficiently small. The finest time step we used is approximately 0.0002 s. The duration of all the simulations is 40,000 time steps. Top

views of the vibrating riser and its vortex contours are shown in Figs 52 and 53 for U_2=0.42 m/s and U_2=0.84 m/s respectively.

We compared the riser cross flow motion time histories to the experimental data in Figs. 54 and 55. The time histories start with a stationary riser. After it is exposed to a shear current, the riser begins to vibrate in cross flow direction. Figs. 54 and 55 compared a fully developed segment of the simulations to the experimental data. The comparisons show general agreements on the VIV amplitudes and frequencies. The time histories show the riser cross flow vibration is periodical but with varying amplitudes. Usually this indicates more than one mode exists.

The riser motion rms a/D is also an important parameter. Figs. 56 and 57 show the comparisons to the experimental data for test case 1205 (U_2=0.42 m/s) and test case 1210 (U_2=0.84 m/s). In these comparisons we filtered out the 1st order response to avoid the riser sagging effect due to its own weight. For case 1205, the CFD simulation matches the VIV response shape while slightly over-predict the cross flow motion. For case 1210, the CFD simulation predicts similar motion rms while with slightly different modal components. Overall, the comparisons show good agreement and demonstrate strong correlation between the CFD results and experimental data.

Figs. 58 and 59 show the riser cross flow VIV PSD of experimental results and CFD simulation respectively. Both of them show the 2nd mode dominate the cross flow VIV (U_2=0.42 m/s). Fig. 60 and 61 show the PSDs for U_2=0.84 m/s. In this case the CFD method predicts that the 4th mode is the dominant mode, while the experimental data indicates that both the 3rd and 4th modes are excited, with the 3rd mode more dominant than

the 4th mode. A possible reason could be the added mass variation. In the experiment the riser was rotating, therefore, its cross flow added mass could be also influenced by the rotations, especially when the rotational speed is high. Nevertheless, the comparisons are very encouraging despite of the discrepancies.

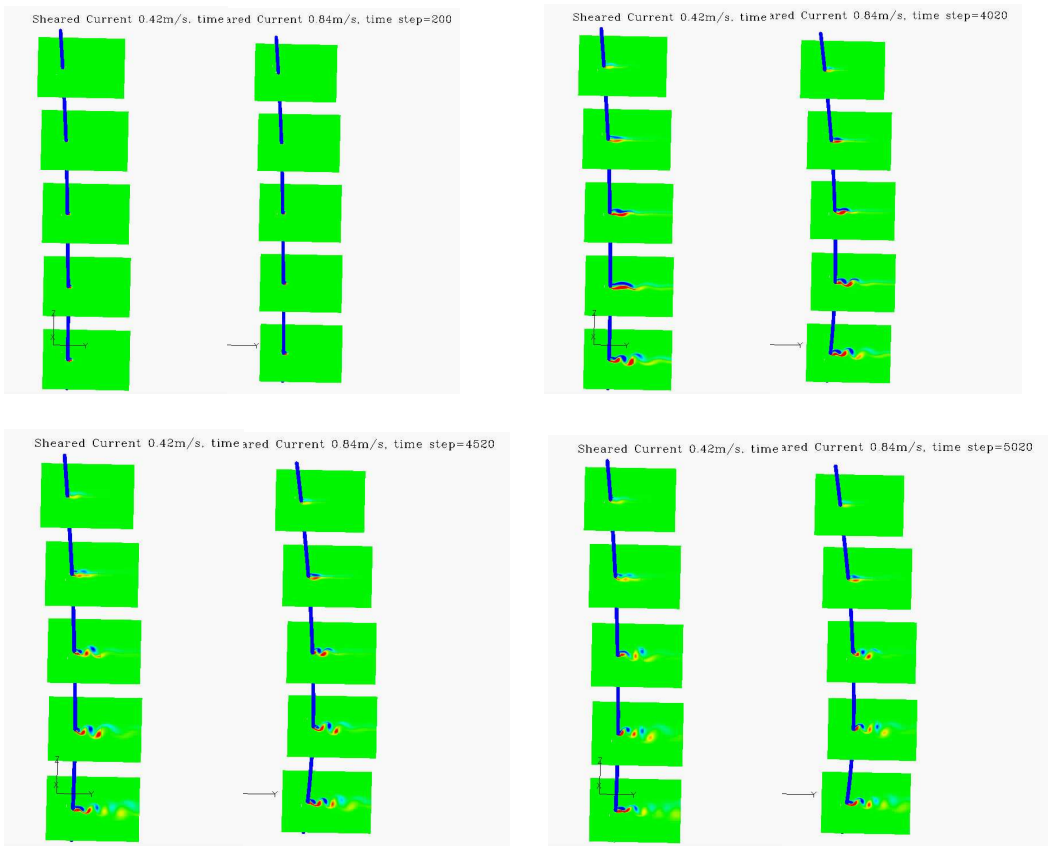

Fig. 51 Riser VIV Evolution, Left: U_2=0.42m/s, Right: U_2=0.84m/s

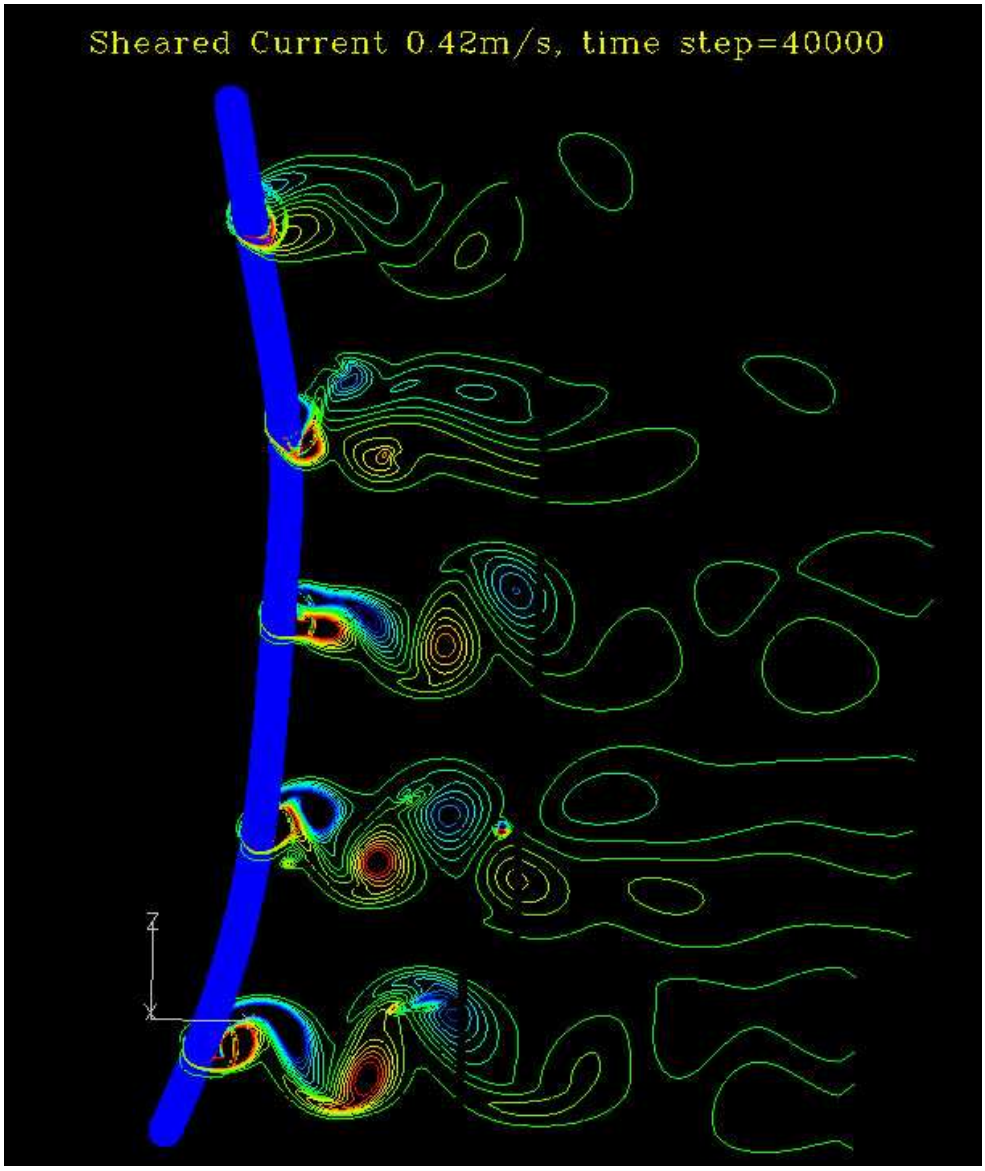

Fig. 52 Riser VIV Snapshots, U_2=0.42m/s

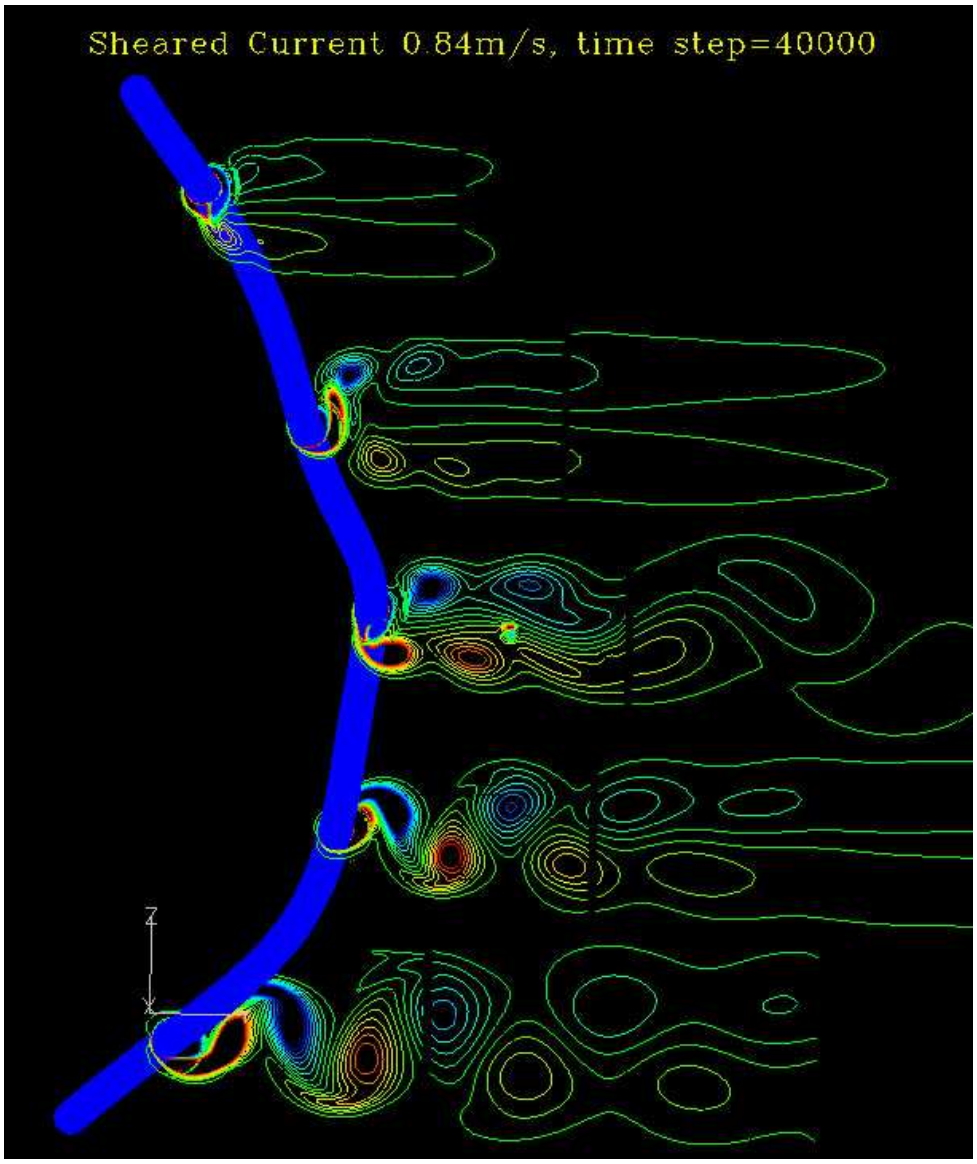

Fig. 53 Riser VIV Snapshots, U_2=0.84m/s

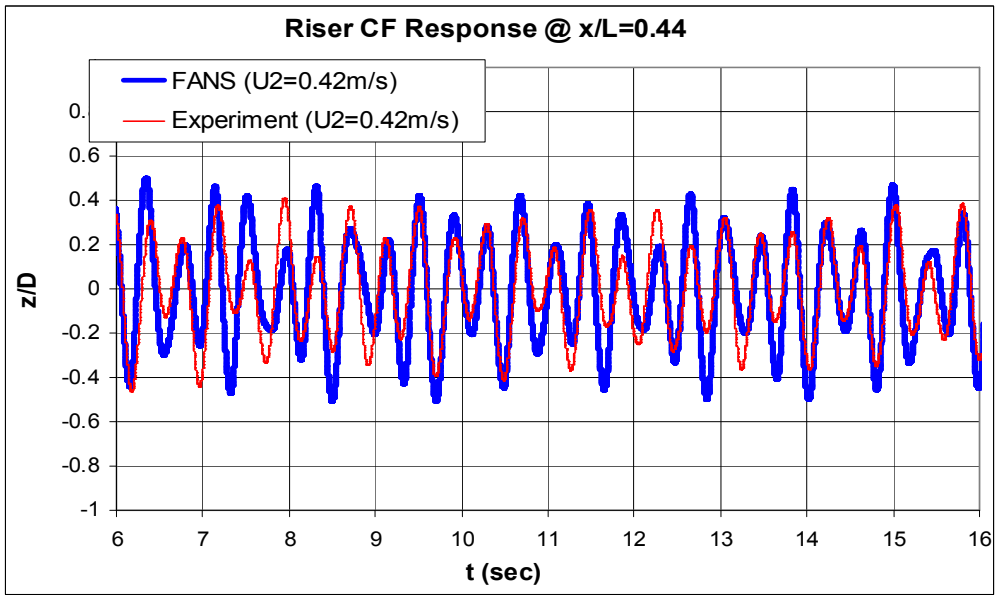

Fig. 54 Riser Cross Flow Response Time History (U_2=0.42m/s)

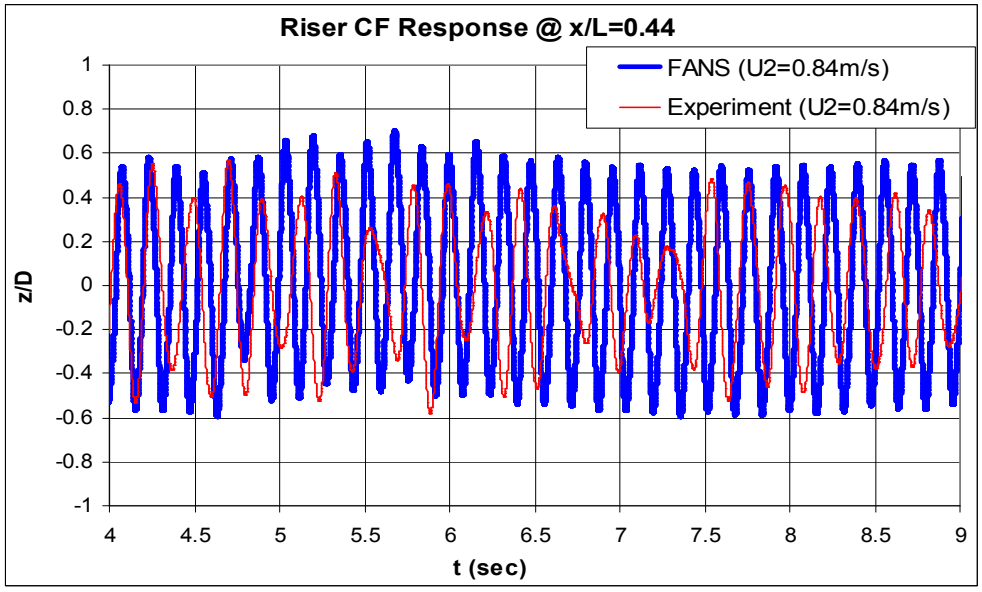

Fig. 55 Riser Cross Flow Response Time History (U_2=0.84m/s)

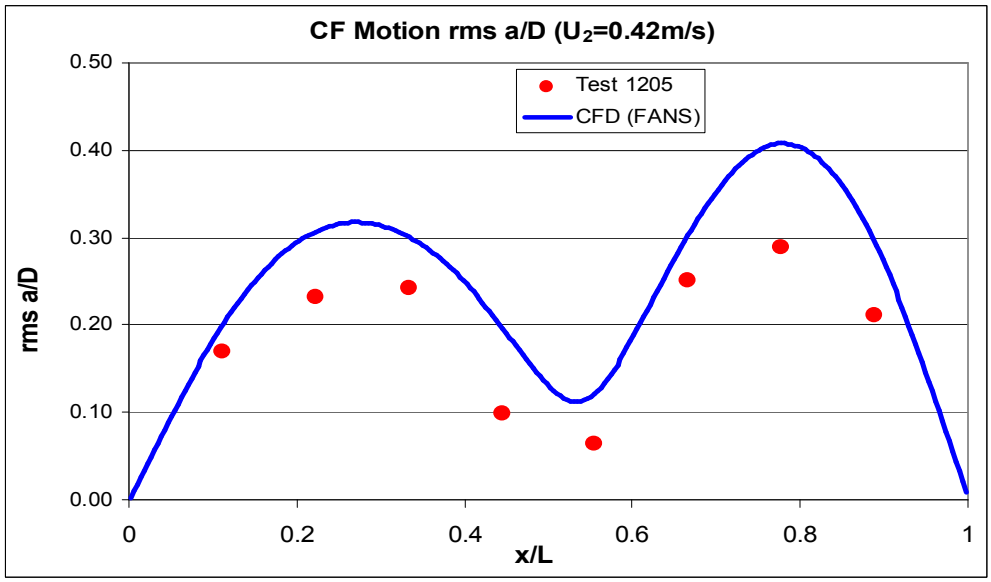

Fig. 56 Riser Cross Flow Response rms a/D (U_2=0.42m/s)

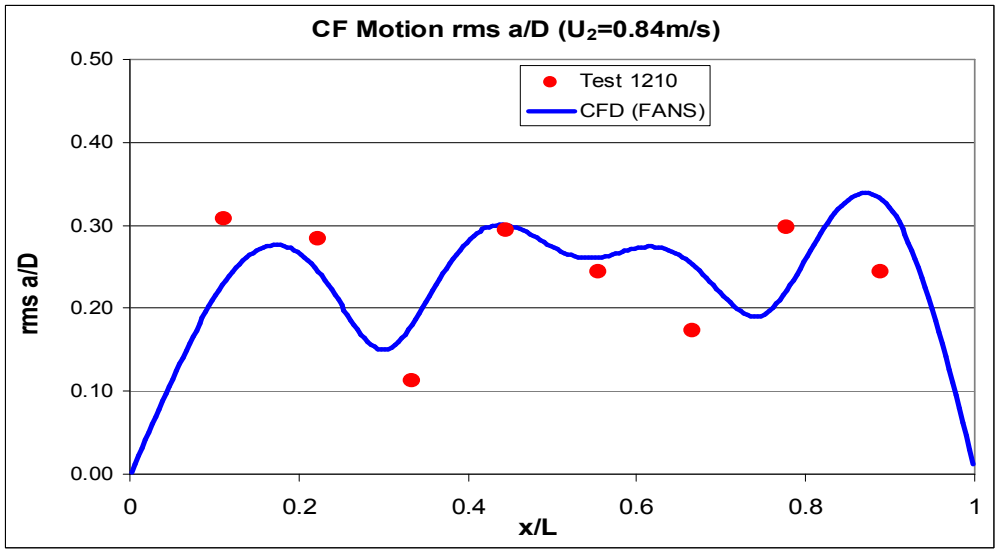

Fig. 57 Riser Cross Flow Response rms a/D (U_2=0.84m/s)

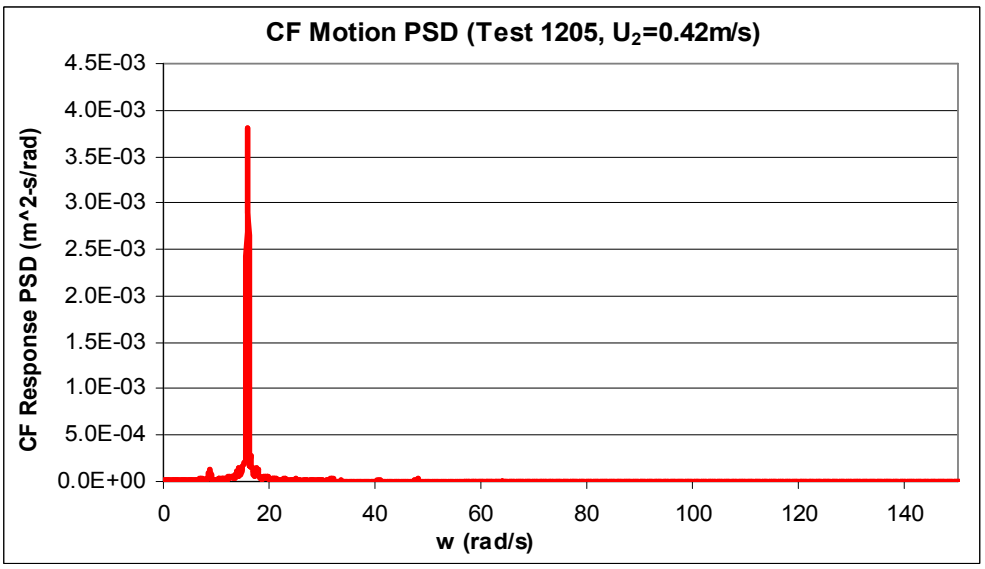

Fig. 58 Riser Cross Flow Response PSD (Test 1205, U_2=0.42m/s)

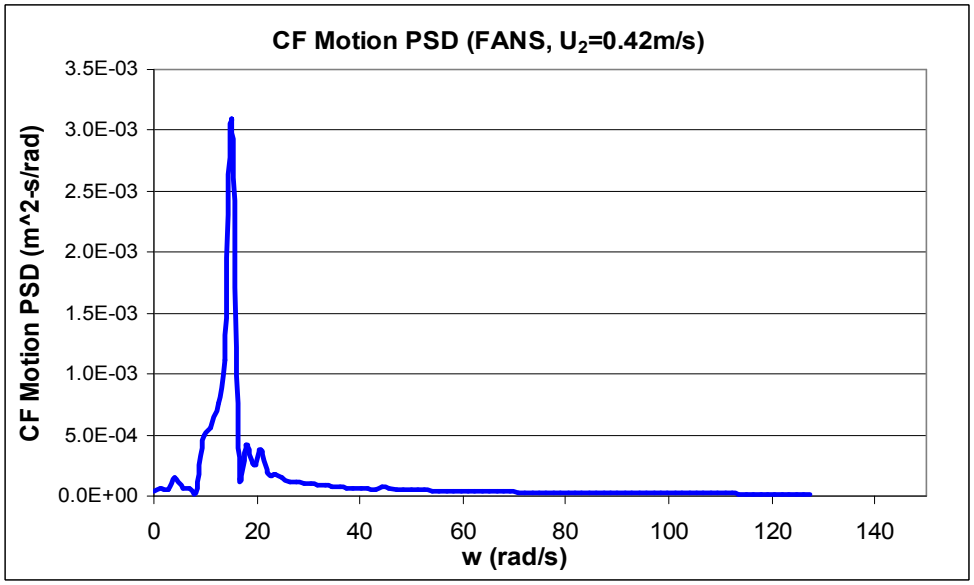

Fig. 59 Riser Cross Flow Response PSD (CFD, U_2=0.42m/s)

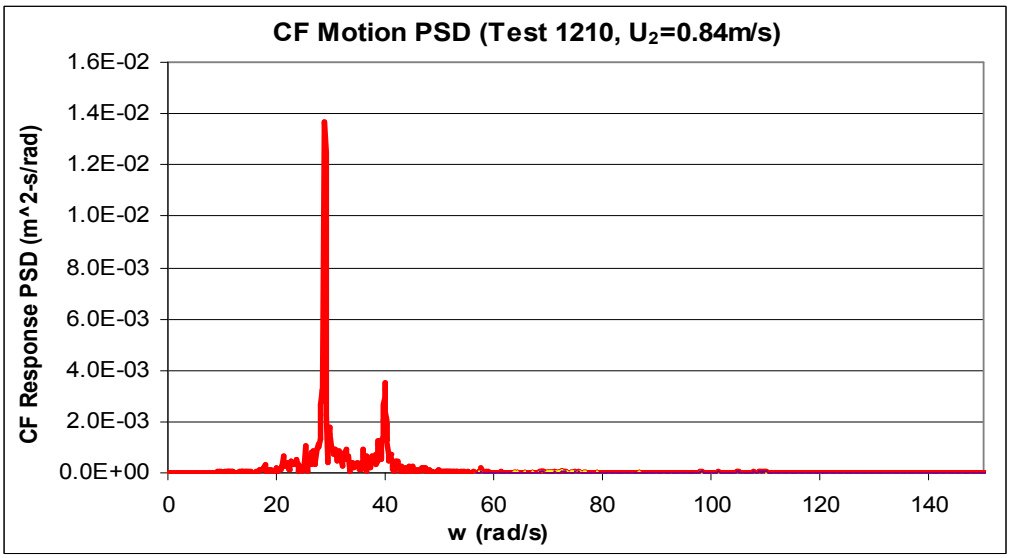

Fig. 60 Riser Cross Flow Response PSD (Test 1210, U_2=0.84m/s)

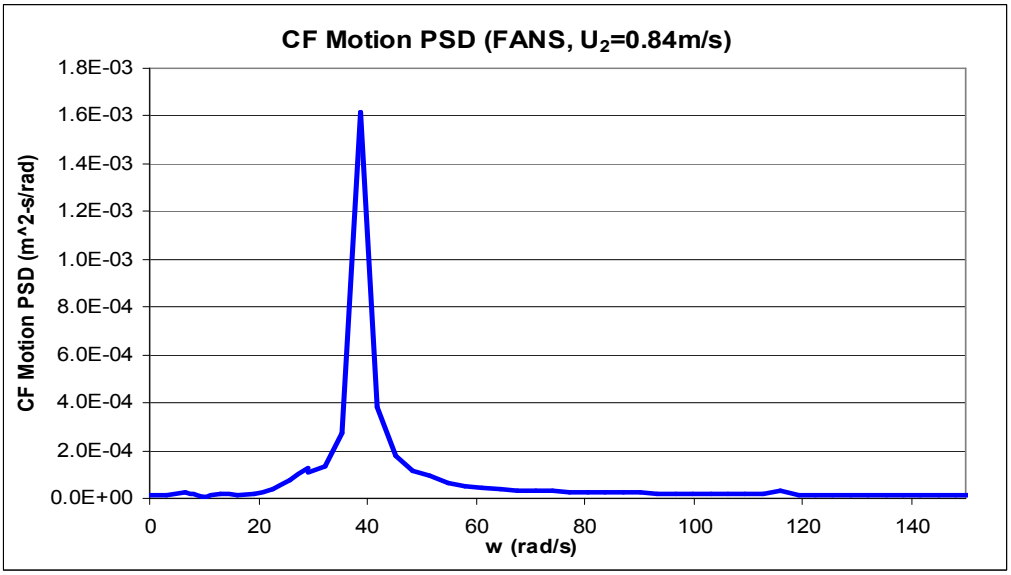

Fig. 61 Riser Cross Flow Response PSD (CFD, U_2=0.84m/s)

The CF VIV induced fatigue damage index along the riser was calculated and compared to experimental results (from stain gages) in Figs. 62 and 63 for U_2=0.42m/s and U_2=0.84m/s respectively. The comparisons show that the fatigue damages are comparable between the CFD simulation and experiments. In general the CFD code predicts slightly higher fatigue damage than the experiment. It is worthwhile to note that both CFD simulations and experiments show that the fatigue damage distributions on the riser are not symmetric along the axial direction. One possible reason is the involvement of the non-dominant modes. The non-dominant modes themselves contribute very small fatigue damages. However, when they are superimposed to the dominant mode, their influence is amplified by approximately 3 times (for single slope S-N curve with m_1=3), hence is able to noticeably change the fatigue distributions. Overall, the CFD approach provides satisfactory results. And the comparisons confirm the feasibility of fatigue assessment using CFD time domain simulation approach.

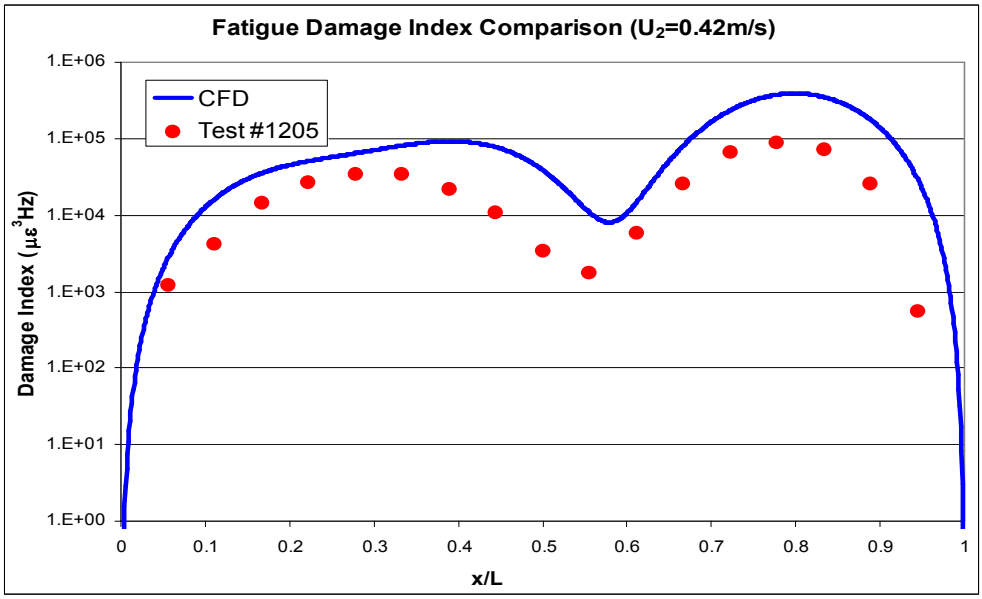

Fig. 62 CF Fatigue Damage Index Comparison (U_2=0.42m/s)

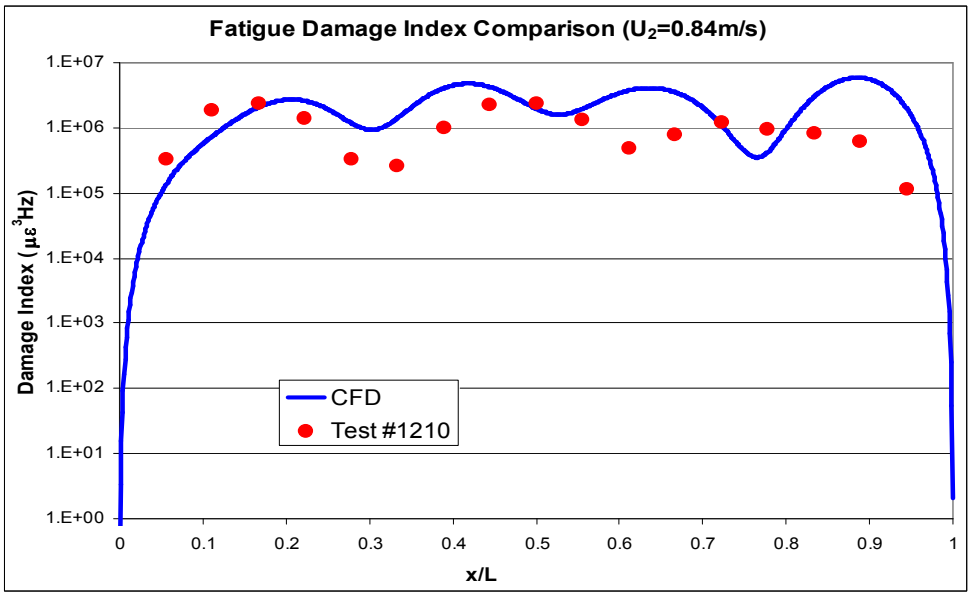

Fig. 63 CF Fatigue Damage Index Comparison (U_2=0.84m/s)

Discussions

In this chapter we have simulated a vertical riser VIV response in shear currents, and compared to the experimental data. The riser has aspect ratio L/D of 482. The fluid-riser interactions are computed and visualized in time domain. Based on that we calculated the cross flow VIV induced stress and fatigue damage index, and compared the fatigue results to experimental results. Some of the findings from the study are:

1. The CFD simulations of riser VIV show similar response as the experimental data. We compared the important parameters, including motion time histories, rms a/D, and PSDs. General agreements have been observed. The CFD approach could slightly over-predict the response amplitudes.
2. Linearly shear current with higher speed tends to excite more modes. The dominant mode contributes most to the VIV induced fatigue, while the non-dominant modes could also influence the fatigue damage considerably by enhancing or canceling the peak values. Both CFD simulation and experiments show non-symmetric fatigue damage distributions along the riser.

3. In our studies cases, the vortex shedding generally follows “2S” pattern. The vortex shedding frequencies along the riser corresponds to the dominant modal frequency. While the vortex traveling speed varies along the riser, or the vortex travels faster in the riser bottom (higher current speed) than in the riser top (lower current speed).
4. The VIV induced fatigue distribution along the riser is usually different from the motion amplitude distribution. The fatigue is not only sensitive to the modal response amplitudes, but also sensitive to the modal frequencies. Therefore, to predict accurate fatigue damages it is important to accurately predict the responses of both the dominant mode and the non-dominant higher modes.

In summary, the CFD approach provided reasonable results for the studied cases on a 9.63m vertical riser in shear current (Huang et al. 2007a, 2007b, 2007c, 2007d).

CHAPTER VI

3D SIMULATION OF FLOW PAST A HORIZONTAL RISER IN UNIFORM CURRENT

This chapter presents the study results on a horizontal riser (L/D=1,400), which was the subject of a recently experiment conducted at Marintek's Ocean Basin in Trondheim (Trim et al. 2005). Fig. 64 shows the testing schematics plan view. The riser model has a mass ratio of 1.6, and length of 38 m. It is towed through the wave basin to generate desired current conditions. The testing was performed under different the current conditions, i.e. uniform and shear current. Some experimental data are published in Trim's paper (2005).

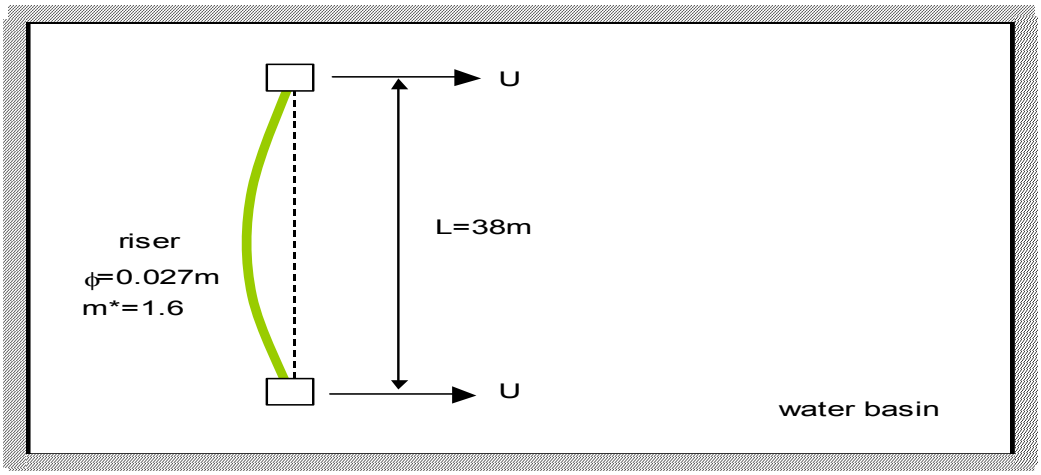

Fig. 64 Riser VIV Testing Plan View Schematics

In this chapter we intended to further demonstrate that the long riser VIV could also be analyzed by using Chimera (overset grid) technique embedded CFD approach.

The studied riser is positioned horizontally with uniform sectional properties and constant tension. Its two ends have pinned connection boundary conditions. In such case its modal shapes follow sinusoidal functions and are well defined by simple analytic formula. A uniform current of 0.4 m/s and 0.8 m/s are applied to the riser respectively, the riser response is then calculated in time domain for sufficiently long durations. The simulation results are compared to the published experimental data and CFD results.

The flow field around a riser is calculated by numerically solving the unsteady, incompressible Navier-Stokes equation. The turbulence flow was solved using Large Eddy Simulation (LES) with Smagorinsky subgrid-scale turbulence model. The Reynolds numbers are $8x10^3$ and $1.7x10^4$ for U=0.4 m/s and U=0.8 m/s respectively.

The non-dimensional time step used in the simulation is 0.01, which means the free stream fluid travels a distance of one riser diameter in 100 time steps. The dimensional time steps are about 0.0007 seconds for U=0.4 m/s current, and half of that for U=0.8 m/s current. Considering that both the vortex shedding frequency for the fixed riser and the vibrating frequency of the riser are less than 3 Hz, this time step is sufficiently small.

Overset grid (Chimera) technique provides an effective way to handle riser movement. Figs. 65 and 66 show the structured data grids used in this study. The body grid has a dimension of 182 x 41 x 30, the wake grid has a dimension of 200 x 101 x 30, while the background grid is artificial. It provides boundary conditions to the wake grid, but does not involve in numerical iterations. Therefore, it is not shown in the figures. The data grids have a total of slightly less than 1 million elements, and have been delicately generated with very fine grid sizes at the riser boundary layer and vortex shedding zones. In this study the wake grid is set to move with the riser, which eliminates the relative movement between the riser body grid and wake grid. As a result, the overlapping region depends on only the riser initial position, and the interpolation coefficients between these two grids needs only to be determined once throughout the simulation. Fig. 65 illustrates the data grids when riser is at its initial position (not deflected) and deformed due to current loadings. Fig. 66 shows the grid details around/along the riser surface.

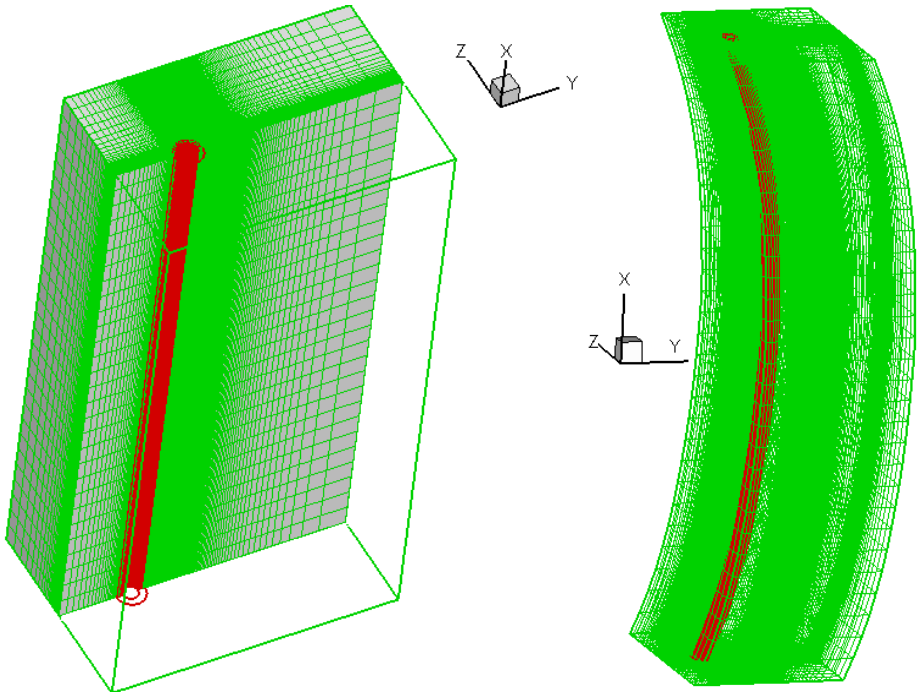

Fig. 65 Data Grids in 3D, Left: Undeformed Riser, Right: Deformed Riser

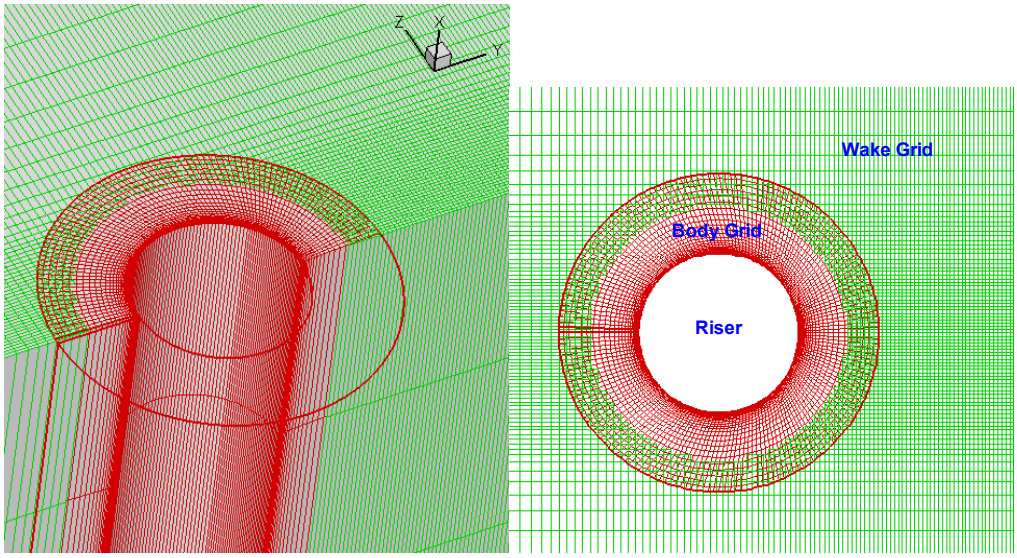

Fig. 66 Data Grid Near Riser Surface

The simulation starts with an initial uniform flow on the background data grid. The riser deflects toward the current direction until its internal restoring force overcomes the current drag force. After a certain period of transitional dynamics, it then oscillates about its equilibrium position. The riser motions were solved using the modal solver. Both inline and cross flow motions are included in this study.

Simulation Results

We started the riser VIV simulation with an initially straight riser. Because it is subject to the mean drag force, the riser deflects toward the downstream direction. The maximum riser deflections occur at the middle section, with values of approximately 5D and 20D for current speed 0.4 m/s and 0.8 m/s respectively. Fig. 67 shows the evolution of this deflection and the vorticity of the flowing field around the riser. The results indicate that the riser approaches near its equilibrium position after 6,000 time steps (current travels a distance of 60D), and its inline vibrating amplitudes are small comparing to the riser mean deflections. The figure also shows the vortex shedding at different locations along the riser can be either in phase or our-of-phase. Majority of the vortex shedding show clear 2S pattern. Occasionally coalescence of vortex (C pattern) occurs near top and bottom regions. This indicates that the riser is self-exciting most of the time throughout the whole riser span.

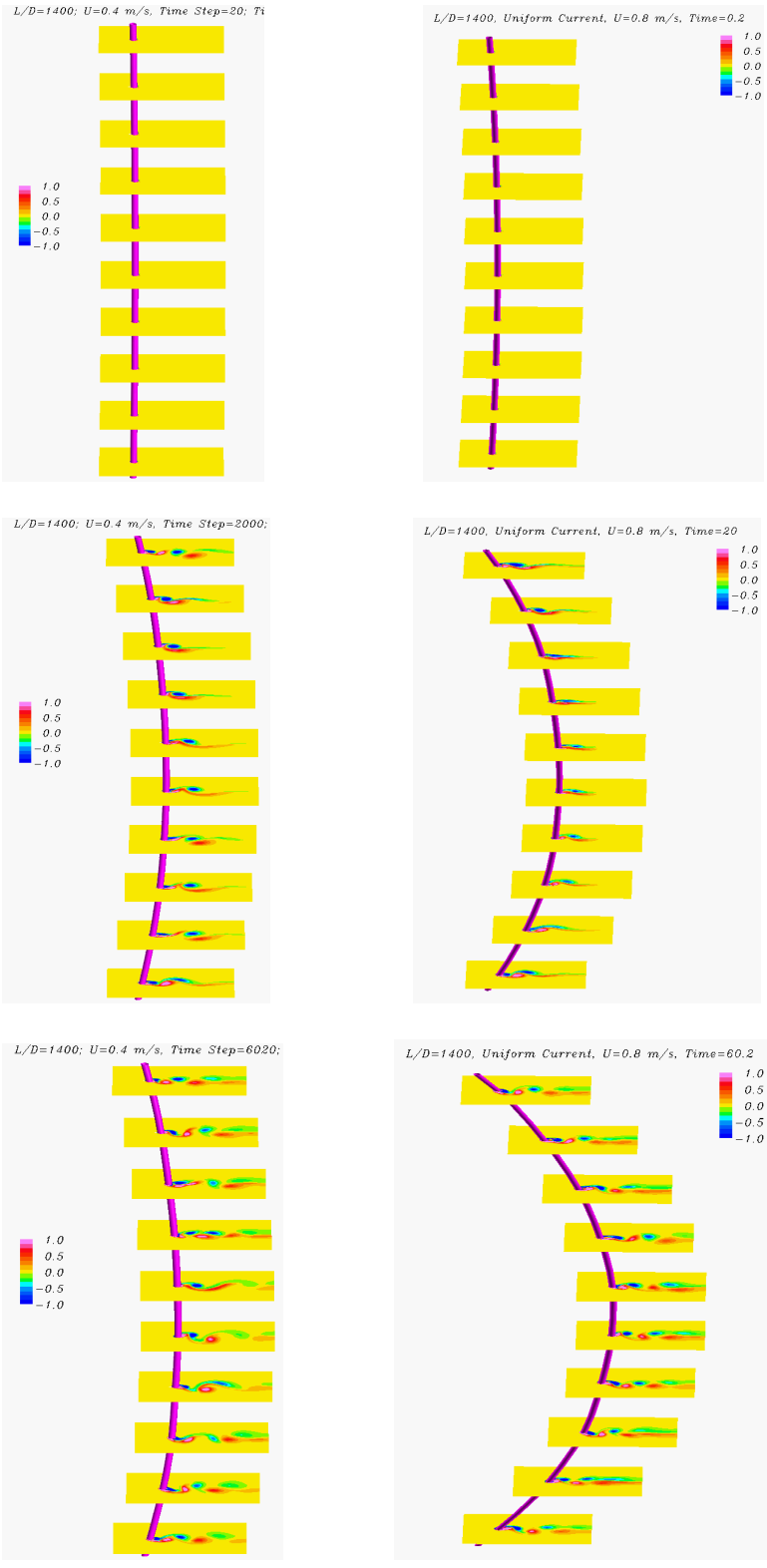

Fig. 67 Riser VIV Evolution, Left: U=0.4m/s, Right: U=0.8m/s

Figs. 68 and 69 present the riser and flow field vorticity contour snap shots for U=0.4 m/s and 0.8 m/s respectively. Only 5 sectional planes are shown. It confirms that the vortex shedding at different riser sectional stations are synchronized with the riser motions. Furthermore, it also illustrates the riser VIV response in 3D, including in-line and cross flow vibrations. It is interesting to see the large riser mean deflections in flow direction. We noticed that this in-line deflection could affect the riser VIV responses, both in-line VIV and cross flow VIV. To illustrate this, we plotted the 1st mode response time histories in Figs. 70 and 71 for U=0.4 m/s and 0.8 m/s respectively. It shows that:

- The 1st mode amplitude approaches a large mean value, i.e. 5.2D for U=0.4 m/s, and 23.3D for U=0.8 m/s. Note that the mean value increases by approximately 4 times when current velocity doubles, which is as expected since the current loading is proportional to the square of the speed. Also note that the 1st mode response is different from the riser response. The former is only a component of the later.
- The 1st mode amplitude decays very slowly, if it decays at all. It oscillates about its mean value with a standard deviation of 0.4D and 1D for U=0.4 m/s and 0.8 m/s respectively. Therefore, it seems the 1st mode dynamics is intrinsic and somewhat proportional to the incoming current speed. These standard deviations are in the same order of magnitude with the riser diameter, and obviously comparable to the in-line and cross flow VIV amplitudes.

Other low order modes, i.e. the 2nd and 3rd modes, also show similar trend. The higher order the mode is, the lower the mean and standard deviation are. The existence of these low order modes complicates the riser VIV phenomenon. This also implies that the riser deflection will influence its own VIV. This effect can easily be studied and evaluated further with time domain simulation approach.

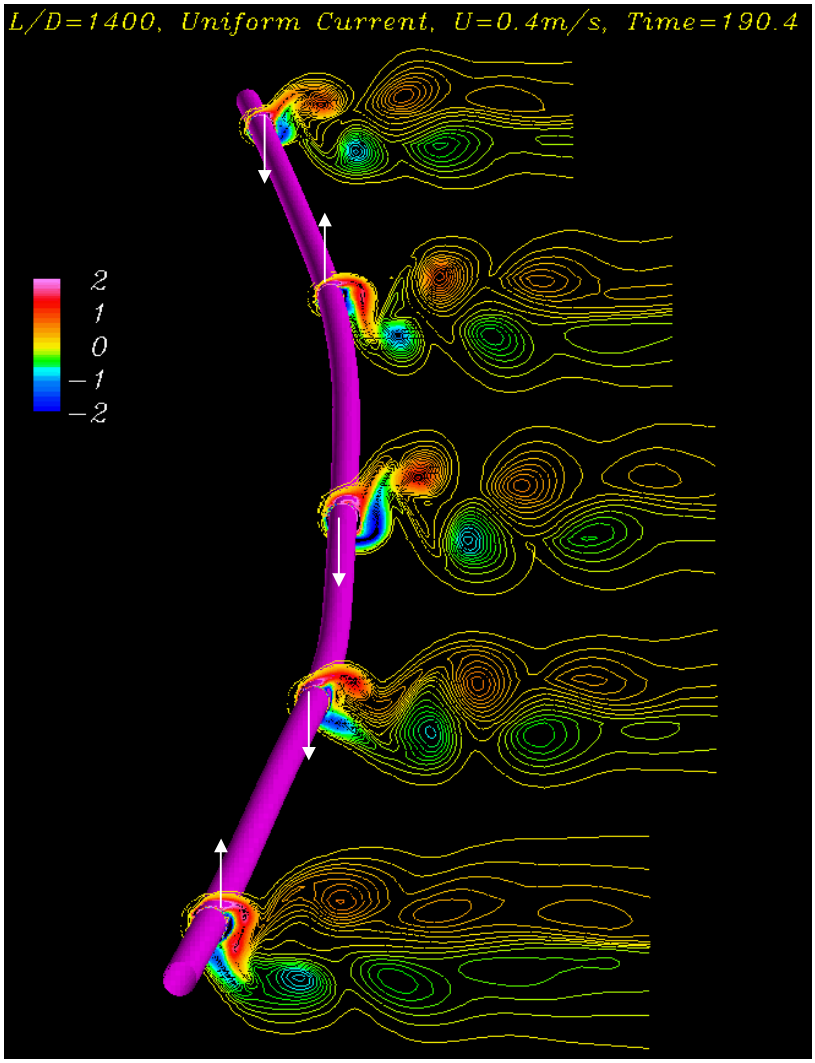

Fig. 68 Riser VIV Snap Shots (U=0.4m/s)

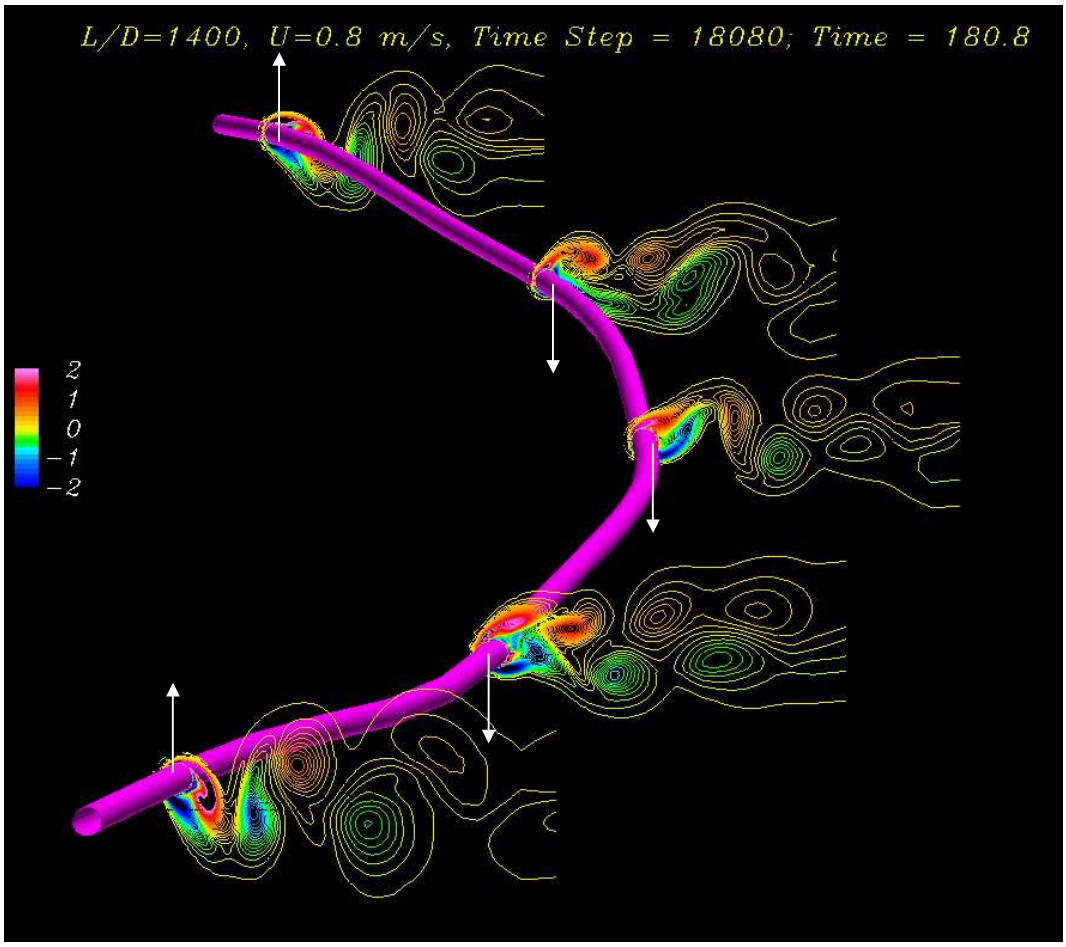

Fig. 69 Riser VIV Snap Shots (U=0.8m/s)

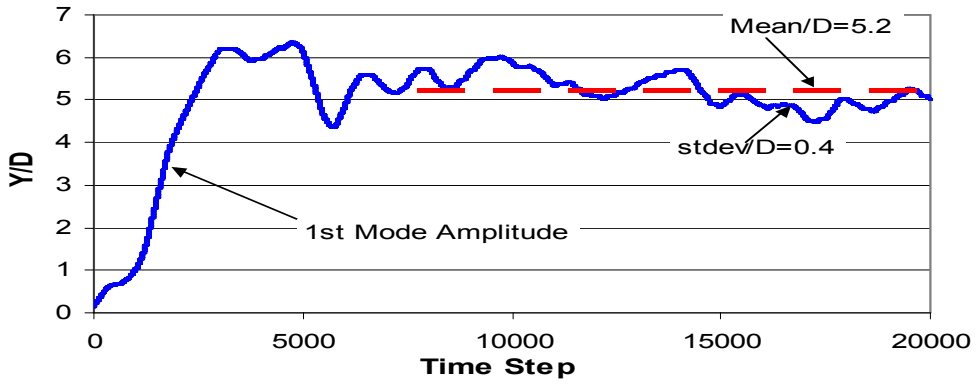

Fig. 70 In-Line Modal Response (U=0.4m/s)

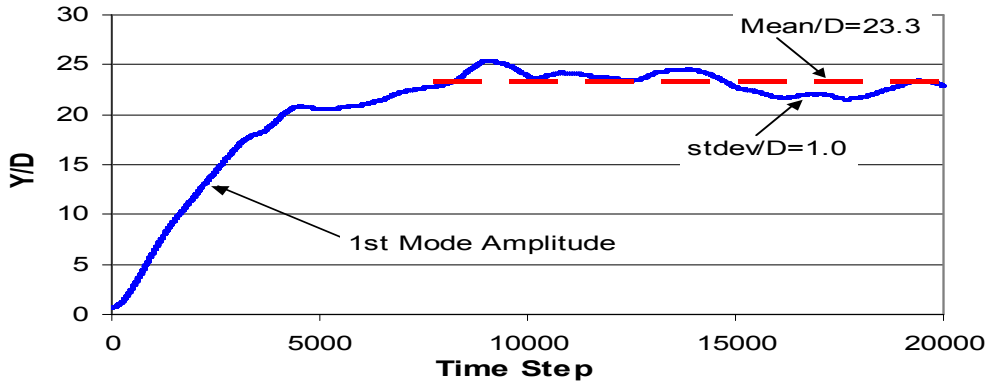

Fig. 71 In-Line Modal Response (U=0.8m/s)

Drag and lift coefficients are calculated at each time step along the riser. Fig. 72 shows the mean drag coefficient distributions. The drag coefficients are calculated based on global current velocity and have mean values between 1 and 2.5. By comparing the mean Cd distributions to the riser cross flow VIV amplitude envelopes (shown in page

114 and 115), we found they are correlated to each other. The higher the cross flow VIV amplitude is, the higher the averaged Cd is. It also shows that higher current speed does not necessarily cause higher drag coefficients. Fig. 73 shows the lift coefficient RMS distributions. The lift coefficients tend to have more evenly distributed, but lower RMS values along the riser at higher current speed. This would explain the dominant mode response amplitude usually decreases when the current speed increases. In other words, higher order modes are excited in higher speed current, but likely with lower vibrating amplitudes.

Fig. 74 shows the riser motion trajectories at different elevations for U=0.4 m/s and 0.8 m/s. The riser is first pushed downstream to certain distance. It then oscillates laterally in both in-line and cross flow directions. Note that the mean positions are different at different riser elevations. Figs. 75 to 77 show the amplified views of the riser motions at x/L=0.15, 0.35 and 0.55 for U=0.4 m/s. The figure "8" movement pattern is clearly observed at riser top and bottom regions ($x/L \approx 0$ or 1), and is less obvious at riser middle sections ($x/L \approx 0.5$). A possible reason is the large riser deflection effect as we discussed in previous sections. Figure "8" pattern is usually seen in 2D or 3D rigid cylinder VIV simulations, where the cylinder mean Cd is independent of the riser elevations. For a long and flexible riser, its mean Cd depends also on the space, i.e. x/L. This introduces more complex pattern of riser in-line movement. On the other hand, when the riser has a large lateral deflection, even very slight change of drag force could cause the riser's in-line deflection to fluctuate up to several diameters and break the

figure “8” pattern. As a result, the riser motion trajectory pattern is complicated by the riser lateral flexibilities as well.

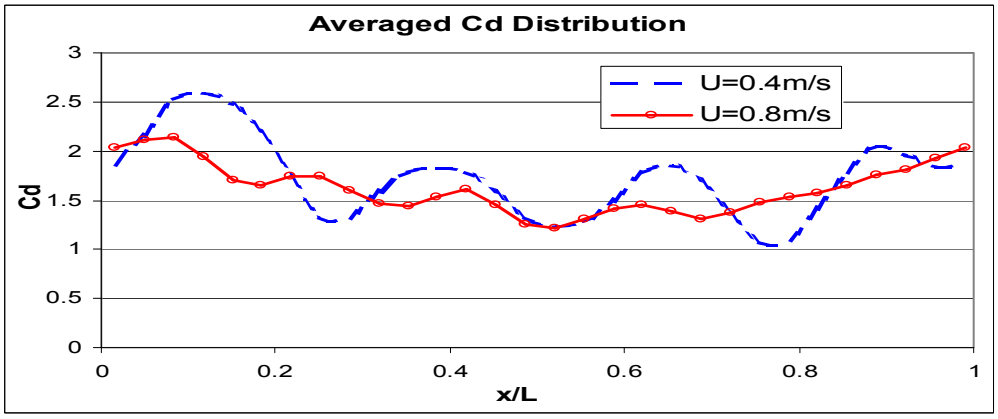

Fig. 72 Mean Drag Coefficients

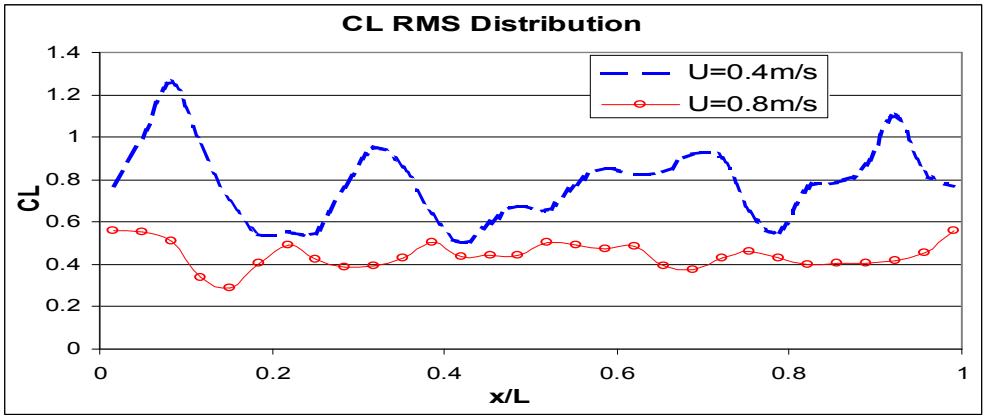

Fig. 73 RMS of Lift Coefficients

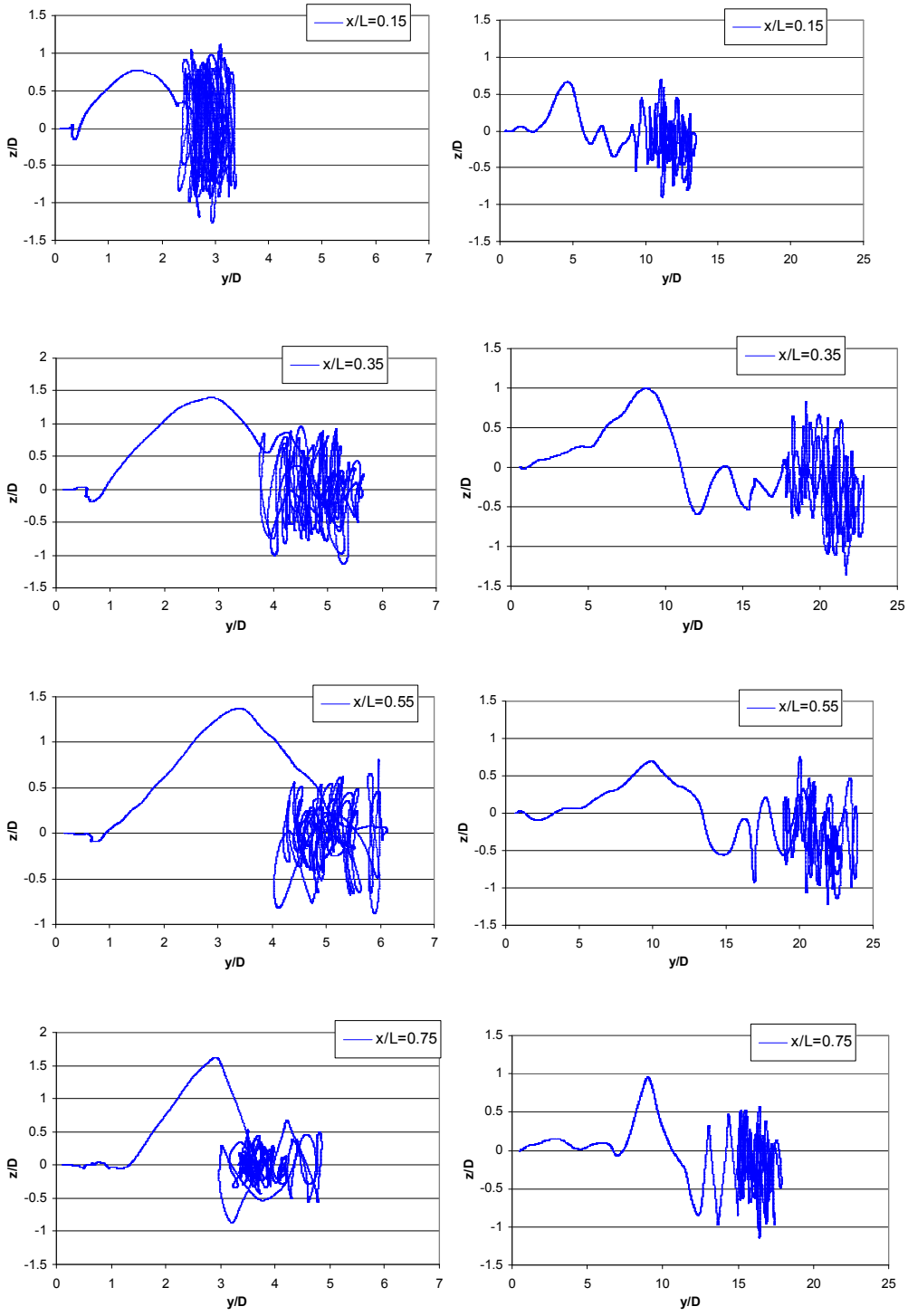

Fig. 74 Riser Motion Trajectory, Left: U=0.4m/s, Right:U=0.8m/s

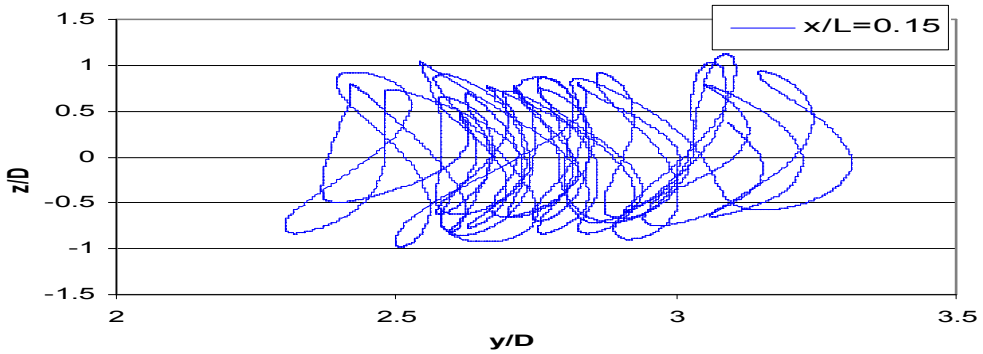

Fig. 75 Riser Motion Trajectory at x/L=0.25, U=0.4m/s

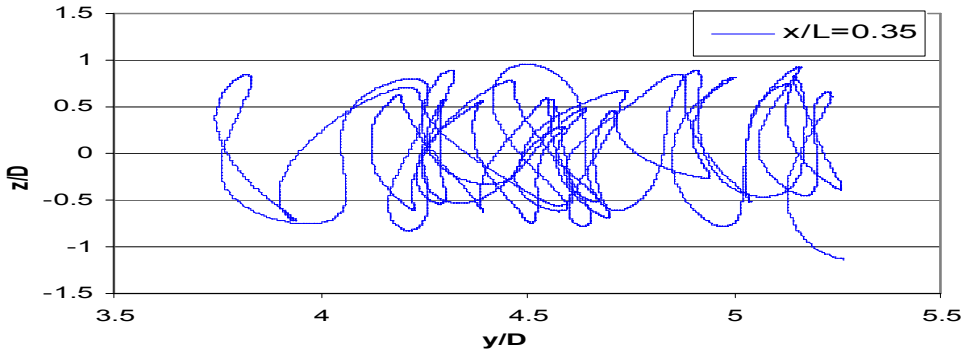

Fig. 76 Riser Motion Trajectory at x/L=0.35, U=0.4m/s

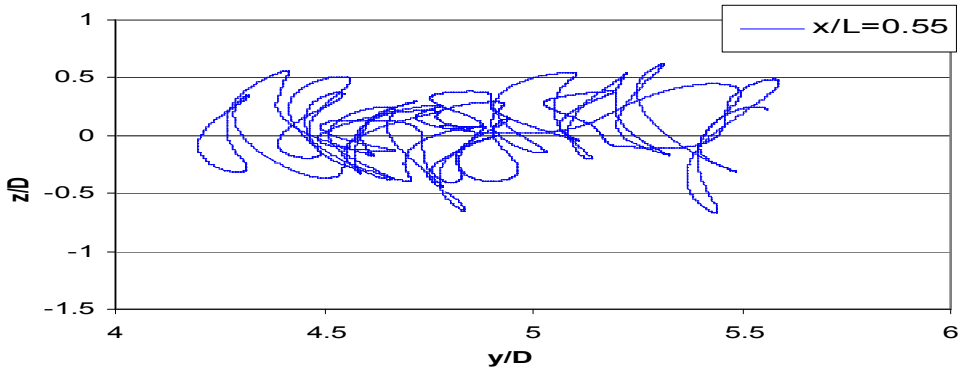

Fig. 77 Riser Motion Trajectory at x/L=0.55, U=0.4m/s

To investigate into more details on the riser VIV, we plotted the riser cross flow motion snap shots in Figs. 78 and 79. It shows the envelope of the dominant mode. The responses are not exactly symmetric. This could be due to the interference from the low-mode riser vibrations in both the in-line and cross flow direction, as we discussed later in this section. We also plotted the riser motion RMS a/D in Figs. 80 to 83, and compared the results to the experimental data (Trim et al. 2005) and published CFD results (Holmes et al. 2006). Generally the comparisons show very good agreement to the experimental data. Some highlights are:

- For cross flow VIV the dominant modes are clear: FANS predicted the 4^{th} mode is dominant for U=0.4 m/s and the 6^{th} mode is dominant for U=0.8 m/s. The model testing shows the 3^{rd} mode is dominant for U=0.4 m/s. One possible reason would be the tension variation. In our calculation the tension within the riser is set to 5 kN, while in the model testing it varies in a range from 4 kN to 6 kN.
- For in-line VIV the dominant modes are not obvious in FANS' results. However, the model testing shows the 5^{th} mode is dominant for U=0.4 m/s. Again this is likely due to the lower order mode dynamics. We suspect that in the model testing the gravity of the riser has played a role in the riser in-line VIV by acting as a restoring force. Further assessment is needed to confirm that.

The maximum cross flow rms a/D is also compared to the experimental data at U=0.4 m/s and 0.8 m/s in Fig. 84. It shows good agreement as well. We noticed that the

locations of the maximum riser response are not at the riser middle section. Some of them are near the two ends of the riser. This could be due to the "pinned" boundary conditions, where all the modes have zero curvature at the two ends, and the peak curvature values of the excited modes are most likely to add together near the ends.

Another interesting phenomenon is that the cross flow VIV is not symmetric along the riser. This is clearly shown in the experimental data: the rms has a trend of going higher at large x/L. We also found the same in our results. Further investigations disclose that the 2nd in-line mode (and higher even order modes) excitation could be the reason. We plotted the in-line motion time histories at x/L=0.25 and 0.75, take the difference between these two motions, and compare that to the 2nd in-line mode amplitude, as shown in Fig. 85. The correlation between these two is obvious. Due to the existence of the even order in-line mode, the riser top and bottom section experience different relative fluid-riser velocities, hence different lift forces.

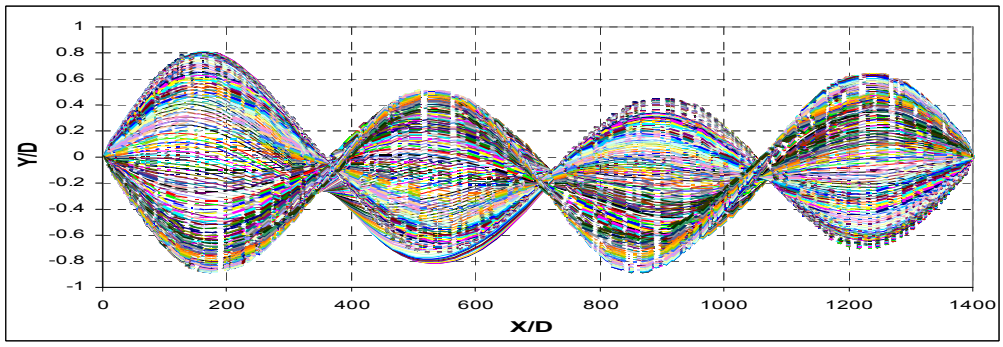

Fig. 78 Riser CF Response Envelope for U=0.4m/s, t=193~200

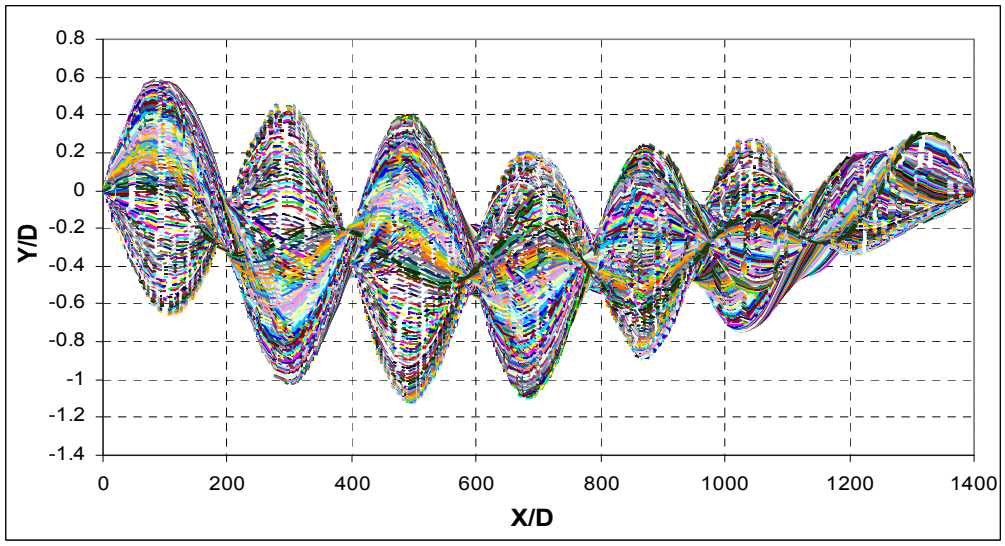

Fig. 79 Riser CF Response Envelope for U=0.8m/s, t=193~200

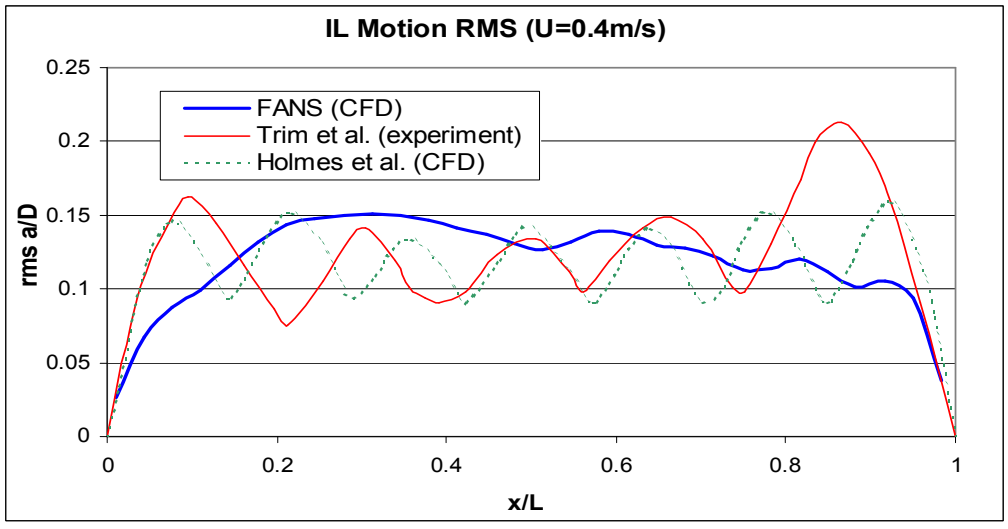

Fig. 80 Riser In Line VIV RMS for U=0.4m/s

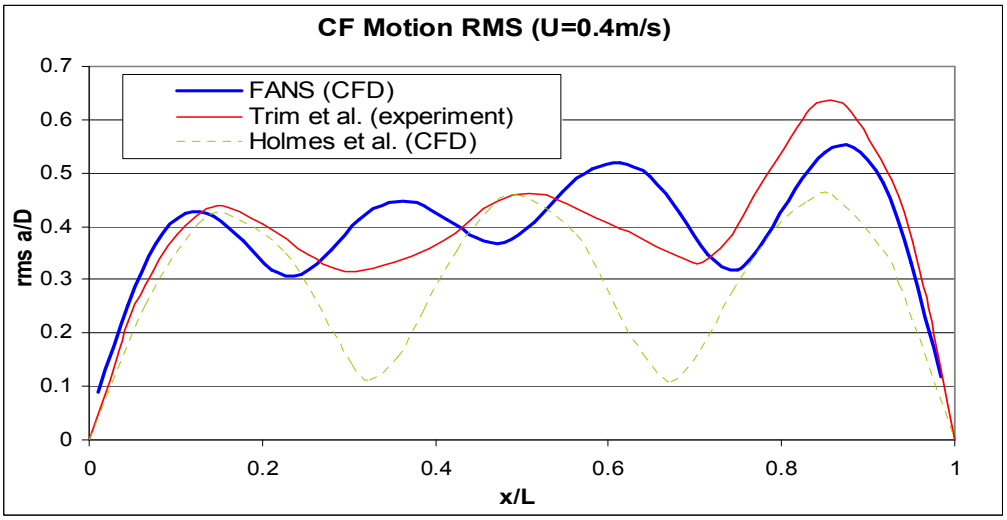

Fig. 81 Riser Cross Flow VIV RMS for U=0.4m/s

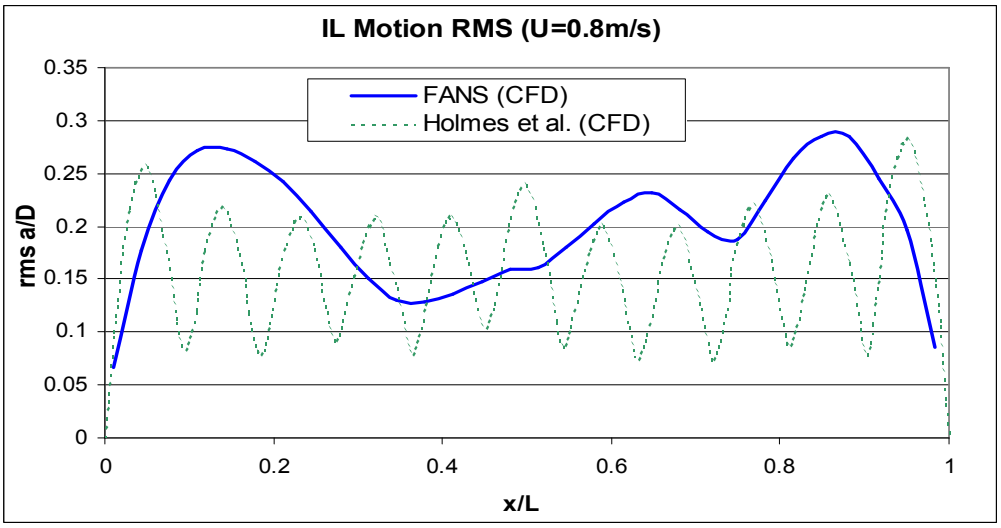

Fig. 82 Riser In Line VIV RMS for U=0.8m/s

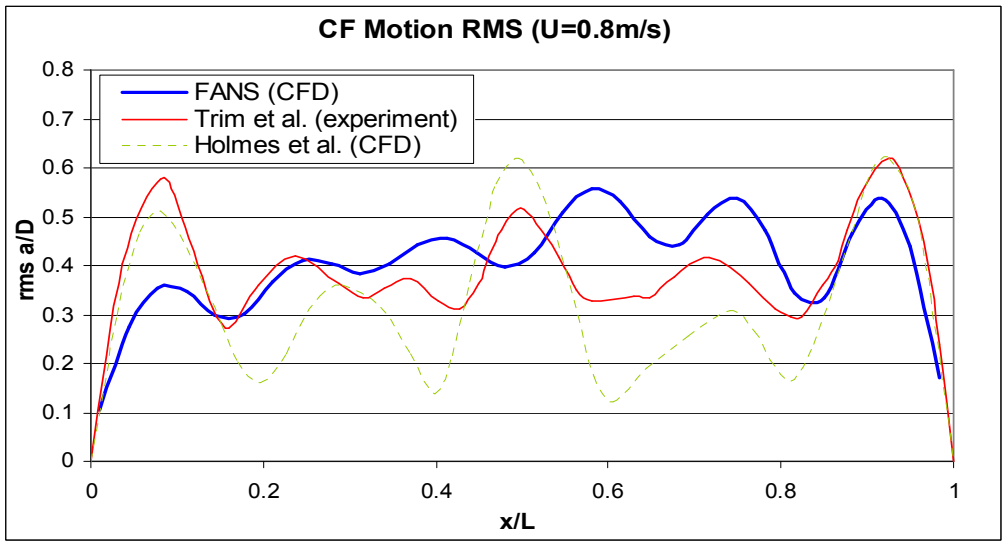

Fig. 83 Riser Cross Flow VIV RMS for U=0.8m/s

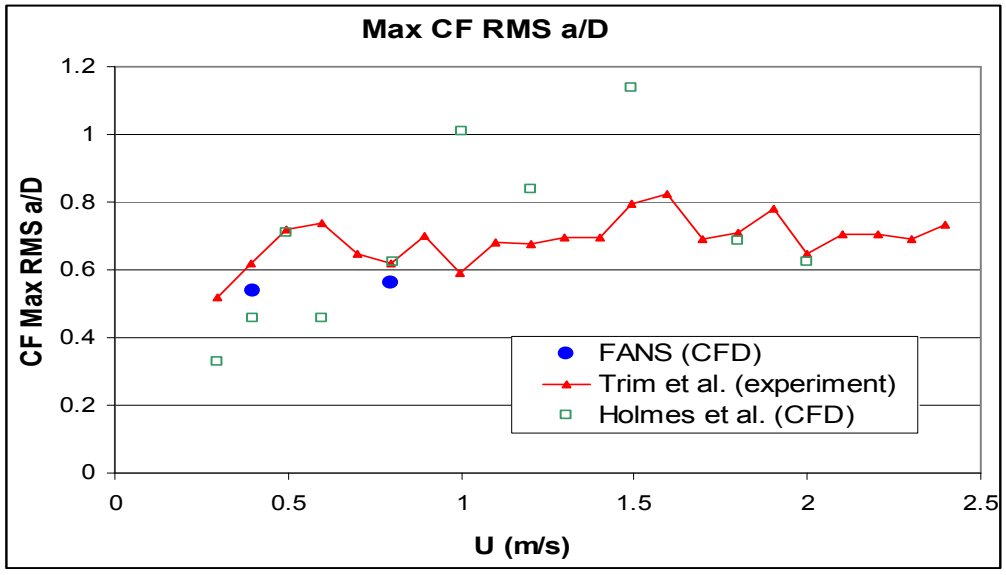

Fig. 84 Riser Cross Flow VIV Max RMS

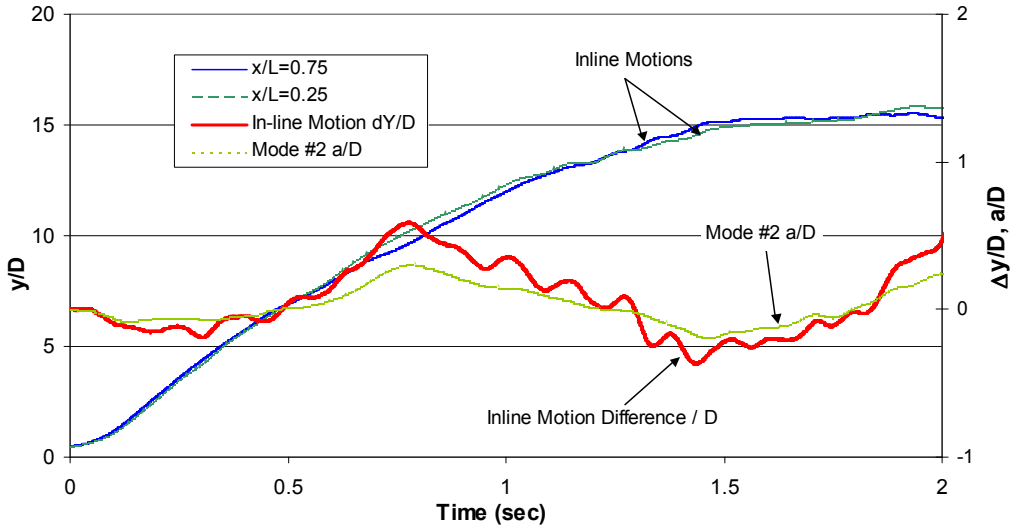

Fig. 85 Riser Motions at x/L=0.25 and 0.75

Discussions

This chapter studied a long riser VIV response by using an unsteady, overset-grid (Chimera), Navier-Stokes method. We presented two case studies with uniform current speed of 0.4 m/s and 0.8 m/s respectively. The total element number used for the computation of fluid domain is less than 1 million. And the results are in good agreement with published experimental data. It is found that when constrained by data grid element number, it is more efficient to focus on accurate prediction of drag and lift forces than the flow details in spanwise direction. Nevertheless, more elements could be used in the riser axial direction to provide better resolution, hence more accurate drag and lift force distributions. For deepwater risers, when current speed is high, very high order modes could be excited. Therefore, the data grid in riser spanwise direction should be adequately fine to predict the high order VIV response with acceptable accuracy.

In this study it also demonstrated that the time domain CFD approach is able to provide more valuable details on the drag force, lift force, fluid velocities and vorticities, riser displacement and modal response time histories. We successfully used FANS to illustrate some of the interesting but not explained phenomena in the experimental data. In conclusion, a CFD approach that could be applied to long marine riser VIV assessment has been presented. And its validity and effectiveness to predict long riser VIV in uniform current have been demonstrated through case studies and comparisons to published experimental data (Huang et al. 2007a, 2007b, 2007c, 2007d).

CHAPTER VII

3D SIMULATION OF FLOW PAST A HORIZONTAL RISER IN SHEAR CURRENT

In Chapter XII we compared the VIV simulation results of a long riser (L/D=1,400) to the experimental data in uniform currents. In this chapter we continue to use the same CFD approach and data grids to study the riser VIV response in shear current. In order to facilitate a direct comparison with the experimental data of Trim et al. (2005), we have chosen two linearly shear current profiles with maximum speeds of 0.4 m/s and 0.8 m/s respectively. During the experiment, the riser was horizontally positioned under the water. One end of the riser was fixed, while the other end was towed in circular movement at constant speed. This would simulate a linearly shear current. The effect on VIV due to the riser circular movement is expected to be small, as discussed in Holmes et al. (2006).

The riser is 38 m in length and 0.027 m in diameter. In the simulations, the drag (C_d) and lift (C_L) coefficients are calculated along the riser at each time step. Then the riser motions are solved by a modal motion solver as if the drag and lift forces are constant. This is an explicit approach without iteration between the flow field and the riser motion. We used the 4^{th} order Runge-Kutta method to integrate the motion equation. The riser was modeled as a beam with a constant tension of 5 kN. Its two ends are assumed to have pinned connections. No damping has been included. It is estimated that the dominant mode should be less than the 10^{th} mode. Therefore, the riser bending

stiffness was expected to have very limited effect on the results, and was neglected in this study. The Reynolds number varies along the riser. It has a maximum value of $1.7x10^5$ at x/L = 1.0 for Umax=0.8 m/s case.

Simulation Results

The riser VIV responses in two linearly shear current profiles are analyzed. These two profiles are illustrated in Fig. 86. We chose these two current profiles to facilitate a direct comparison of the simulation results with the experiment data and other numerical investigations.

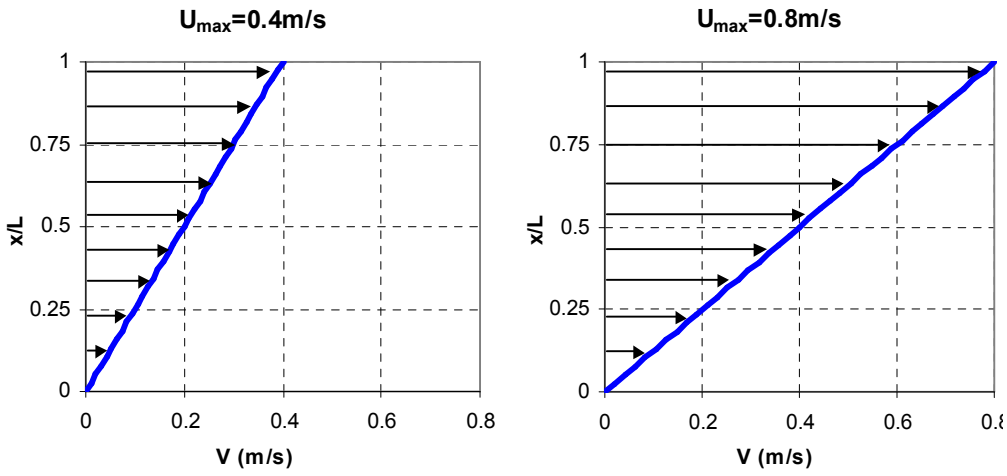

Fig. 86 Linearly Shear Currents

The simulations started with an initially un-deformed riser. The riser begins to move after it is subjected to a shear current, and deflects continuously until its internal restoring force is sufficiently large to overcome the drag forces. Theoretically, this motion is transient and subsides as simulation continues. However, we found that the transient response decays rather slowly over the duration of the present simulations, which made it difficult to distinguish this transient motion from the riser in-line VIV.

The time domain simulations are carried out to a total of 20,000 time steps, or fluid travels a total distance of 200 OD (5.4 m) at x/L=1 for Umax=0.4 m/s case. Fig. 87 shows the evolution of the riser VIV and vortex shedding under different current profiles. The left hand side riser is undergoing VIV in shear current, while the right hand side riser is undergoing VIV in uniform current. Both risers start with un-deformed configuration. After a period (approximately 4,000 time steps) of transient response, both risers reach nearly equilibrium positions. The maximum riser deflection occurs at the middle section for risers in uniform current, while it occurs at a slightly higher position in the shear current. The maximum riser deflection amplitude in the uniform current is approximately four times of that in the shear current. This is reasonable since the averaged speed for the shear current is half of that for the uniform current, and the drag force is proportional to the square of the current speed. Majority of the vortex shedding shows a clear 2S pattern, which is defined in Williamson and Roshko (1988). Coalescence of vortex (C pattern) also exists in both cases. It occurs near the top and bottom regions in the uniform current, and around the middle section in the shear

current. The cross flow VIV amplitudes are moderate and in the order of 1D. No obvious 2T patterns (Williamson and Jauvtis, 2004) have been observed in these two-degree-of-freedom simulations.

Fig. 88 shows two snap shots of the vorticity fields for Umax=0.4 m/s and Umax=0.8 m/s respectively. The riser maximum lateral deflection for Umax=0.8 m/s case is approximately 5~6 times of the riser diameter. As expected, it is much larger than that of the Umax=0.4 m/s case. It is also observed in both cases that the 2S pattern and C pattern are mixed along the riser. The C pattern indicates a possible power out region. Therefore, it is likely that the riser middle section is the power in region, while the riser top and bottom sections are the power out regions (Vandiver and Li, 2003).

Fig. 89 shows the vorticity contours for Umax=0.4m/s and Umax=0.8m/s, respectively, at selected time instants. For Umax=0.8m/s case, the dominant modal shape number (7^{th} mode) is much higher than that (3^{rd} mode) of the Umax=0.4 m/s case.

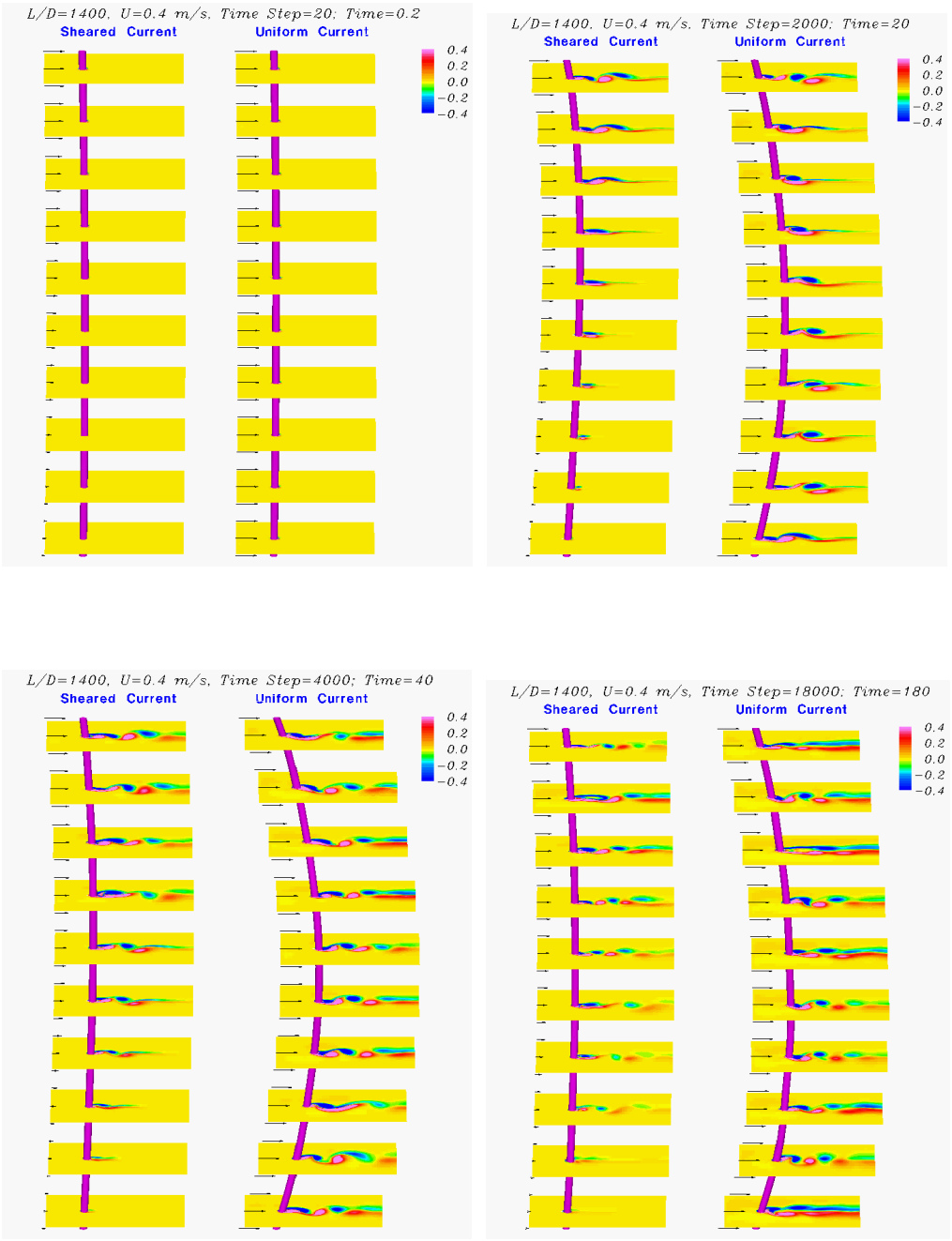

Fig. 87 Vortex Shedding, Umax=0.4m/s, Left: Shear, Right: Uniform

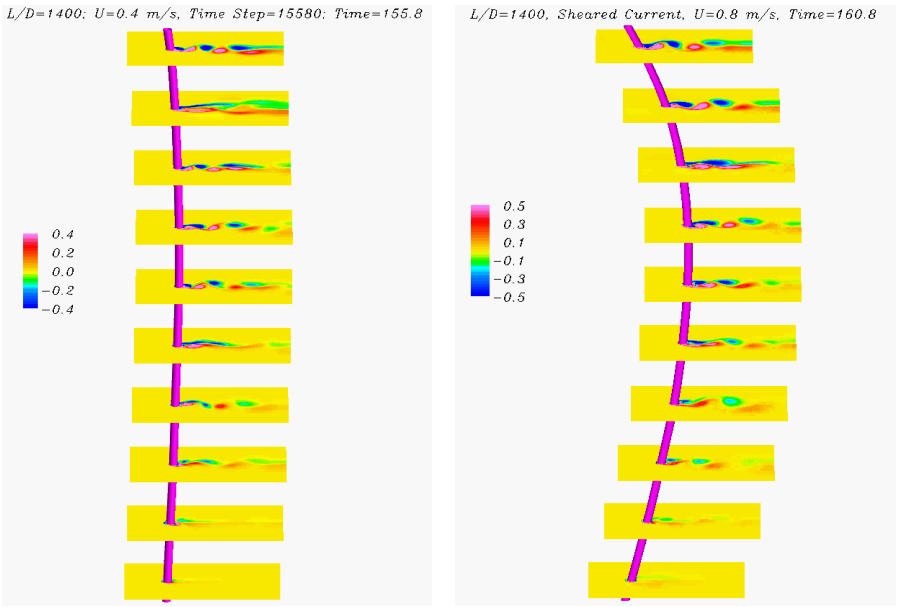

Fig. 88 Riser VIV Snap Shots, Left: Umax=0.4m/s, Right: Umax=0.8m/s

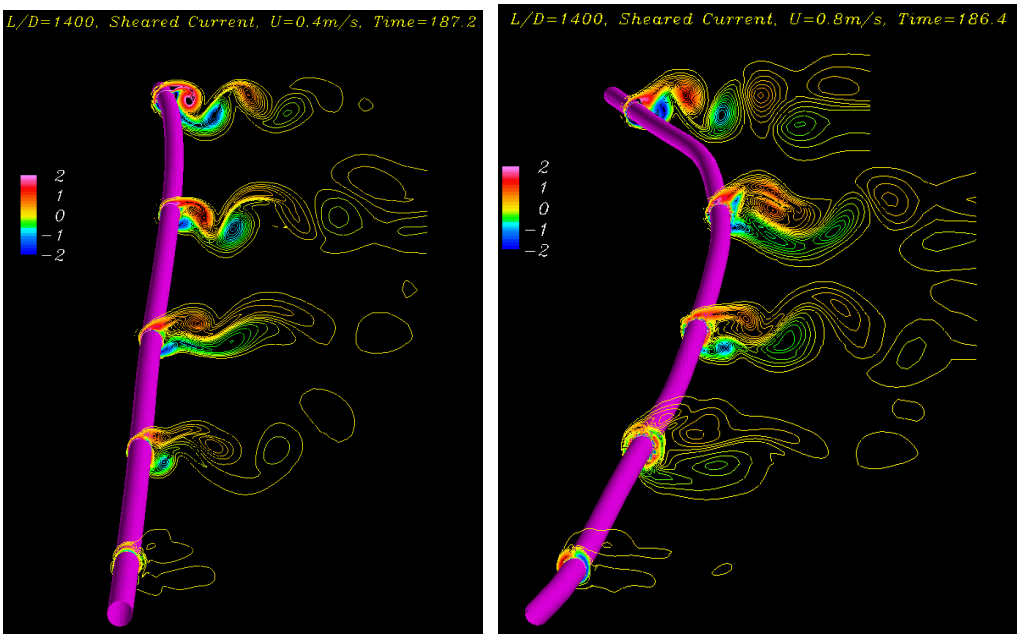

Fig. 89 Vorticity Contours, Left: Umax=0.4m/s, Right: Umax=0.8m/s

The drag and lift coefficients are calculated at each time step. Figs. 90 to 93 show the comparisons between the uniform and the shear current cases. It shows that the drag coefficients are in the similar ranges for all cases, with minor variations due to different dominant modes. While the lift coefficients for shear current are generally lower than those for the uniform current. This could be related to the riser vibration mode dominant level and amplitudes in these two current profiles. It is not surprising to see that the single mode dominant is more likely to occur in uniform current than in shear current, and with higher a/D rms values. The lift coefficients also show variations along the riser that corresponds to the dominant mode shapes. The higher the current speed, the higher the dominant mode number becomes. Hence more peaks and troughs are observed in the lift coefficients for U = 0.8 m/s case. The results also show that the lift coefficients have a rms value of 0.2~0.4 in shear current profiles. The averaged values for shear current cases are 0.34 for Umax = 0.4 m/s, and 0.32 for Umax = 0.8 m/s. On the other hand, the averaged rms values are 0.78 for U=0.4 m/s and 0.44 for U=0.8 m/s in the uniform current cases. Although the exact values are case dependent, it seems that the lift coefficients are less sensitive to the current speed under shear current condition. The drag coefficients are slightly higher at the riser top and bottom regions in uniform current cases. One possible reason could be due to the vortex shedding pattern near the top and bottom boundaries (C pattern). Note that the mean drag coefficient is related to several factors, including Reynolds number, riser vibrating amplitudes and frequencies. Therefore, high velocity does not necessarily result in high drag coefficient, as shown in the shear current cases.

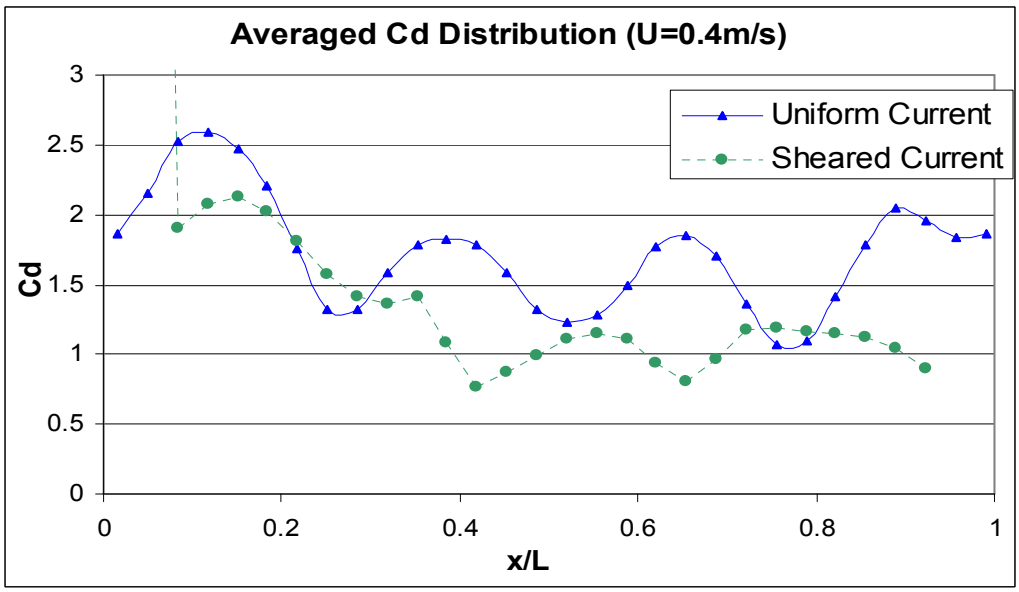

Fig. 90 Drag Coefficient Distribution, Umax=0.4m/s

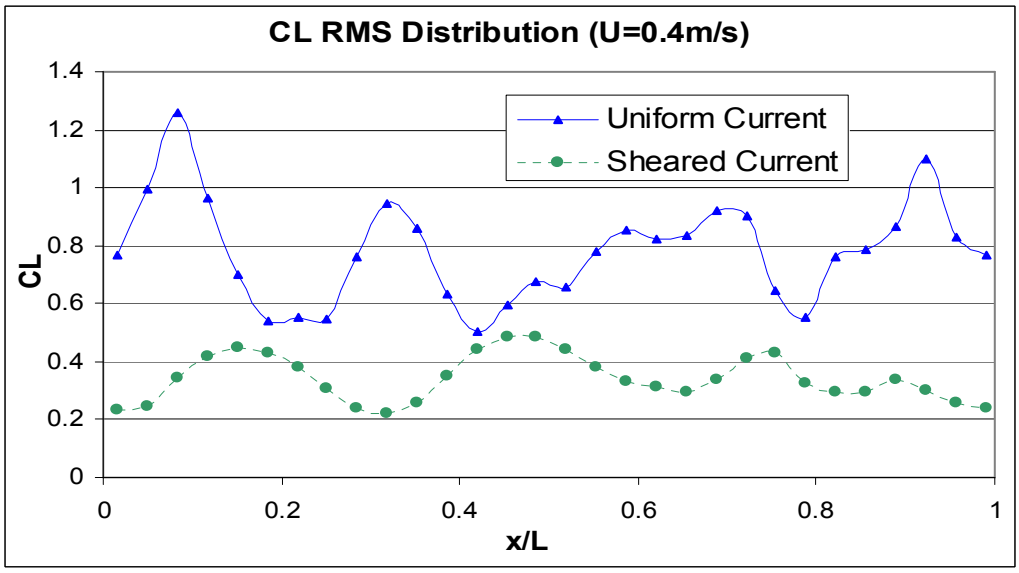

Fig. 91 Lift Coefficient Distribution, Umax=0.4m/s

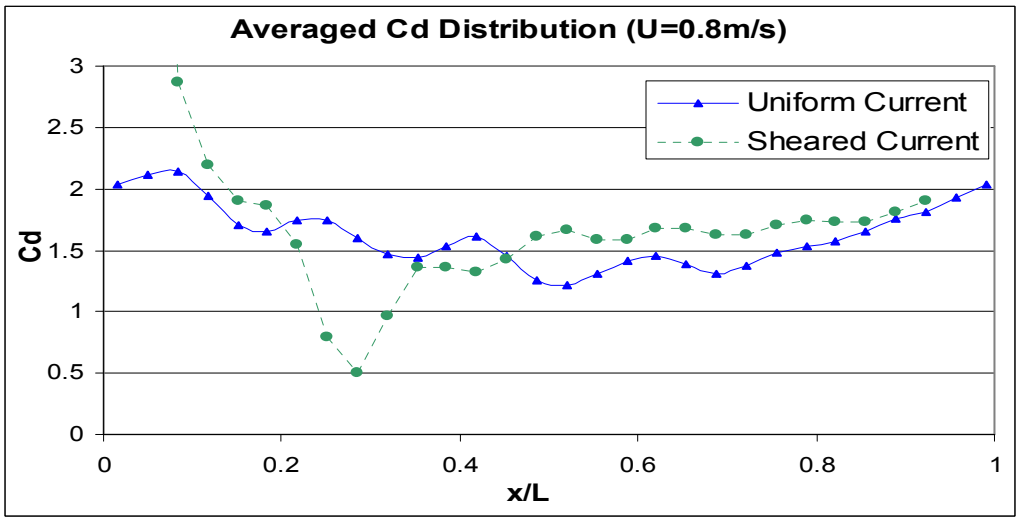

Fig. 92 Drag Coefficient Distribution, Umax=0.8m/s

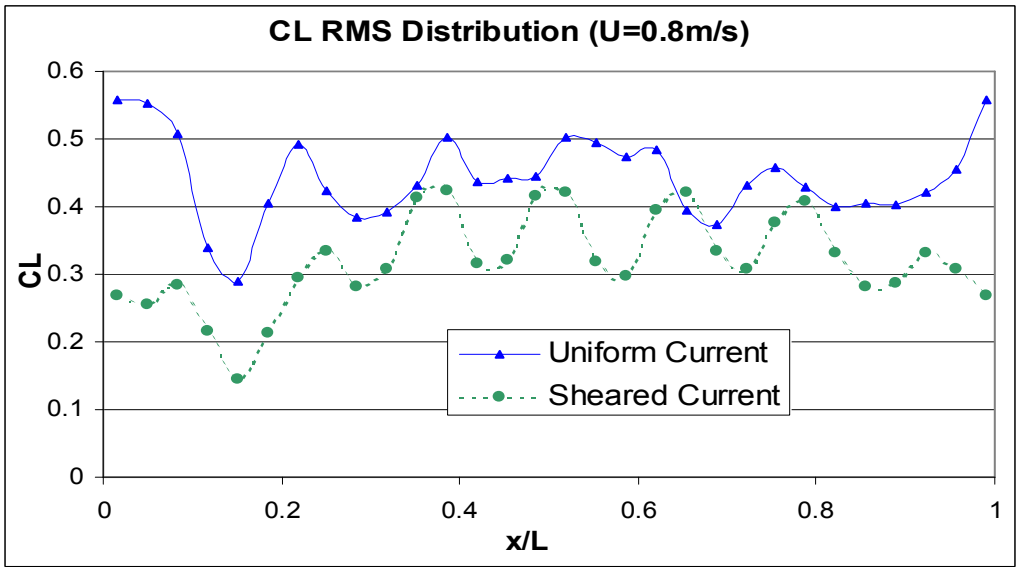

Fig. 93 Lift Coefficient Distribution, Umax=0.8m/s

The riser response rms a/D is of particular interest in the riser VIV simulations. Figs. 94 and 96 show the comparison between the simulation results and experiment data in cross flow VIV. The experimental data are plotted in straight lines since only the mean and maximum values are given in the experiment of Trim et al. (2005). Our CFD simulation results predicted similar maximum and mean values as the experiment data for the slower shear current case (Umax=0.4 m/s), while under-predicted the VIV in higher shear current case (Umax=0.8 m/s). Fig. 96 shows the comparison of maximum rms a/D. In general the CFD approach tends to underestimate the riser VIV peak response. The in-line riser VIV rms a/D is not presented since it is dominated by the transient motions as noted in earlier discussions. Hence, it is difficult to distinguish the in-line VIV from the overall dynamic motions.

For completeness, the riser motion trajectories for both the shear and uniform currents are also shown in Figs. 97 and 98 for Umax = 0.4 m/s and 0.8 m/s cases, respectively. The figure "8" pattern is clearly shown only when the in-line motion is small, and the dominant mode number is low, i.e. x/L=0.15 and Umax=0.4 m/s. Otherwise, the riser movement does not necessarily take any simple shapes.

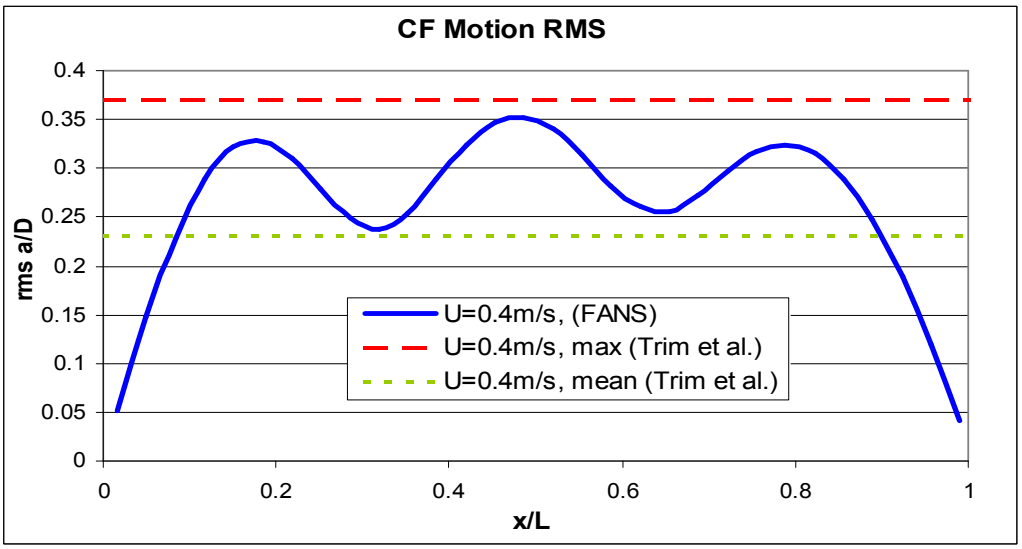

Fig. 94 Cross Flow VIV RMS a/D, Umax=0.4m/s

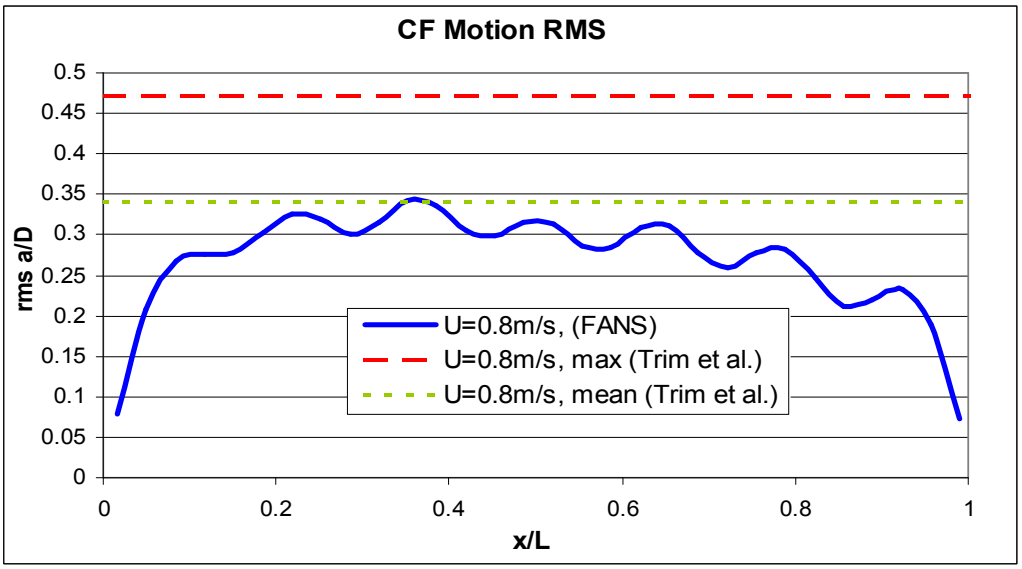

Fig. 95 Cross Flow VIV RMS a/D, Umax=0.8m/s

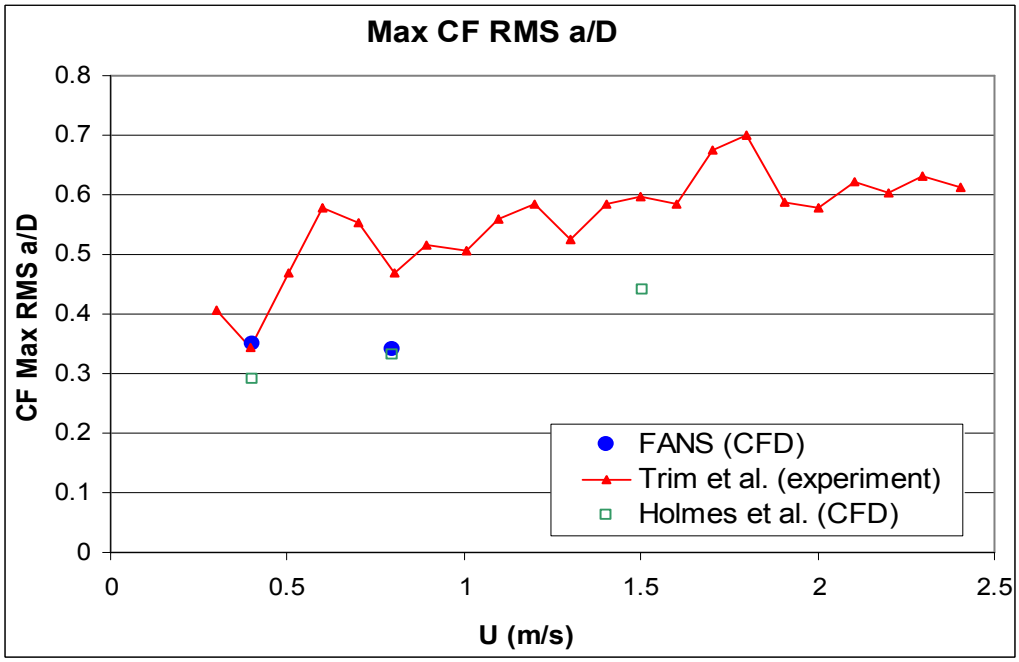

Fig. 96 Cross Flow VIV Max RMS a/D

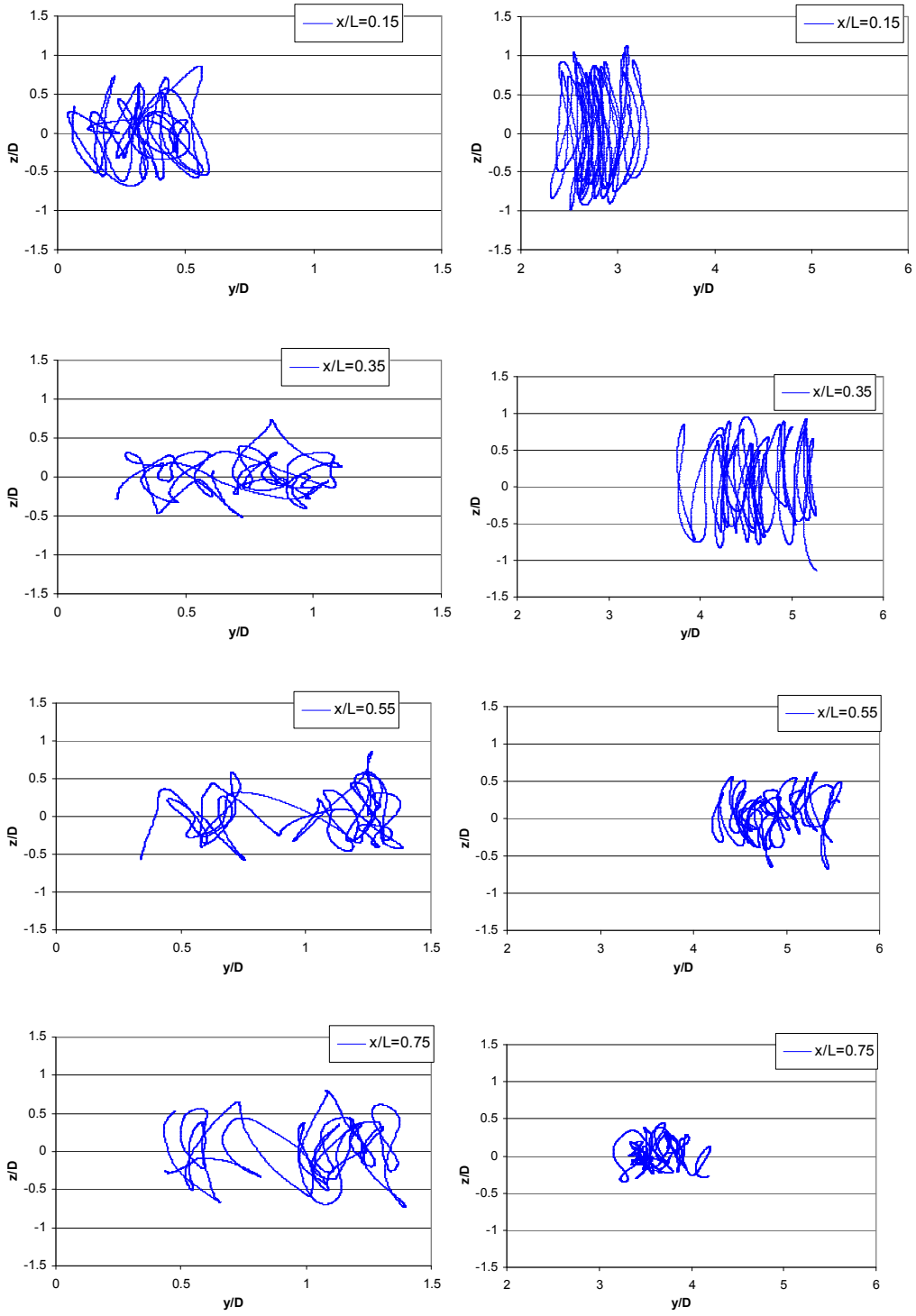

Fig. 97 Riser Motion Trajectory, Umax=0.4m/s, Left: Shear, Right: Uniform

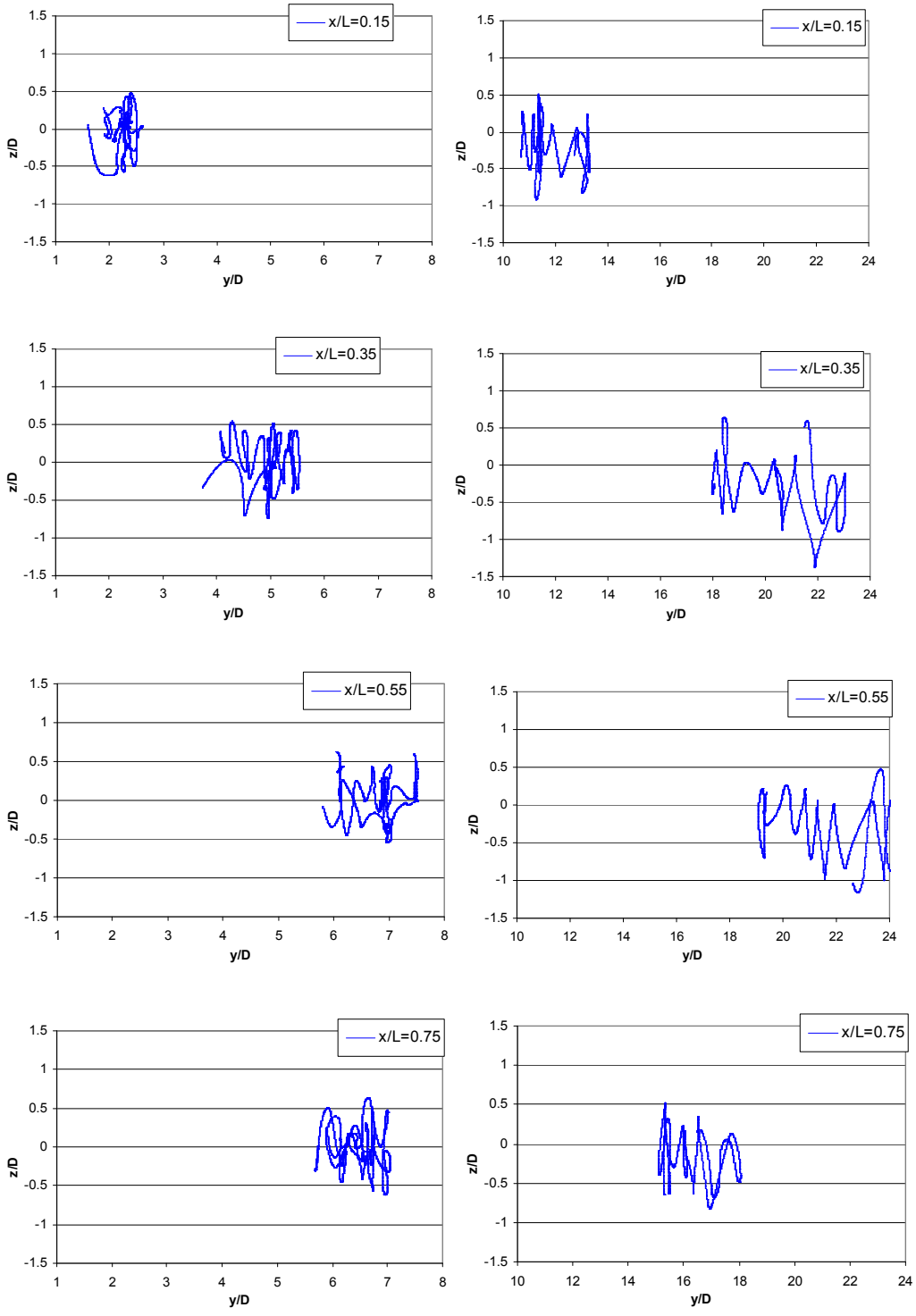

Fig. 98 Riser Motion Trajectory, Umax=0.8m/s, Left: Shear, Right: Uniform

The riser in-line and cross flow motion responses are calculated through modal superposition. The rms a/D of each modal component are plotted in Figs. 99 and 100 for in-line and cross flow respectively. The response includes both the riser transient dynamic motions due to its initial positions and velocities, and the steady VIV. The transient response is usually low frequency and low modes, as shown in Fig. 99. We didn't attempt to split the transient response and steady VIV in this section. Further investigation is needed in order to separate the transient response from the steady VIV.

In order to measure the dominant level of an excited modal shape, we normalized the modal energy by the total response energy. In other words, we looked at the modal energy percentage of each mode. Fig. 101 shows the results for in-line motions, which is dominated by the 1st mode. As discussed earlier, this 1st mode is mainly due to the transient effect. Fig. 102 shows the modal energy percentages of cross flow motions. For each studied case, there is a single mode that contributes at least 40% of the total vibrating energy. This single mode is the dominant mode that is of particular concern for VIV-induced fatigue. However, we also see a number of non-dominant modes with each of them contribute 10% to 20% of the total energy. The importance of these non-dominant modes and their impact on the riser VIV and VIV-induced fatigue remain to be determined.

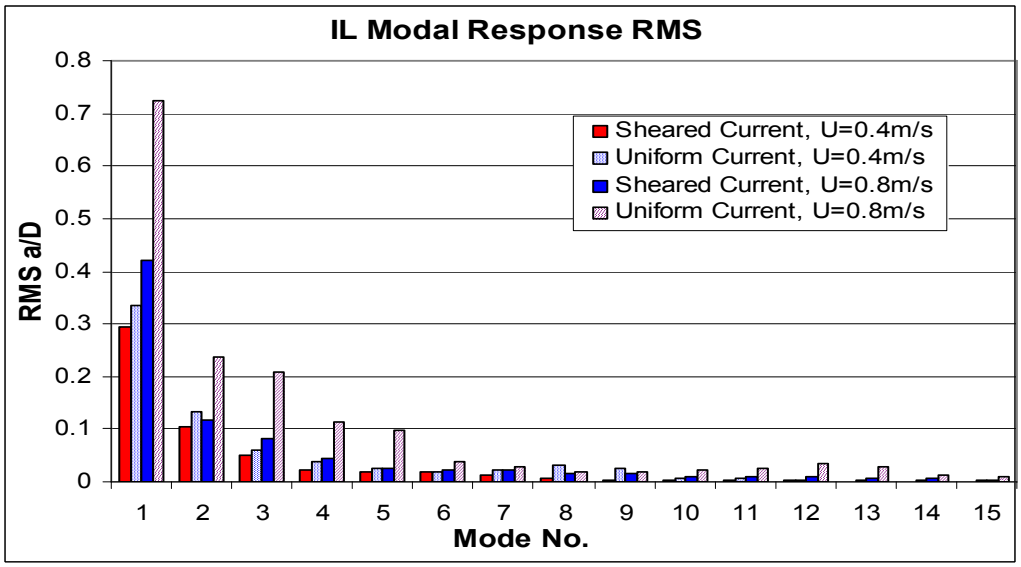

Fig. 99 In-Line VIV Modal Response Amplitude

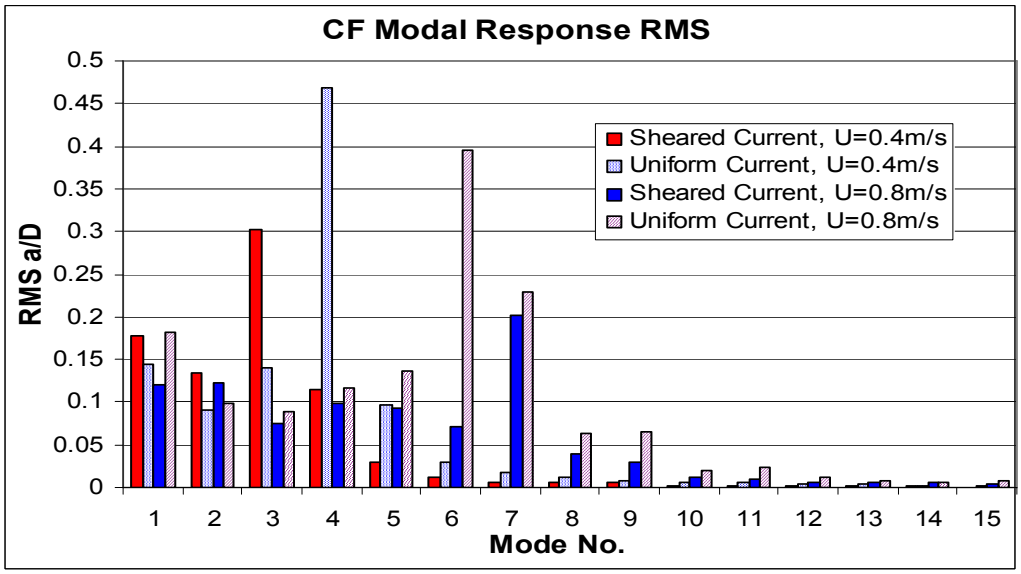

Fig. 100 Cross Flow VIV Modal Response Amplitude

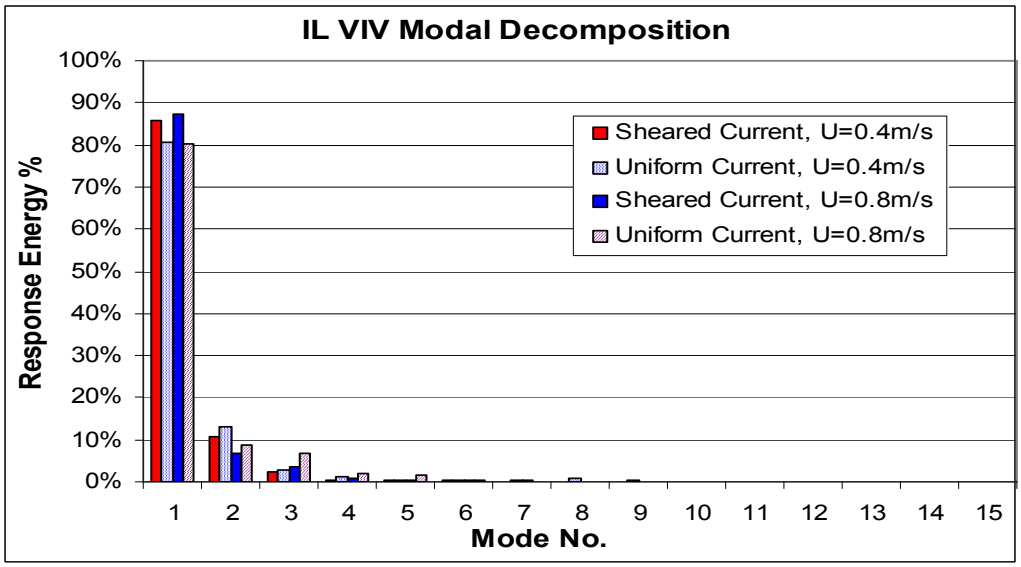

Fig. 101 In-Line VIV Modal Response Energy

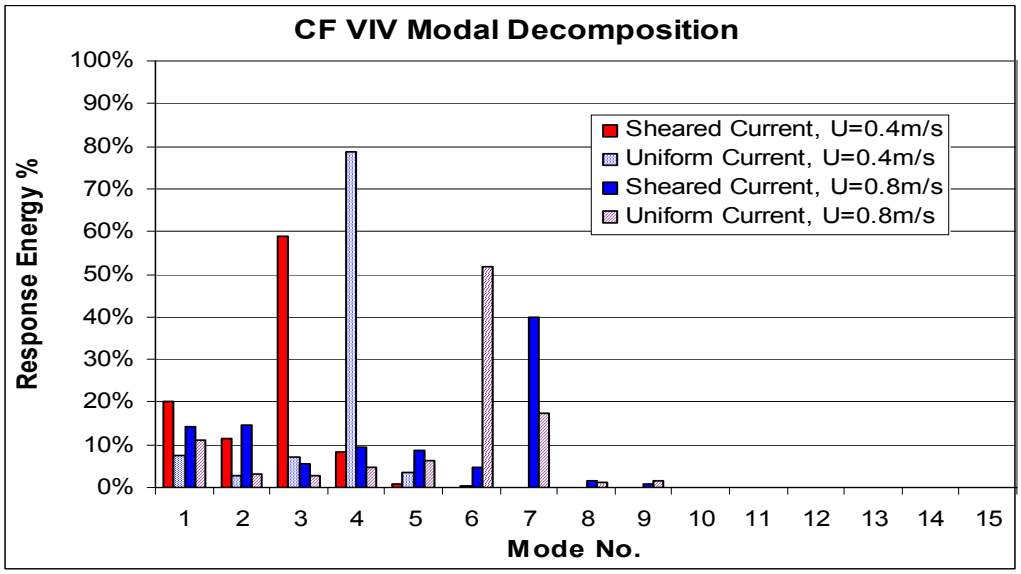

Fig. 102 Cross Flow VIV Modal Response Energy

Discussions

In this chapter we presented two case studies with shear current speed of 0.4 m/s and 0.8 m/s at x/L=1.0. The results are within the ranges of published experiment data. It indicates that the FANS code is capable of predicting reasonable results for long risers using fairly coarse grid in the riser axial direction. It is worthwhile to note that FANS can be readily generalized to handle much more complex current conditions, such as highly shear current and submerged current. Some findings of the study are:

1. The vortex shedding pattern in the shear current is different from that of the uniform current. In the uniform current case, the riser motion and vortex shedding are usually synchronized. In the shear current case, the 2S and C patterns may correspond to the power-in and power-out zones along the riser.
2. Mode lock-in could occur in the shear current. However, its dominant level (in terms of the energy percentage) is lower than that of the uniform current.
3. A long marine riser could have large mean lateral deflection when subject to strong current. It seems that this mean lateral deflection is more than a static value that could be subtracted during the riser VIV simulations. It is part of the result from the fluid-structure interaction. Hence it could influence the in-line and cross flow VIV by altering the flow field.

In conclusion, we used a CFD approach to simulate a long marine riser VIV response in shear current. The simulation details are presented, analyzed, and validated against the experiment data (Huang et al. 2007a, 2007b, 2007c, 2007d).

CHAPTER VIII

3D SIMULATION OF FLOW PAST A 3000FT RISER IN UNIFORM CURRENT

This chapter studied the VIV of a hypothetical single casing top tensioned riser sized for 3,000ft water depth (L/D=3,350). The riser dynamic response under different currents is simulated in 3D. The riser-fluid interaction effect is included through instantaneous drag and lift forces. The riser inline and cross flow responses, including A/D, modal shapes and frequencies, and VIV induced stresses, are studied in detail as well.

The fluid domain around the riser is meshed with structure data grids, which consist of a phantom background grid, a wake grid, and a riser body grid. It is estimated that the highest mode could be excited in a 0.4 m/s current (slightly less than 1 knot) is the 12^{th} mode. In order to represent this mode, we used 30 data grids in the riser span direction, which is a minimum. The total element number is kept below 1 million, so the computation can be performed on a single processor PC. More data grids would certainly improve the riser simulation accuracy, at the expense of computational speed and resources. During the simulation the wake grid and body grid move together with the riser.

The non-dimensional time step used in the simulation is 0.01, which means the free stream fluid travels a distance of one riser diameter in 100 time steps. This time step

is typical for similar riser VIV problems, and is sufficiently small for stable time domain simulations.

The studied riser is a 10 ¾" single casing top tensioned riser designed for 3,000 ft water depth. It has a nominal top tension of 400 kips, submerged weight 121 lb/ft, and mass ratio of 4.0. The riser string consists of steel bare joints without external insulations and strakes. For simplicity, specialty joints, such as stress joint and tension joint, are assumed to have the same sectional properties with standard joint. The riser top and bottom boundary conditions are also simplified as pin connection.

The riser has a fundamental frequency of 38 seconds in seawater. Preliminary reduced velocity (Blevins, 1990) screening shows the dominant mode is likely to have a frequency between 8^{th} and 12^{th} mode. The riser modal shapes have been calculated up to the 40^{th} mode to cover any high mode vibrations. The selected modal shapes are shown in Fig. 103. Note that the modal shapes are normalized to unit maximum amplitude, which is usually located near the riser bottom. For deepwater risers, the effective tension near the subsea wellheads is minimum, while it increases to its maximum at the top. Therefore, the peak values of its modal shapes are not constant along the riser. Lower effective tension results in higher vibrating amplitudes. This causes an interesting observation: in deepwater applications, the current profiles usually have their maximum speed near ocean surface, however, the worst riser VIV response is well beyond that region, and it occurs near the bottom, where the current speed is nearly zero, or no current at all. It is also worthwhile to note that a typical production riser has slightly more complicated top and bottom boundary conditions than pinned connection: the

bottom stress joint/tieback connector is nearly rigid, the riser top section is constrained by the floater, and possibly other lateral constrains from a keel joint. While all these details could also be modeled in the proposed CFD approach, we start with the pinned connection case for illustration purpose. After all, when riser is as long as 3,000 ft, the boundary conditions are less likely to have significant impact on the riser global dynamic response.

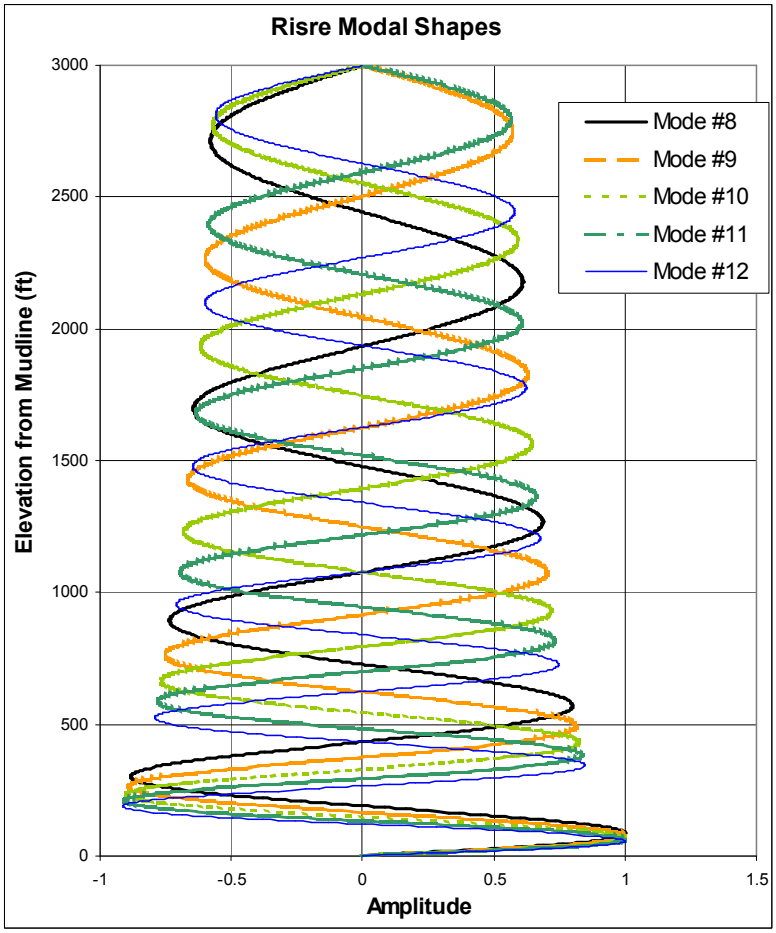

Fig. 103 Riser Modal Shapes

Simulation Results

The simulations have been performed for 20,000 time steps, which correspond to a period of 140 seconds. Fig. 104 shows the evolution of the riser dynamic motion. The risers are initially straight and have no external force except gravity. At t=0s, the risers are subject to a uniform or shear current. They deflect to a new equilibrium position and vibrate back and forth. The in line motions are dominated by transient dynamics. It is not that straightforward to filter out the in-line transient motions. That is also one reason we mainly focused the study on cross flow VIV. Another reason is that the expected dominant mode for in-line VIV is very high (twice of the dominant mode in cross flow VIV), and it is beyond the riser axial resolution of the data grid we used. Being said that, the in-line transient motion could also be important to riser VIV in a sense that: (1) it could influence the riser VIV through disturbing the flow field and changing the initial conditions for vortex shedding, and (2) in the physical world the current condition changes continuously. In other words, the transient response would always exist in real world and might also deserve some attention as well. Some observations from the snapshots are:

At startup phase, the vortices develop slower in the riser middle section than the regions near the ends. Since the riser is fixed at its two ends, the relative velocity is close to the incoming current velocity, and vortices are able to develop and shed when flowing around fixed cylinders. While in the riser middle section, the riser segment has no lateral constrain during the initial period and moves downstream with the current, which results

in small relative velocity. As a result, the drag coefficients near the riser ends are larger than that in the middle section.

In shear current, the riser top section is subject to higher current speed than the lower section. Its initial deflection corresponds to the current profile, i.e. larger riser deflection at higher speed region. However, as the riser deflects more, its own characteristics take effect as well. The riser has much higher effective tension at the top section than in the bottom section. From the riser motion equation we know that the higher the tension, the stiffer the riser would be in lateral direction. Therefore, even the riser lower section is subject to lower current speed, it has much more lateral flexibility, hence has more excursion.

The vortex shedding in the wake of the riser exhibits different patterns at different time. Initially 2S pattern is clearly seen along the whole riser. When the riser reaches near its maximum deflection, coalescence of vortex (C pattern) occurs at top and bottom regions. In shear current case, C pattern occurs only at the top region where the current speed is the maximum. The vortex shedding maintains 2S pattern below a transitional section from C pattern to 2S pattern. In the uniform current case, we found that the C pattern could continue propagating into the middle section of the riser, until it covers the whole riser. Due to the reduced drag force on the riser, the riser reduces its lateral deflections dramatically, as indicated by the arrow in the figure. After that the 2S pattern recovers in the middle section and pushes the riser back toward its equilibrium position. Figs. 105 and 106 show the vorticity contour snapshots where the vortex pattern could be clearly identified.

Overall, the riser exhibits strong flexibility. The cross flow VIV amplitudes are also shown in Figs. 105 and 106 for shear and uniform current respectively. As expected, the shear current causes much less drag force, hence lateral excursion on the riser than the uniform current. The figures also show that the riser lateral deflection is coupled with the vortex shedding, and it could introduce complicated dynamic cross flow response, even in a simple uniform current.

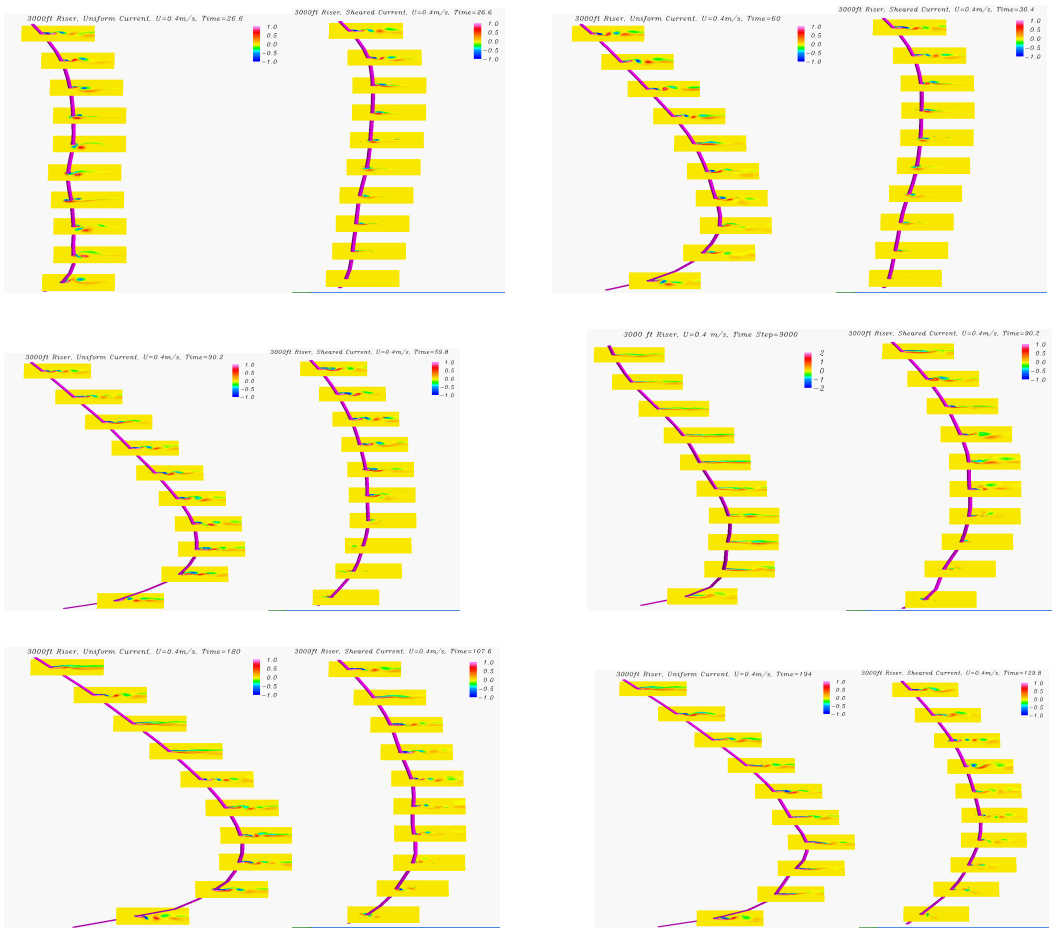

Fig. 104 Riser VIV Comparison, Umax=0.4m/s, Left:Uniform, Right:Shear

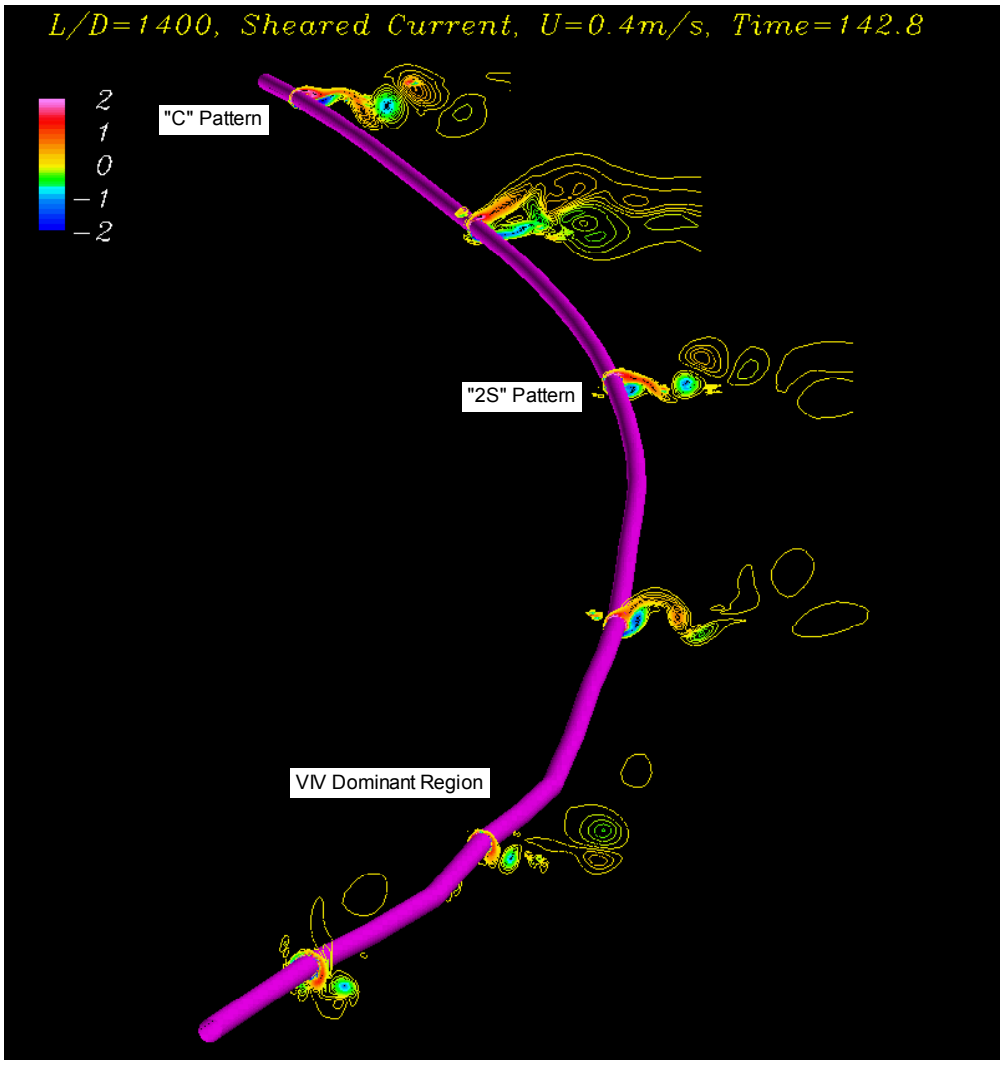

Fig. 105 Riser VIV Snapshot, Shear Current

Fig. 106 Riser VIV Snapshot, Uniform Current

The cross flow modal responses are plotted as shown in Fig. 107. The modal response below 7th mode and above 12th mode has been filtered out during the post-processing for clarity. It shows the dominant mode for the shear current is the 9th mode, while both the 11th and 12th modes have significant contribution to the VIV response for uniform current case. We compared the rms a/D to the results from Shear 7 in Figs. 108 and 109 for uniform current and shear current respectively. It shows the results are comparable for shear current, while FANS predicts lower response in uniform current. This is clearly related to the number of dominant modes. It is worthwhile to point out that other CFD simulations (Willden and Graham, 2004) also showed that the VIV in uniform current is multi-modal, i.e. several modes with similar frequencies are excited at

the same time through added mass adjustment. Note that we have simplified the riser motion equation and neglected the modal damping and stiffness coupling terms. It is unclear that inclusion of these terms would help or impede the multi-mode VIV. Further evaluation is required to address this issue. Overall, FANS code predicted reasonably well results.

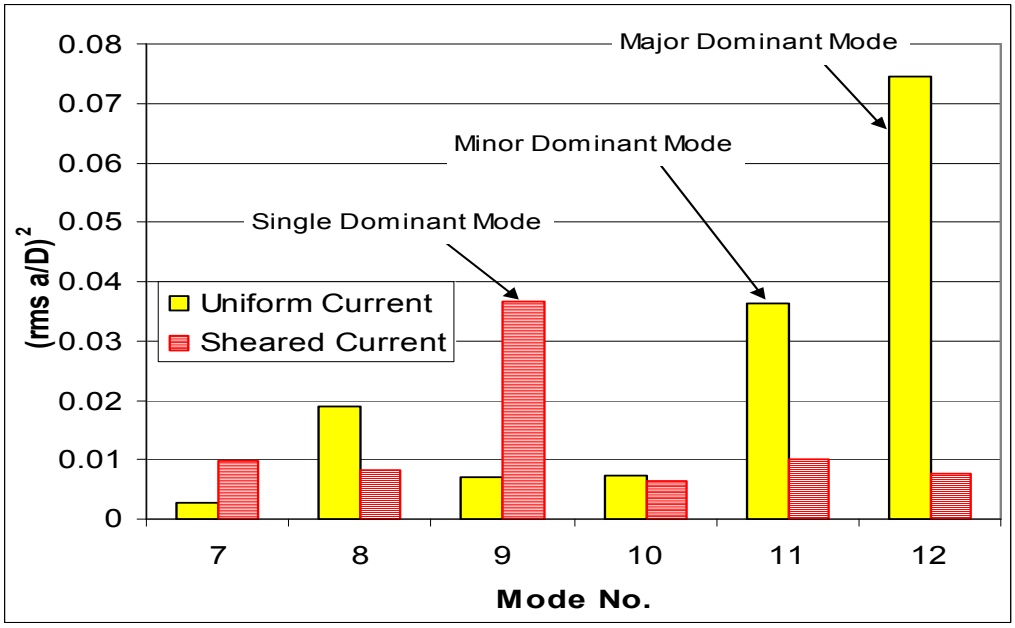

Fig. 107 Riser Cross Flow VIV Modal Response

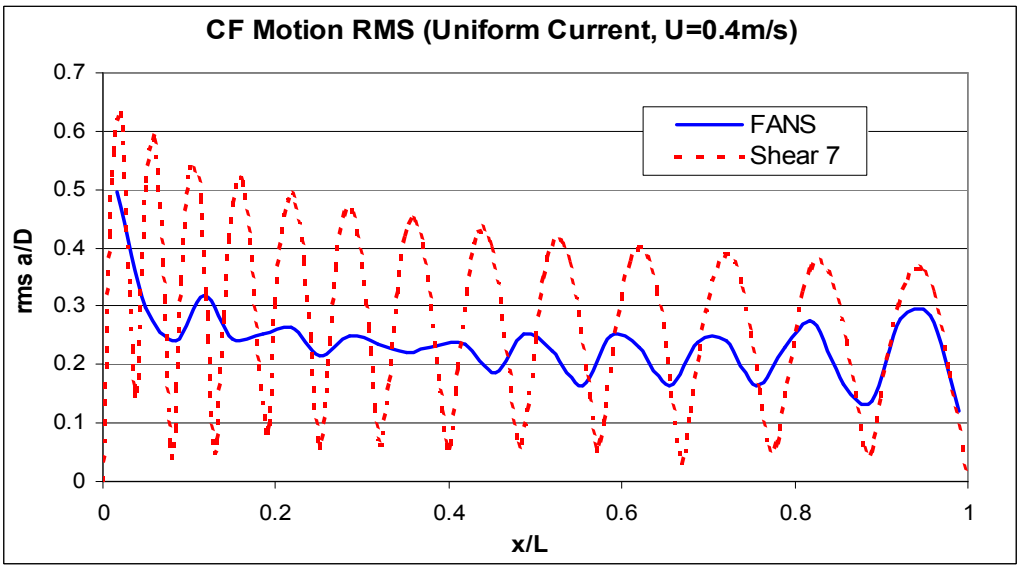

Fig. 108 Riser Cross Flow VIV rms a/D - Uniform Current

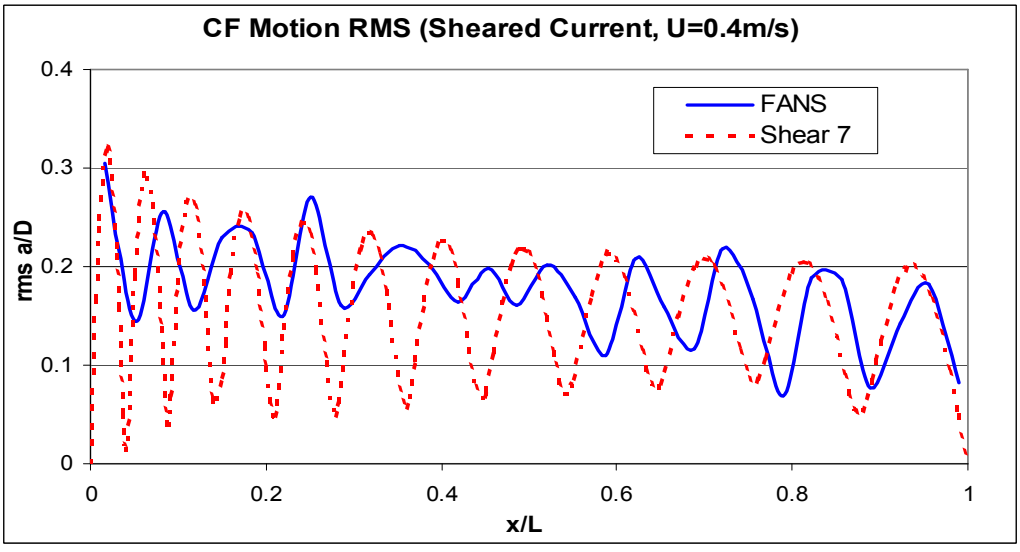

Fig. 109 Riser Cross Flow VIV rms a/D - Shear Current

The stress rms for the uniform and shear currents are presented and compared to Shear 7 in Figs. 110 and 111 respectively. The comparisons are in general agreement. It shows in both cases that the worst stress is always near the riser lower end. This is due to the lower effective tension at the riser bottom portion. This is interesting since in shear current, the current has high speed at the top, while the VIV-induced fatigue damage at this location is minimum. In contrast, there is no current near the bottom, while the fatigue damage at this region is the worst.

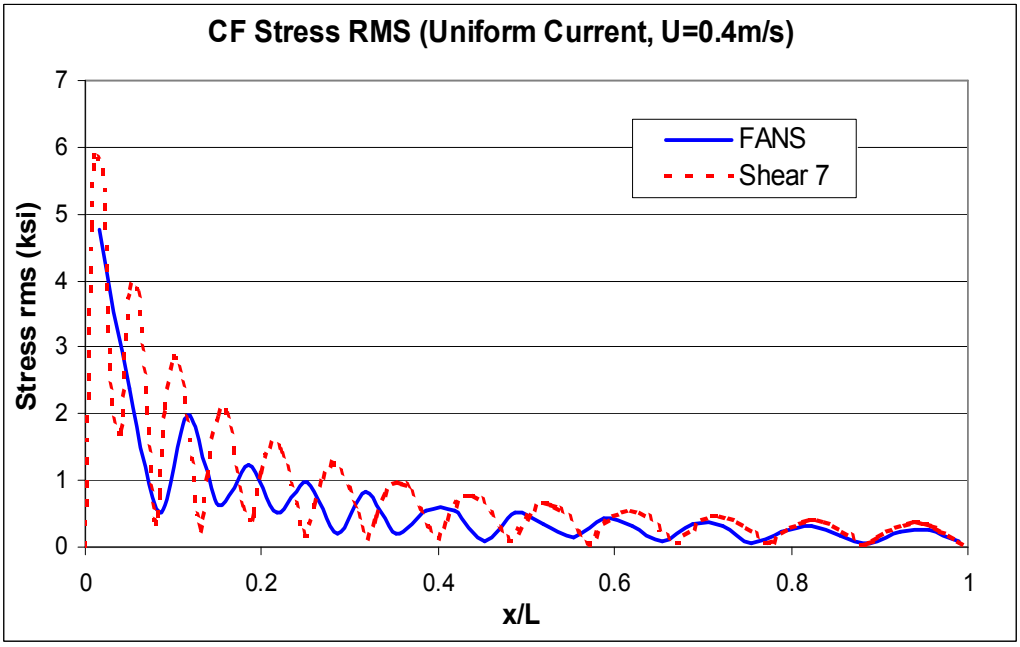

Fig. 110 Riser Cross Flow VIV Induced Stress – Uniform Current

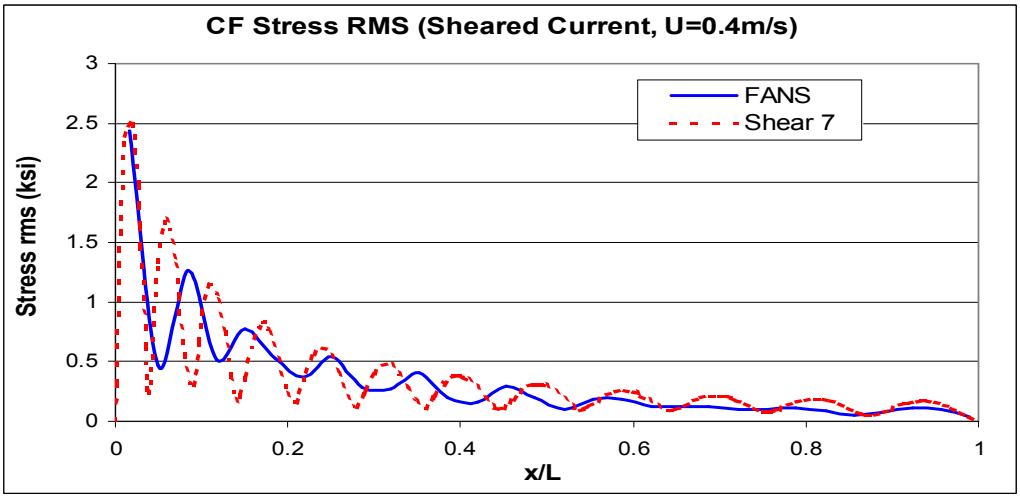

Fig. 111 Riser Cross Flow VIV Induced Stress – Shear Current

Discussions

In this chapter we have studied a 3,000ft riser VIV under both uniform and shear current conditions. The fluid-riser interactions are simulated in time domain. The riser 3D motion and vortex shedding pattern are examined in detail. We also calculated the cross flow VIV amplitudes and stress rms along the riser, and compared with the results obtained from Shear 7 (Huang el al., 2007a, 2007d). It is found that the riser could experience multi-mode VIV in uniform current. It is also found that the CFD approach provides reasonable results. Hence it is feasible for deepwater riser VIV assessment. Further work is recommended in areas including (1) riser initial condition and its transient effect on VIV, and (2) riser modal coupling effect on VIV.

In conclusion, an effective CFD approach has been presented and applied to practical riser VIV assessment.

CHAPTER IX

3D SIMULATION OF FLOW PAST A CANETARY RISER IN UNIFORM CURRENT

As more and more oil and gas field developments are in deepwater regions and harsh environments, how to install the subsea equipment and flowlines safely and efficiently becomes a challenging subject that might require the support from the latest technologies. During a recent offshore subsea installation project in Offshore Brazil, some interesting phenomena were observed: (1) the flexible riser deflection in the water column was much higher than expected when subject to strong currents; (2) the curve on the sea floor tended to lose stability in a much lower current condition than predicted. Consequently, it caused difficulties and temporary schedule delay for the flexible riser installation. This paper is intended to realize what occurred to the flexible riser when it was subjected to strong currents, and provide theoretical evidence to support future engineering practice improvement and offshore installation guidelines (Huang et al., 2010).

Offshore Brazil is well known for the strong bottom current. The field measured current speed was up to 1.2 knot near the seabed. A recent project involved installation of more than 100 km of flexible flowlines and risers in a field located in the northern Campos Basin approximately 220 km northeast of Macae. It consisted of individually completed subsea production wells with gas lift and water injection wells tied back to a floating, production, storage, offloading (FPSO) vessel with flexible flowlines. The field

layout was fairly congested due to the sea bed bathymetric constrains, and included a number of sharp turns and low-radius curves. Engineering analytical work was done extensively to ensure smooth offshore installation operations. It worked well except for the flexible flowline curve laying in strong currents, which experienced some delay because the flexible flowline failed to maintain its position on the seabed and slipped out of its lay corridor. A snapshot of the plane view during the curve laying is illustrated in Fig. 112. The dotted line is the designed flowline position, or the target position to land the flowline onto during the installation. The solid line is the actual flowline position. The flowline is paid out from the installation vessel continuously, and it is suspended in the water column until it reaches the sea floor at the touchdown point (TDP). When strong current exists (most of the time it is from south), the flowline is pushed toward north due to the current drag force. Therefore, the catenary shape is bended toward north. The installation vessel monitors the flowline TDP and adjusts its position accordingly to ensure the flowline is laid within the allowable corridor. The illustrated flexible flowline was part of a production loop that begins and ends at the FPSO. Its field layout includes a 130m-radius curve to turn the flow direction back to the FPSO, as the dotted line indicates. The curve is stable if the soil friction is sufficient to hold the pipe in place against the bottom tension. Otherwise the curve won't be able to maintain (slippage occurs, as illustrated by the dashed line in Fig. 112). Pipe-soil friction coefficient was determined by the pipe and soil properties, and not related to the current. Therefore, the flexible flowline bottom tension becomes the controlling parameter for curve stability during installation, and it is directly related to the current strength. The

curve slippages occurred several times offshore when similar curves were being laid. To gain better understanding, transponders were deployed during the installation to measure the flowline deflections. It was found that the maximum flexible flowline deflection (hence the bottom tension) was underestimated during the installation engineering. A possible reason was VIV induced drag coefficient amplification, which was not considered in the installation engineering. It was believed that the flexible pipe has high structural damping and negligible VIV response since the design criteria for installation are much lower than those of in-place design. To confirm that, reliable flexible catenary riser VIV analysis is needed.

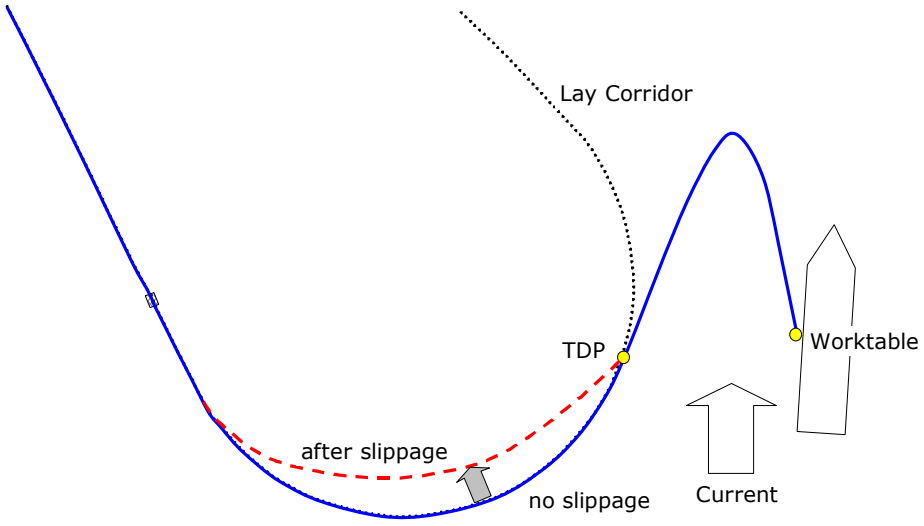

Fig. 112 Flexible Flowline Curve Laying Schematic

As of today there are very few publications on the flexible catenary flowline/riser VIV. Some of the reasons are: (1) the flexible flowlines are still relatively new for industrial deepwater application; (2) the flexible flowlines have good fatigue resistance performance and high structural damping, therefore, VIV induced fatigue was not as critical as the steel pipe risers; (3) the flexible flowlines consist of multiple layers that serve as different functions and have different material properties. The combined cross sectional properties are non-linear, project specific, and difficult to obtain and model; (4) The configuration and general layout of the flexible riser system are versatile and complex, and typically involve one or more catenary shapes, and also possibly other auxiliary components, such as buoyancy modules, buoys, clamps, bending restrictors/stiffeners etc. To the authors' knowledge, this study is the first among its kind to investigate a flexible catenary riser VIV using CFD approach.

In fact the flexible flowlines have been increasingly used for deepwater and ultra-deepwater field applications, partially because of their fatigue resistance performance and low submerged weight.

It is estimated that the linearized bending stiffness of the subject flexible flowline is about 100 kN-m^2. During its installation, a layback distance of 100 m was used, which corresponded to 1 deg nominal departure angle at the worktable. The suspended length of the flexible riser is 1,100m (L/D=3,300). The current speed could ramp up quickly, in terms of several hours, from near zero to a peak value ranged from 0.7 knot to 1.2 knot. ROV was sent to measure the current profile from time to time. It was found that the current profiles were fairly uniform starting from the sea bed to about 200 m below the

mean surface line. For the sake of simplicity, we used uniform current of 0.7 knot throughout the water column for the VIV simulation.

In the present simulations, the flow field around the riser was discretized by 1.5 million finite elements, and solved numerically in time domain. The riser lateral displacement was decomposed into three components: (1) catenary shape due to the riser weight, (2) in plane motion due to the current drag force, and (3) out-of-plane motion due to the lift force. The total riser deflection was the superposition of these three components. The flexible flowline maximum deflections and equivalent drag coefficients were studied and compared to the field measurements.

The data grid is shown in Fig. 113. It consists of 3 overlapping parts that serve different purposes: (1) body grid – the data grid adjacent to the riser surface that provides fine resolution to calculate the fluid-riser surface interaction and vortex generation, it has dimensions of 50 x 182 x 35, (2) wake grid – it interfaces with body grid and background grid and provides good resolution for vortex propagation, it has dimensions of 50 x 121 x 101, (3) background grid –it defines the outer boundary of the computational fluid domain, provides the far field flow boundary conditions, interfaces with and provide a physical extension to the wake grid using relatively coarse mesh. It has dimensions of 50 x 121 x 91.

The flexible riser was also discretised into 250 segments. Its lateral displacement consists of three components as follows:

1. The static catenary shape. For a flexible flowline with uniform cross section, its catenary shape is given by: $z = a\left[\cosh\left(\frac{L+x}{a}\right)-1\right]-h$, where L is the

layback distance, h is the vertical distance between the flexible flowline hang-off position to its TDP on the seabed, a is a constant determined by the departure angle: $a = \frac{L}{\sinh^{-1}(\cot\beta)}$, and β is the nominal departure angle.

The origin of the coordinate system was chosen at the worktable (the flexible pipe hang-off location). The static catenary shape is always in the vertical plane determined by the worktable location and the flexible flowline TDP.

2. Riser response due to the drag force. The response can be decomposed into in plane and out of plane components. Note that the drag force is time dependant, and was calculated by integrating the pressure force and viscous force along the riser surface in the current flowing direction.
3. Riser response due to the lift force. The response can be decomposed into in plane and out of plane components. It was calculated by integrating the pressure force and viscous force along the riser surface in perpendicular to the current flowing direction.

The riser instantaneous displacement is the summation of the above three displacement vectors at each time step. The main advantages of this method are: (1) the catenary shape is calculated statically, and simple catenary equation could be used. This would avoid a complex dynamic catenary solver, (2) a simple tensioned beam motion equation was applied to calculate the riser dynamic vibrations. This equation has a fairly stable differential scheme, and provides reliable solution to the riser motions. The disadvantage is that it is difficult to include the pipe-soil interaction into this simplified

model. Since in this study the primary focus is on the overall flexible flowline VIV behavior and its impact on the effective drag coefficient, this model provides sufficient performance.

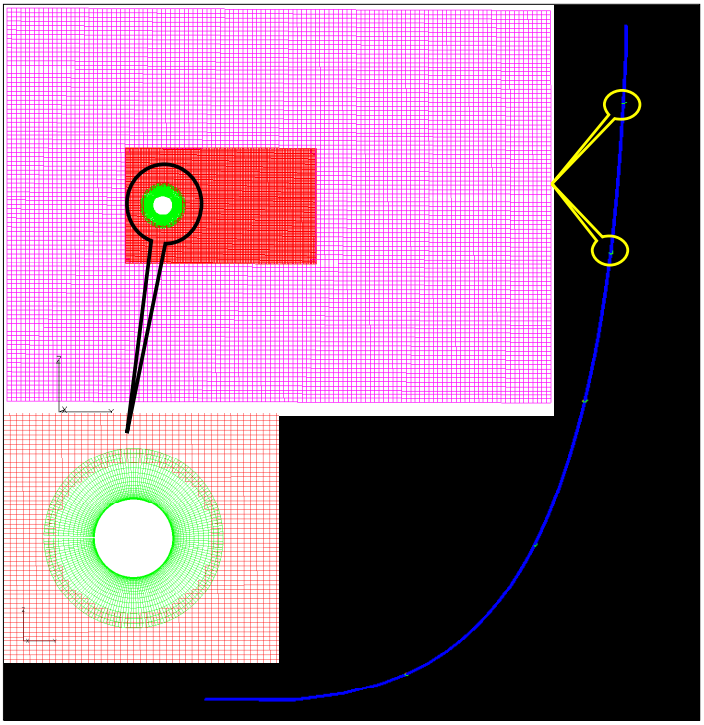

Fig. 113 Data Grid along the Flexible Riser

Modal analysis was performed to provide the modal frequencies and modal shapes. The modal shapes were separated into in plane modes and out of plane modes based on vibrating planes. The fundamental frequencies are 98 seconds for in plane and 122 seconds for out of plane respectively. Fig. 114 compares the normalized modal shapes of the in plane and out of plane fundamental modes. It shows that the in plane

mode has different behavior from the out of plane mode. The in plane mode has two peaks. Except the major peak (normalized to 1.0), it also has a minor peak about -0.15 near the TDP region. When the flexible flowline has in plane deflection, its TDP will move in the opposite direction. This would reduce the effective length of the modal shape, and increase the modal frequency. It is one reason that the in plane fundamental modal frequency is slightly higher than that of the out of plane. Other reasons are the added mass difference and static curvatures. When the flexible flowline vibrates in the catenary plane, its velocity direction is not perpendicular to the flexible flowline. Therefore, the effective added mass coefficients are less than that of the out of plane case. Also the static curvature (from the catenary shape) could impact the flexible flowline behavior as well. The modal frequencies of the first 10 modes are listed in Table 4. It shows the discrepancy between the modal frequencies for the in plane and the out of plane modes reduces when the modal number increases. This is expected since the vibration becomes more and more localized for high modes. And in high modes the local curvatures increase dramatically such that the catenary shape induced curvature (static curvature) has negligible effect on the local behavior.

Table 4 Flexible Catenary Riser Modal Frequency

Mode No	Out of Plane		In Plane	
	T (sec)	f (Hz)	T (sec)	f (Hz)
1	122.0	0.008	97.8	0.010
2	59.2	0.017	50.2	0.020
3	39.2	0.025	34.1	0.029
4	29.3	0.034	25.9	0.039
5	23.4	0.043	21.0	0.048
6	19.5	0.051	17.6	0.057
7	16.7	0.060	15.2	0.066
8	14.6	0.068	13.4	0.075
9	13.0	0.077	12.0	0.084
10	11.7	0.086	10.8	0.093

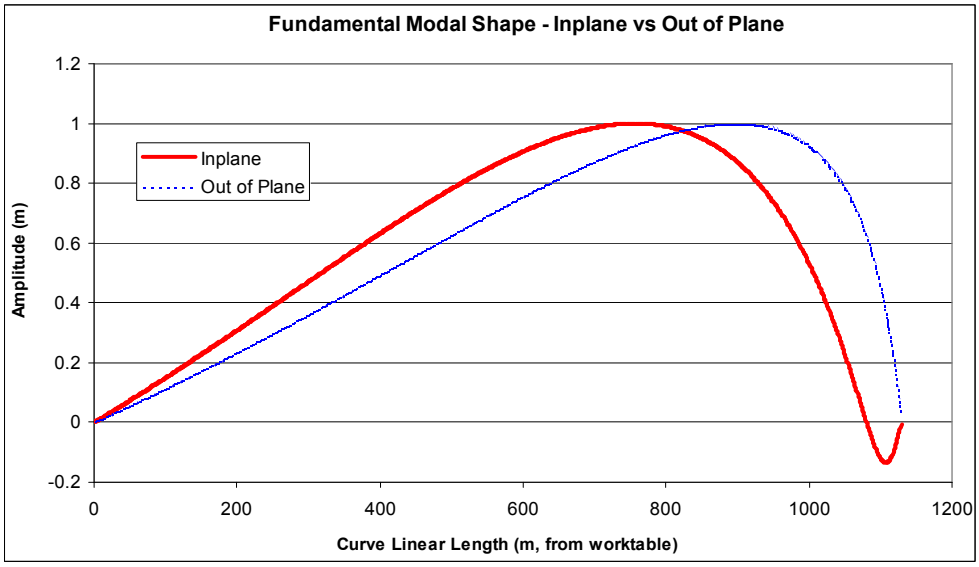

Fig. 114 Flexible Catenary Riser Fundamental Modal Shapes

Simulation Results

In the simulation, 0 degree current heading was used (or the current is from the far direction). This is the worst condition for the flexible flowline curve stability since it gives the maximum bottom tension at the TDP. The current speed was 0.7 knot. This speed was observed frequently during offshore installation and was selected for this study. It corresponds to a Reynolds number of 1.05×10^5. The time step for the numerical simulation was chosen as 0.009 s, which is sufficiently small for the dominant modes. The duration of the simulation is 20,000 time steps, or 180 seconds. Fig. 115 illustrates the flexible riser deflection and vortex development and shedding process. The flexible riser started with a static catenary shape. When it was subject to strong current, it deflected in current direction due to the drag forces. At the same time, it also started cross flow vibrations due to the lift forces.

The results showed that the maximum riser deflection was near the bottom region, where the effective tension was low. Typically the flexible flowline bottom tension was around 1~2 Te, while the top tension could be more than 20 Te. The bottom tension is adjustable in a limited range by positioning the installation vessel and varying the layback distance. Nevertheless, the bottom tension of a catenary riser is always low regardless of the flexible riser properties. It is expected that the flexible riser behavior near the bottom is different from its upper portion because of this low tension characteristics, and it is common among all catenary risers.

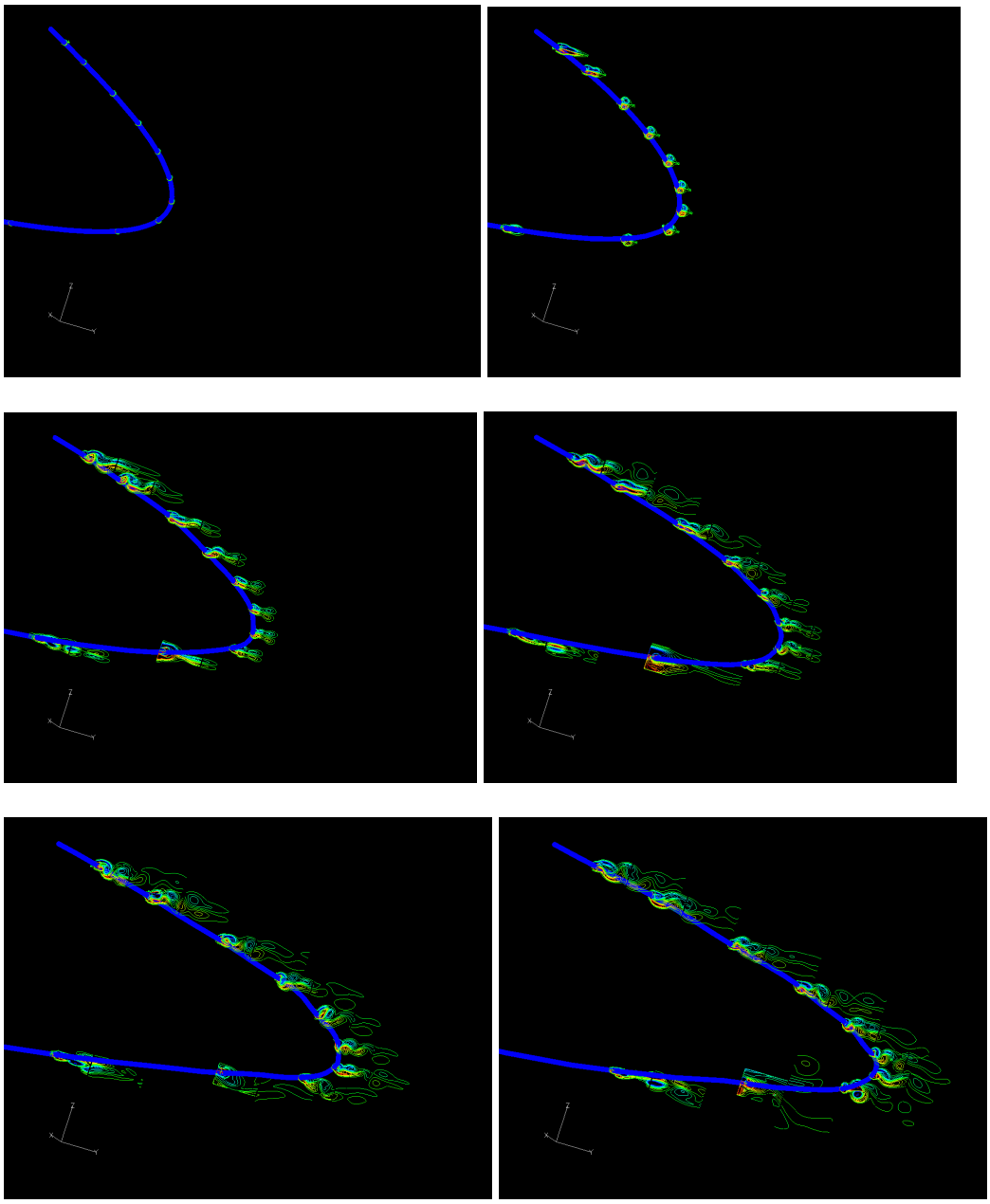

Fig. 115 Flexible Catenary Riser VIV Evolution Illustration (Top View)

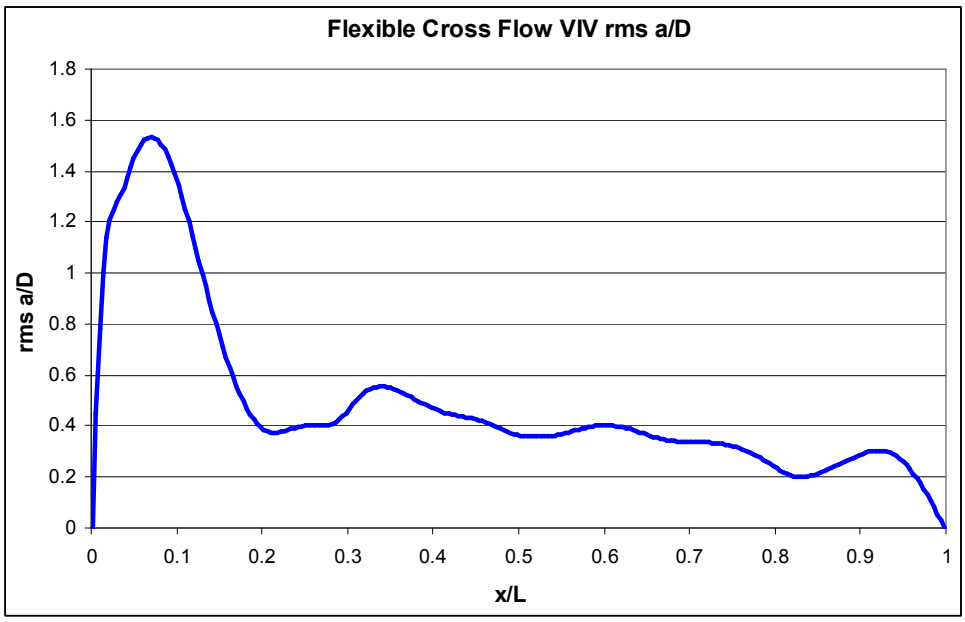

Fig. 116 Cross Flow VIV rms a/D, U=0.7knot

The flexible flowline VIV includes both in plane and cross flow vibrations. Usually the VIV amplitudes are in the order of 1D, which is negligible comparing to the flexible flowline in plane deflection. Therefore, the in plane VIV is of less interest. The cross flow VIV rms a/D was plotted in Fig. 116. x/L=0 corresponds to the bottom of the flexible flowline (TDP), while x/L=1.0 corresponds to the top of the flexible flowline (worktable). It shows the flexible flowline experienced cross flow VIV, and its rms a/D distribution consists of two portions:

- The upper portion with rms a/D ranging from 0.2 to 0.6. This range is consistent with a typical top tensioned riser. The rms a/D indicates a downward trend when x/L increases. This is expected since the riser tension

increases as the elevation gets higher. And the response rms a/D correlates to the tension distribution very well.

- The bottom portion with rms a/D as high as 1.5. This response is very high. Seems it is related to the near-zero bottom tension. This region includes the lowest 20% of the total riser length.

Overall, the results indicate that the catenary riser VIV will have different VIV response pattern than the top tensioned risers. Its low tension / near-zero tension zone could show complicated behavior that requires particular attention during numerical simulations. It also indicates that the dominant modes should be less than the 10^{th} mode, based on the rms a/D distribution shapes.

The flexible flowline maximum in plane displacement is a critical parameter of this VIV study. During offshore installation transponders were attached onto the flexible flowlines to identify the actual catenary shape when strong current exists. It was found that the flexible flowline could be pushed 80 m to 90 m away from the vertical line at the worktable when the measured current was around 0.7 knot. Fig. 117 shows the flexible flowline maximum deflection from the VIV simulation. The maximum deflection of 70 m occurs near the bottom. Considering the uncertainty of the field measured current profile and the varying nature of the current speed and direction, the flexible flowline maximum deflection from the VIV simulation is in a reasonable range. The flexible flowline deflection is quite large, and excessive riser displacement causes problems such as: (1) lose curve stability when the current is from the far or cross direction; (2) lose control of flexible flowline laying at the TDP, form pig tail loops on the sea floor and

infringe the flexible flowline minimum bending radius when the current is from the near direction; (3) interfere with nearby installed equipment or existing facilities. Interference with wet parked mooring lines was observed offshore. The flexible flowline also clashed several times with the ROV tethers. Consequently, accurate prediction of the flexible flowline deflection and positions in strong current is critical to plan the installation activities accordingly and manage the risks associated with the adverse environmental conditions.

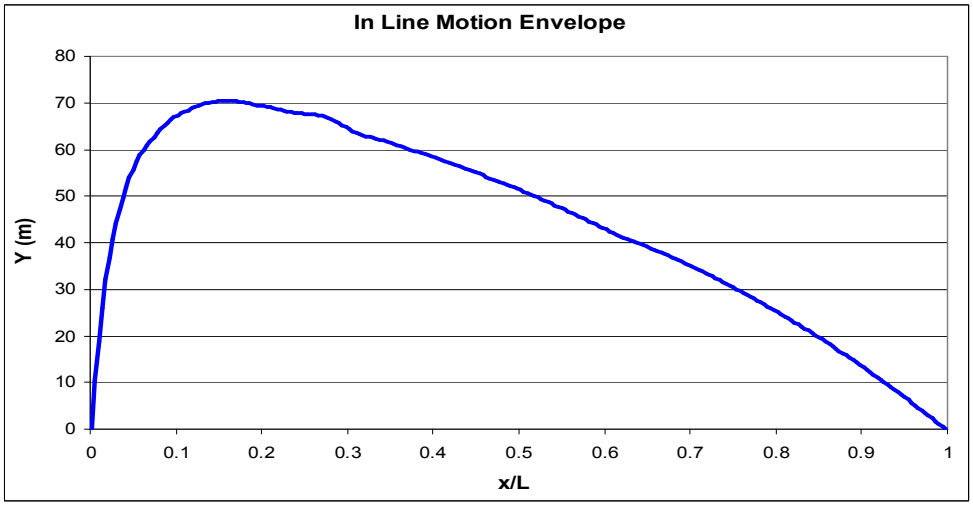

Fig. 117 Flexible Flowline Maximum Deflection, U=0.7knot

The flexible flowline effective drag coefficient is also of interest since it is a normal practice to use an effective drag coefficient instead of time consuming CFD approach for offshore installation engineering. Current design codes (such as API RP 2RD) provide drag coefficient selection criteria, which depend on Reynolds number. In the studied case the Cd is between 1.0 to 1.2 for $Re=10^5$ for a fixed cylinder. When the cylinder undergoes VIV in current, the effective drag coefficient could be higher because the riser lateral movement increases the equivalent drag area. The drag coefficient was calculated during the VIV simulations at each time step and each location along the riser. The instantaneous drag coefficient depends on the riser movement and flow field condition, and may vary dramatically in a wide range. Its impact on the riser deflection is mainly determined by the time-averaged value. Fig. 118 shows the average Cd distribution along the riser. It shows that the drag coefficient of the riser upper portion is between 1.0 to 1.5. At the riser bottom, the drag coefficient varies in a larger range, from 0.5 to 2.5. Some observations are as follows:

1. By comparing Fig. 118 to Fig. 116, it shows the drag coefficient at the riser bottom has strong correlation to the cross flow VIV amplitude at that region. The drag coefficient could be either amplified or suppressed significantly.
2. The VIV induced Cd amplification is obvious at the top half of the riser, where its tension is high.
3. The average Cd along the riser is approximately 1.3, which is 10~20% higher than the Cd for the fixed riser condition.

Overall, the results indicated that for catenary risers, high VIV amplitude does not necessarily result in high effective Cd. A possible reason could be the dominant VIV response frequency. The catenary risers have very long fundamental modal frequencies. Based on a Strouhal number of 0.2, it is estimated that the vortex shedding frequency is 0.21 Hz (4.7 s), which corresponds to the 23rd modal frequency. However, it is unlikely that the 23rd mode could be excited since the flexible flowline has high structural damping that tends to dampen out any high frequency vibrations. This can be confirmed from Fig. 116 since it does not show any indications of high frequency modal response.

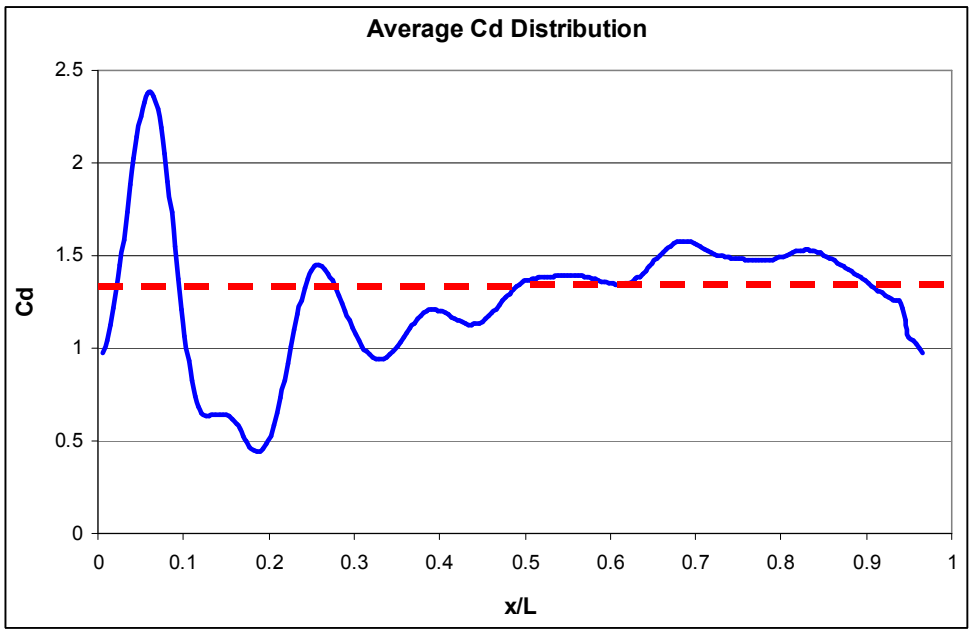

Fig. 118 Drag Coefficient Distribution, U=0.7knot

Discussions

This chapter studied a flexible riser VIV using a CFD approach. The flexible riser parameters and environmental conditions were obtained from a recent installation project in offshore Brazil. During the offshore installation, it was found that the flexible riser could have higher lateral deflection than expected when subject to strong current. The selected case was simulated in time domain using proven CFD technology in conjunction with a simplified catenary riser motion solver. The simulation details were presented, and the maximum riser deflection was also compared to the field measurement. It is found that:

1. The flexible riser VIV response is complicated by its low tension at its bottom section (near seabed region). In this region the flexible riser could have large VIV response and sensitive drag coefficients.
2. The flexible riser VIV response reduces along the riser and reaches its minimum at the top. This distribution correlates well to the riser effective tension distribution. It confirms that high tension would result in low VIV response.
3. The average effective drag coefficient is up to 20% higher than the fixed riser condition. A maximum deflection of 70 m was observed in the riser VIV simulation with uniform current speed 0.7 knot, which is consistent with offshore observations.

Note that the present approach could be further improved by refining the catenary riser motion solver. Some recommendations are:

1. Inclusion of the riser-soil interaction. When the riser moves, the riser TDP also moves, both axially and transversely. And the riser section on the seabed will experience both the vertical loads and lateral friction force. These nonlinear behaviors need to be modeled in order to accurately predict the riser bottom VIV response.
2. Inclusion of the flexible flowline bending hysteretic curves. The flexible flowline has strong nonlinear properties, especially the bending stiffness.

In summary, the simplified catenary riser motion solver worked well, and the simulation results are reasonable. The results showed that the flexible riser VIV could increase the effective drag coefficient by 10~20%, which partially explains the phenomenon of high flexible riser deflection observed offshore.

CHAPTER X

3D SIMULATION OF FLOW PAST A PARTIALLY SUBMERGED JUMPER IN UNIFORM CURRENT

This chapter studied the VIV of a flexible jumper. Flexible jumpers are widely used in oil and gas industry to transport liquid or gas content between two facility units, usually located close to each other and have relative movement. In many of its applications, the jumper is positioned near the water surface, sometimes surface piecing, hence subject to severe environmental loads, including strong surface currents. This paper is to study a flexible jumper VIV in uniform current by using a CFD simulation approach (Huang et al., 2011).

Fig. 119 shows a typical jumper arrangement. In this hypothetical case the jumper's first end is attached to a submerged facility at 50 m below the mean surface level, and its second end is attached to a hang-off porch at 30 m above the mean surface level. The nominal horizontal span is 200 m. The jumper has a diameter of 0.33 m, and total length is 265 m (L/D=800). Its air weight is 100 kg/m, and submerged weight 20 kg/m (mass ratio=1.0). The mass ratio is $m/\rho D^2$ (Vandiver, 1993). A uniform current of 0.5 m/s (1knot) is applied in the direction perpendicular to the jumper catenary plane.

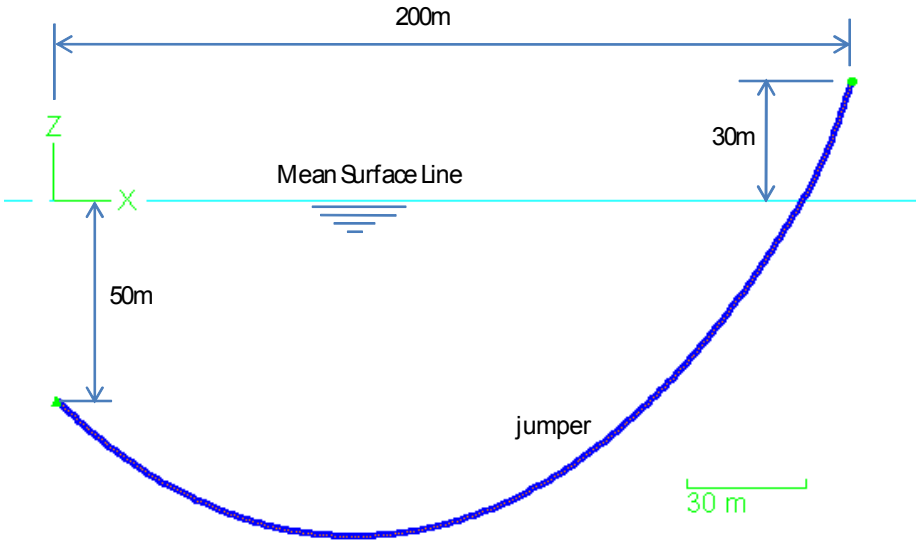

Fig. 119 Jumper General Arrangement

This study is the first to study the surface piecing cylinder VIV using 3D CFD simulation approach. The publications on VIV 3D simulation of catenary risers are rare, except for the one we published on a flexible riser VIV (Huang, Chen & Chen 2010). This study is a continuous effort on the VIV simulations on catenary type of risers. The main challenges of the jumper VIV simulation are:

1. The jumper tension level is fairly low. The jumper could have large lateral deflection when subject to strong current flow. This lateral movement causes high deformation on the data grids, and imposes difficulty on fluid-structure solver. And very fine time steps have been used in the simulation to ensure the simulation accuracy.
2. The apparent mass distribution along the jumper is not uniform, and disconnection exists at the mean surface level. The jumper configuration

cannot be represented by the simple catenary equation. A trial and error approach is proposed in this paper to calculate the catenary shape. The non-uniform apparent mass distribution also requires fine mesh on the riser.

3. The effective tension distribution is non-linear and its amplitudes vary in a large range. The modal shapes also show strong non-linear behavior, and are not orthogonal to each other. In order to extract the modal components, a least squares method is adopted.
4. The jumper cross flow VIV response could be influenced by the lateral motions, and contains transient dynamic response. A filtering methodology is presented in this paper to better interpret the VIV response results and characteristics.

In this study we first developed a static catenary solver to determine the jumper configuration. The upper section (about 10% of overall length) of the jumper is in the air, and the lower section (about 90% of the overall length) is submerged in the water. The static catenary solver is capable of handling cable catenary shapes with arbitrary mass distributions. Then the modal frequencies and modal shapes were derived and examined. The jumper cross flow transient response was also simulated and its modal component distribution was studied. After that a uniform current of 1 knot was imposed as far field incoming current, and the jumper dynamic responses were simulated in time domain. The vortex shedding details were plotted and examined. The cross flow VIV rms a/D was also calculated and compared to the results predicted by Shear 7. Other important parameters, including dominant modes, modal components, and motion

trajectories, were derived and studied as well. It is found that the jumper cross flow VIV may contain more than one modes with similar strength. And the VIV amplitudes correlate well to the effective tension distribution. It is also noticed that the jumper motion trajectories show complex behavior, and may not follow figure “8” pattern. In conclusion, the jumper VIV was simulated in time domain, and reasonable results were obtained. The validity of the proposed CFD approach was also confirmed through the results comparisons.

The data grid is shown in Fig. 120. It consists of 3 overlapping parts that serve different purposes: (1) body grid – the data grid adjacent to the jumper surface that provides fine resolution to calculate the fluid-jumper surface interaction and vortex generation, it has dimensions of 50 x 182 x 35, (2) wake grid – it interfaces with body grid and background grid and provides good resolution for vortex propagation, it has dimensions of 50 x 121 x 101, (3) background grid –it defines the outer boundary of the computational fluid domain, provides the far field flow boundary conditions, interfaces with and provide a physical extension to the wake grid using relatively coarse mesh. It has dimensions of 50 x 121 x 91.

The non-dimensional time step is selected to be 0.01 (fluid particle travels 1 diameter distance in 100 time steps), which is sufficiently small to avoid possible numerical instabilities and ensure calculation accuracy.

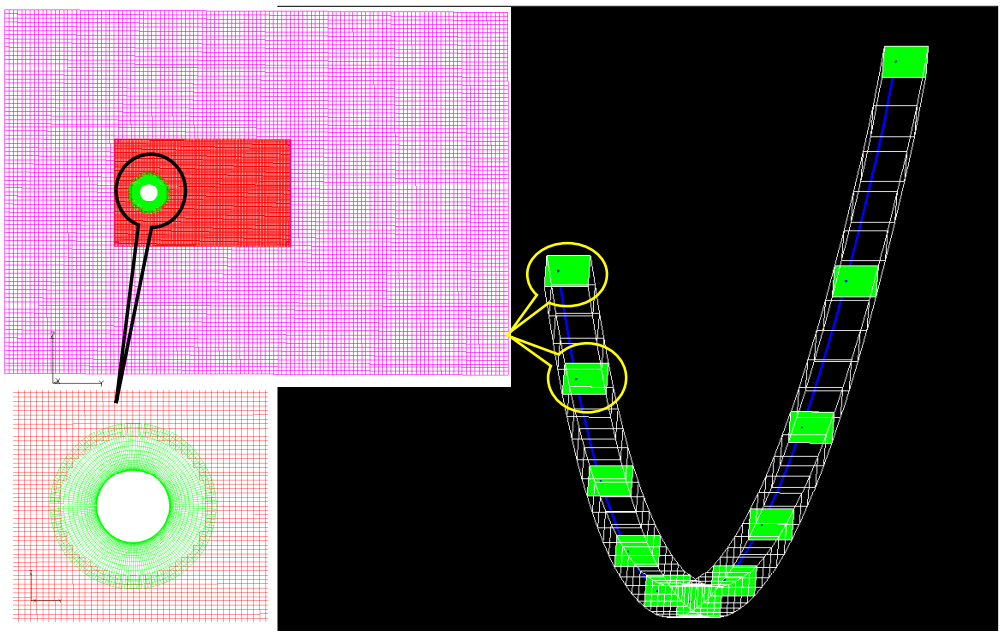

Fig. 120 Data Grid along the Flexible Jumper

Simulation Results

In the simulation, a uniform current perpendicular to the jumper catenary plane was applied. The current has a velocity of 0.5 m/s. It corresponds to a Reynolds number of 1.5×10^5. The dimensional time step for the numerical simulation was chosen as 0.0066 s, which is sufficiently small for the dominant modes. The duration of the simulation is 20,000 time steps, or 130 seconds. The flexible jumper started with a static catenary shape. When it was exposed to the uniform current, it deflected in the current direction due to the drag forces. At the same time, it also started cross flow vibrations due to the lift forces. Fig. 121 shows one snap shot of the jumper undergoing VIV at time step=20,000. Note that the top portion of the jumper is above the mean surface line, and the vortex shedding occurs only on the submerged portion of the jumper.

Fig. 122 shows the jumper mean deflection in the current direction. The results show that the jumper has a maximum deflection of 65D, which occurs at the vertex, the bottom of the sagging bend with the lowest effective tension. The mean deflection is two orders of magnitude larger than the cross flow VIV amplitudes. Therefore, any slight variation of the mean deflection would have significant influence on the fluid environment surrounding the jumper, and impact the lifting coefficient and cross flow VIV.

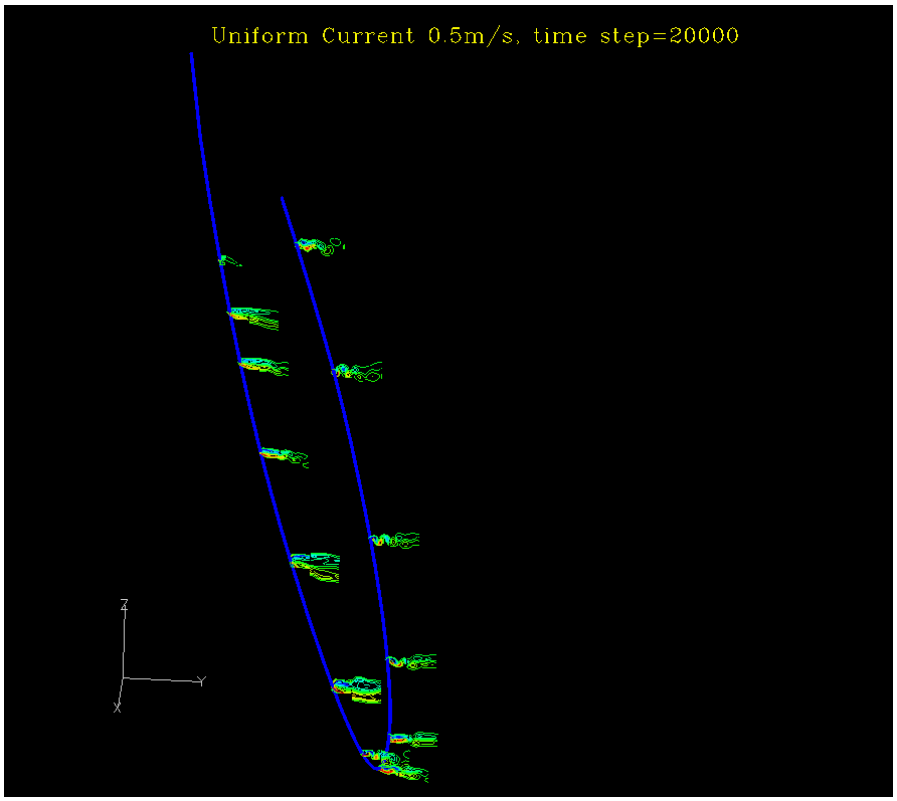

Fig. 121 Jumper VIV Snapshot, Time Step=20,000

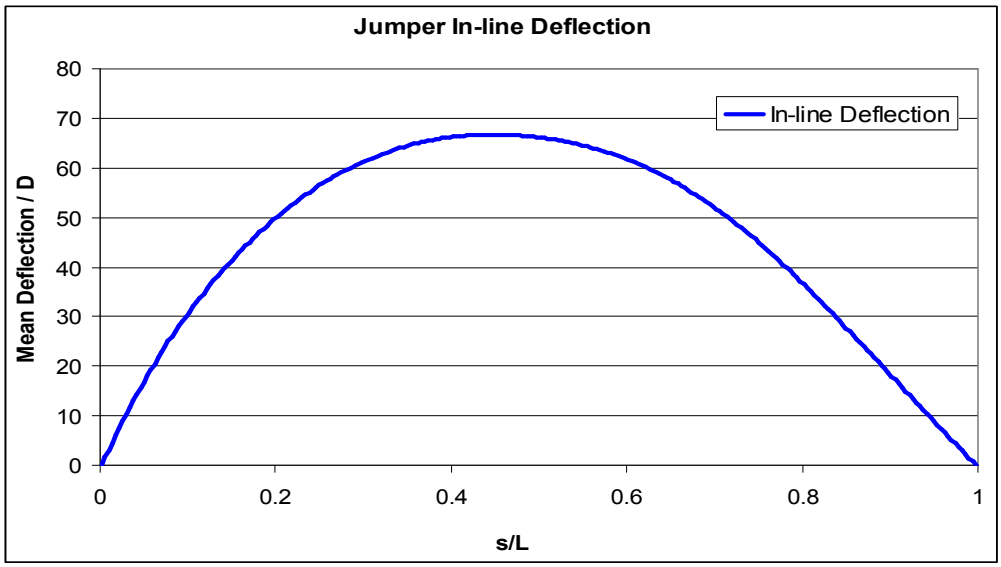

Fig. 122 Jumper Mean Deflection due to Current Drag Force

In general, the vortex shedding shows clear "2S" pattern (Williamson and Roshko, 1988) along the jumper. Fig. 123 and 124 show the snap shots (time step=18,600) of the vortex shedding and vorticity contours at two locations: s/L=0.25 and s/L=0.5 respectively. At each location, the vortex shedding details on three adjacent stations (spaced at 15D apart along the jumper) were plotted. It shows that the vortex shedding frequency and vorticity contour are very similar within this +/-15D span. It can also be observed that the vortex shedding phase angle (relative to the jumper) shifts gradually along the jumper. If the jumper were rigid and fixed (no movement), the vortex shedding along the jumper would be very similar. Therefore, it seems the jumper motion is the main reason of this vortex shedding phase angle difference. On the other hand, the jumper movement could also be inferred from the vortex shedding behavior as well:

- The forming vortex always follows after the jumper cross flow motion, i.e. the forming vortex is below the jumper when the jumper moves up, and the forming vortex is above the jumper when the jumper moves down.
- The vorticity contour indicates the vortex separating distances. A decreasing vortex spacing indicates the jumper moves forward in the current direction, and a increasing vortex spacing indicates that the jumper is moving back against the current.

The vortex shedding pattern also provides indications of the power in and power out zones. In the present case, the jumper is subject to uniform current, and the power in and power out zones correspond to the whole span of the submerged portion.

The flexible jumper VIV includes both in plane and cross flow vibrations. Usually the VIV amplitudes are in the order of 1D, which is negligible comparing to the jumper in-line deflection (two orders higher). As a result, the in-line VIV is obscured by the deflection variation. It is also of less interest than the cross flow VIV from practical application point of view. The cross flow VIV rms a/D along the jumper was plotted in Fig. 125. As a comparison, the results predicted by the Shear 7 were also included. The Shear 7 calculations were based on recommended default parameter values. Both Shear 7 and FANS predicted the cross flow is dominated by the 5^{th} mode. Discrepancies exist on the peak value envelopes. Overall FANS predicted lower rms a/D, especially when s/L>0.3. Possible reason is that Shear 7 assumed a single mode (5^{th} mode) lock-in, while FANS is based on fluid-structure interactions, and is not selective among any participating modes. Actually the time domain simulation by FANS has shown the 6^{th}

mode was also excited with slightly less energy than the 5th mode. In other words, Shear 7 assigned 100% of the VIV response energy to the 5th mode, while FANS predicted that the VIV response energy was largely shared between the 5th and the 6th modes. This also explains the slight difference of the peak and trough positions along the jumper. Nevertheless, the results show reasonable agreement between FANS and Shear 7, with consideration of the different VIV prediction methodologies.

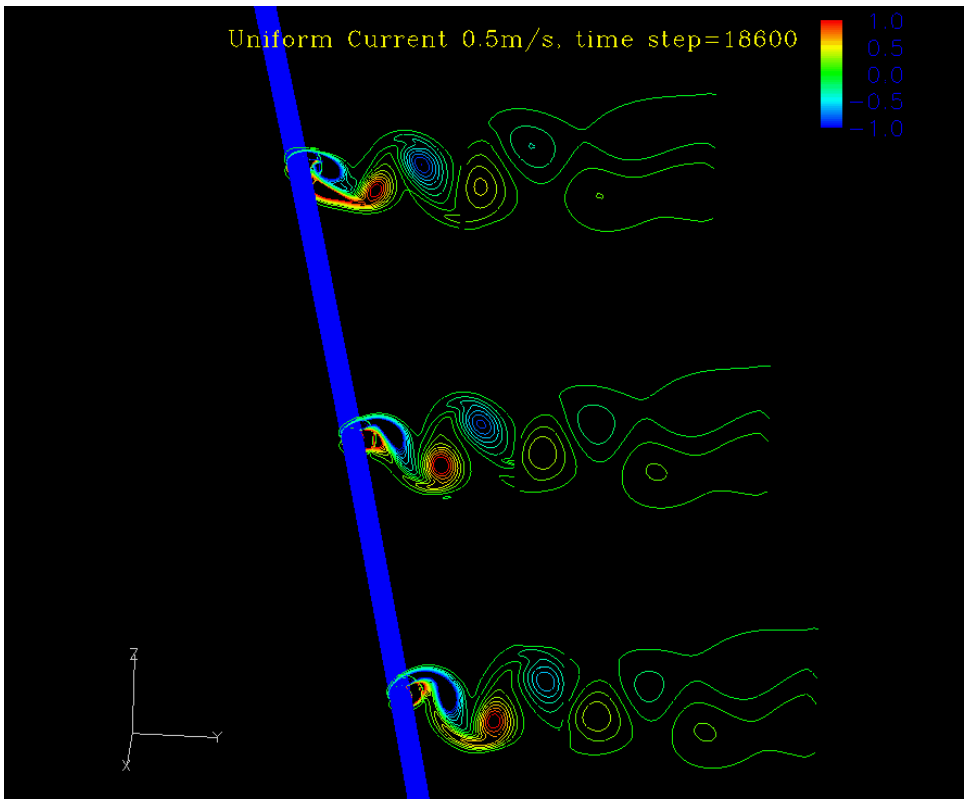

Fig. 123 Jumper VIV Vortex Shedding Pattern, s/L=0.25

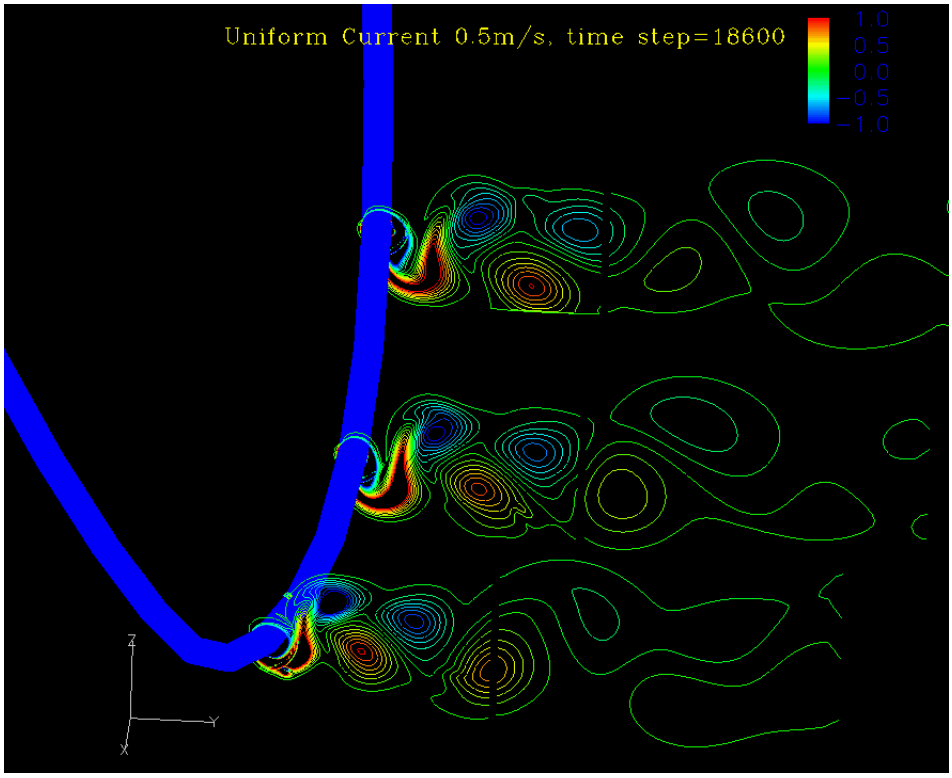

Fig. 124 Jumper VIV Vortex Shedding Pattern, s/L=0.5

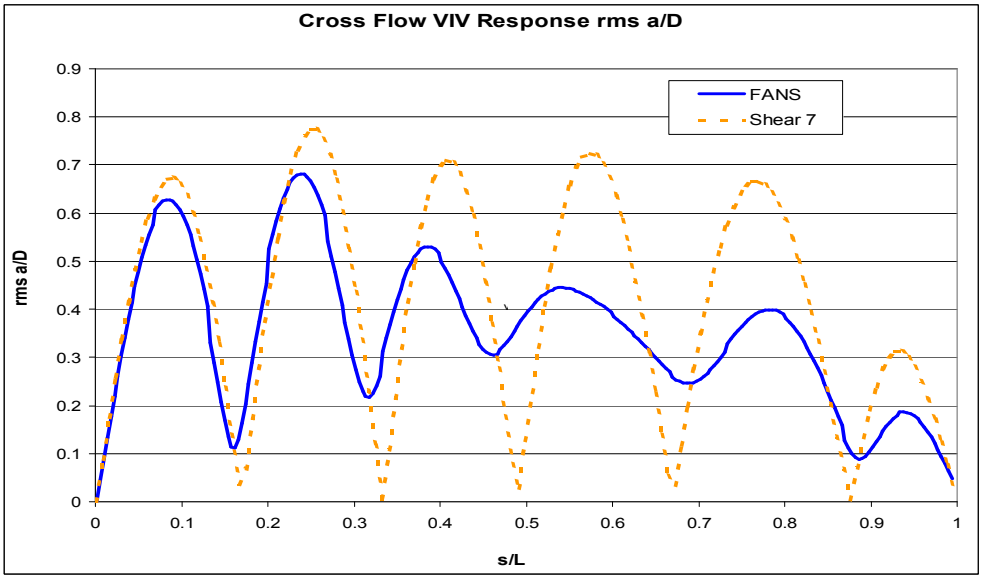

Fig. 125 Cross Flow VIV rms a/D

The jumper cross flow motion time histories were decomposed into modal response, and the rms a/D for each modal component is presented in Fig. 126. The top figure is the modal components of the total motion, and the bottom figure is the filtered modal components, which represent the cross flow VIV response better. The modal components of the transient response were estimated to be $rms_i = 0.4116e^{-0.1412i}$, i=1 to 25. The filtered modal components show that the jumper cross flow VIV is dominated by the 5th mode, which contributes more than 60% of the cross flow VIV energy (measured by rms_i^2). The 6th mode was also excited, and it contributes about 40% of the VIV energy. Other modes may also exist, but with insignificant contributions. This multi-modal response observation is consistent with Willden and Graham (2004).

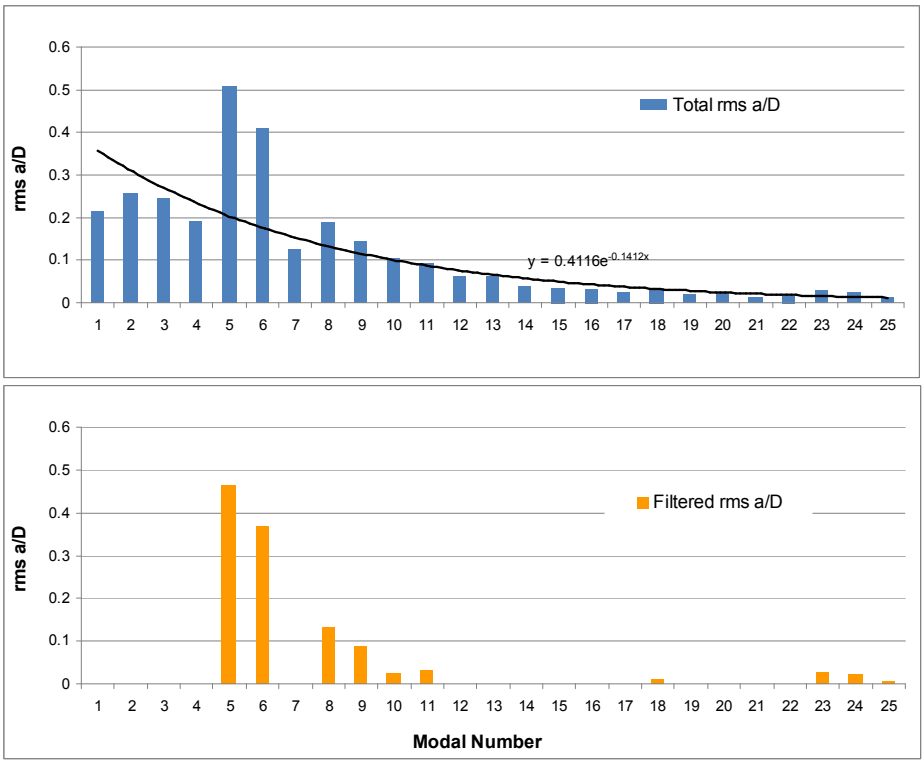

Fig. 126 Jumper Motion Modal Decomposition

The jumper motion trajectories were plotted at eight stations: s/L=0.1, 0.2, 0.3, 0.4, 0.5, 0.6, 0.7, 0.8, as shown in Fig. 127. The horizontal axis is the current flow direction, and vertical axis is in the cross flow direction. The trajectories were plotted in the same scale to facilitate the comparison. The trajectories confirmed that the jumper VIV behavior in 3D is much more complex than in 2D (rigid cylinder motions), where the trajectories usually follow figure "8" or deformed figure "8" pattern. The jumper motion does not exhibit regularity. Instead, it shows certain degree of random behavior. The main reason is the lateral offset fluctuations. The mean lateral offset could vary in a range of 1D near the two ends, and up to 8D at the central portion of the jumper.

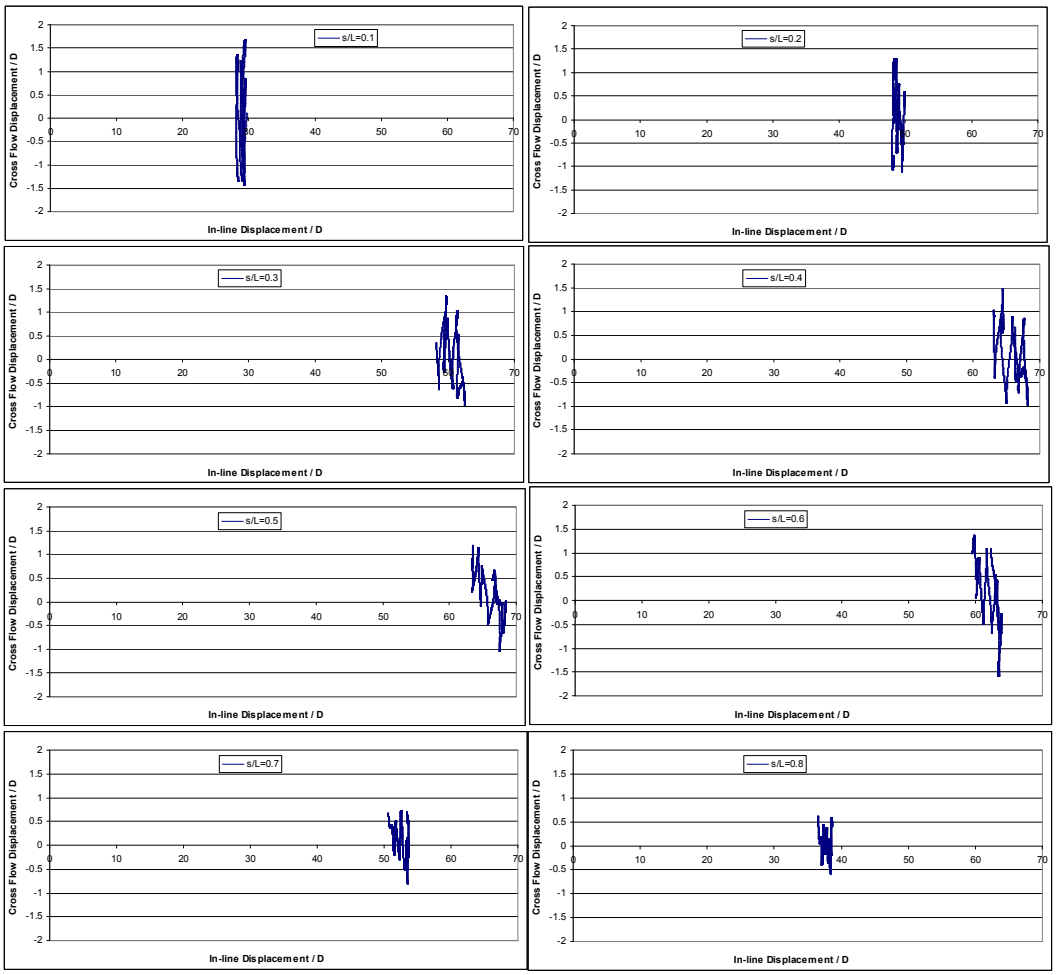

Fig. 127 Jumper Motion Trajectory

Discussions

This chapter studied a partially submerged flexible jumper VIV using a CFD approach. The flexible jumper size and arrangement are based on a hypothetical offshore field application case. The simulation results, including vortex shedding details, rms a/D, modal analysis, modal decomposition, and motion trajectory were presented. The cross flow rms a/D was also compared to those calculated by using Shear 7, and reasonable agreements were observed. The conclusions are:

1. The jumper modal shapes are not orthogonal. The least squares method works well for modal extraction, and is able to extract any number of modal components. It is recommended to include all the modes below the cut-off mode, which is determined through the reduced velocity range.
2. The flexible jumper VIV response is complicated by its large lateral deflection, which is two orders of magnitude higher than the cross flow VIV amplitudes. Slight change of the drag force is equivalent to relocate the jumper to a new equilibrium position, and consequently influence the cross flow VIV response. On the other hand, the jumper in-line mean offsets and motions need to be carefully considered during jumper VIV time domain simulation because of their influence on the simulation results.
3. The modal response of the transient effect could be approximated by an exponential function, which provides an option to filter the transient response from cross flow VIV.

4. The dominant mode may not necessarily be locked-in. The simulation results showed the dominant mode may allow the co-existence of other participating modes with similar strength.
5. The jumper motion trajectories are not likely to follow simple figure "8" patterns, as typically seen in 2D or rigid cylinder VIV. This suggests that the long catenary cylinder VIV may intrinsically include certain degree of random behavior, and require statistically approach to gain better understanding.

In summary, a simplified catenary riser motion solver has been applied to the VIV simulation of a partially submerged jumper, and it worked well. The time domain simulations showed reasonable results, and disclosed valuable details on the jumper VIV. The paper also presented the methods for modal components extraction and transient response filtering, which are essential for jumper VIV results interpretation. It also confirmed that the present approach is valid for catenary jumper VIV simulation, and is applicable for complex VIV problems involving partially submerged risers, flowlines, jumpers, and cables.

CHAPTER XI

SUMMARY AND CONCLUSIONS

In this dissertation we have successfully simulated the VIV of some long risers in uniform and shear currents. We developed a riser modal motion solver and a direct integration solver to calculate riser dynamic motions when subject to external forces. The direct integration solver provides good flexibility on inclusion of riser bending stiffness and structural damping coefficients. We also developed a static catenary riser solver based on trial and error iteration technique, which allowed the motion solvers to handle catenary risers and jumpers with arbitrary mass distributions. We then integrated the riser motion solvers to the existing FANS code, and applied to a series of riser VIV problems. First, we simulated the flow field around a fixed and a vibrating riser, and compared the flow field to Huse's formula (experimental data). The simulation results show good agreement, which confirms the effectiveness of both the FANS codes and data grids. At the same time, we disclosed the "high speed" zone behind the riser and illustrated its influence on the deepwater riser interference. We then extruded the data grid in axial direction, and applied the same data grids or its variations to a series of long riser VIV simulations. To facilitate the comparison to published experimental data, we selected one riser vertically positioned and with L/D=480 when subject to uniform and shear currents, and one riser horizontally positioned and with L/D=1,400 when subject to uniform and shear currents. We chose to discretize the cross-sectional flow plane with deliberately generated fine elements, while use relatively coarse elements in spanwise

direction to keep the total element number of the interested fluid domain less than 1.5 million, which is within the computational capability of a regular PC. The VIV response of both risers showed good agreement with the experimental data. It is found that the riser has much less lateral displacement in shear current than the corresponding uniform current, and the power-in and power-out zones could also be easily identified through the vortex shedding pattern. After successful simulations of these two constantly tensioned horizontal risers, we proceeded with some simulations of a typical vertical riser for 3,000 ft water depth. This top tensioned riser has much lower tension at the bottom than the top because of its own gravity force. The results showed that the riser bottom has much higher VIV response amplitudes than the top of the riser. This is reasonable since lower tension is usually associated with higher lateral flexibility. The VIV simulation results also showed good agreement with results predicted by Shear 7. We also applied the same CFD approach to a 1,100 m catenary flexible riser VIV simulation. The simulation results showed similar lateral offsets as observed in field, and confirmed that the VIV is one of the main reasons for the drag force enhancement on the flexible riser. Last, we simulated a 265 m catenary flexible jumper VIV when it partially submerged a uniform current. The simulation results agreed well with the results predicted by Shear 7, and further confirmed that the cross flow VIV response is sensitive to the riser in-line deflections. To process the simulation results, we developed a VIV induced fatigue calculation module based on rain flow counting technique and S-N curve method. We also developed a modal extraction module based on least squares method.

In summary, we developed a CFD method that applied it to a series of different long riser VIV simulations, processed and studied the details, including flow field vorticities, rms a/D, riser motion trajectories, PSDs, modal components, VIV induced stress characteristics, and VIV induced fatigue damages, validated the CFD method through comparisons to the published experimental data and/or the results calculated using other commercial software tools, and disclosed interesting phenomena associated with long riser VIV. Some highlights of the findings are as follows:

1. The CFD time domain simulation predicted a narrow wake field and a high-speed zone outside the wake field. This finding has a potential interest for deepwater riser system design since it could reduce the design conservatism during riser interference design.
2. The vortex shedding pattern in the shear current is different from that of the uniform current. In the uniform current case, the riser motion and vortex shedding are usually synchronized. In the shear current case, the mixture of 2S and C patterns suggested the existence of power-in and power-out zones along the riser. And it also provided a criterion to partition these two zones based on the flow pattern.
3. Mode lock-in occurred in both the uniform current and the shear current. However, the lock-in mode's dominant level (in terms of the energy percentage) varied in a large range. And it tends to be higher in uniform current, and lower in shear current.

4. The asymmetry of the riser VIV response in the uniform current suggested that the cross flow VIV was influenced by the in-line riser motion. Good correlation was identified between the in-line riser motion and the asymmetry level along the riser. The existence of the non-dominant modes in cross flow VIV also contributed to the asymmetry.
5. Strong shear current tends to excite more modes. The dominant mode contributed most to the VIV induced fatigue, while the non-dominant modes also influenced the fatigue damage considerably by enhancing or cancelling the peak stresses. The fatigue distribution also showed asymmetry along the riser due to the same reasons as in (4).
6. Higher harmonics have been observed in the CFD simulations. It is found that the 3x higher harmonics was mainly due to the high frequency components of the lift force, which is directly related to the vortex shedding pattern. This finding provides physical explanation to the existence of higher harmonics, and an option to assess its impact on the riser fatigue and possible mitigation methods.
7. The CFD simulation results on a long marine riser confirmed that the maximum VIV response was near the riser bottom, where the effective tension was the lowest. This phenomenon is independent of the current profiles. In other words, the bottom of a top tensioned riser always has the maximum VIV response regardless of the current force action points.

8. The flexible catenary riser VIV response was complicated by its low tension near its vertex region, where its effective tension approaches zero. In this region the riser lateral deflection is large, and could be in the order of 100D, which is two-order of magnitude higher than the cross flow VIV amplitude (in the order of 1D). Slight change of the drag force is equivalent to relocate the riser to a new equilibrium position, and consequently introduces transient dynamics and influences the cross flow VIV response. The simulation results showed that the catenary riser motion trajectories did not follow simple and regular patterns. It also showed that the catenary riser VIV could have two or more modes excited with similar strength (multi-modal).

CFD simulation of the long riser VIV is a relatively new research area. And there are too many unknowns and interesting areas to be further investigated, such as riser high mode VIV under strong current and high Reynolds number, VIV suppression devices including fairings and strakes, deepwater riser non-linear damping effect on VIV, and riser VIV in complex current conditions including submerged current or bottom current. The present CFD approach could also be further improved in following areas:

1. The data grid total element number was limited to 1.5 million for practical considerations including computational time and storage space. This would allow the CFD be carried out by a single-process PC within reasonable time frame. This limitation could be removed by using parallel computation technique on a multi-processor cluster. The refined data grid with high

resolution in riser spanwise will provide more insights to the rise spanwise vortex shedding details, and more accurate simulation for high Reynolds number current flow and high mode riser VIV.

2. The riser direct integration solver was based on a finite difference scheme with accuracy of $O(h^2)$ in space and $O(\tau)$ in time. The accuracy order could be improved by adding more terms to the finite difference scheme.
3. The riser motion solvers were extended to handle the catenary riser dynamics through a linearized approach, which requires only a static catenary shape as the initial condition. A catenary riser dynamic motion solver could be developed to expand the CFD approach's capability to strong non-linear riser dynamics.
4. The riser motion solver and the fluid field solver are weakly coupled in the present CFD approach, i.e. the riser motions and the fluid dynamics were solved separately and coupled through an explicit and forward marching method. Iteration between the riser motion and fluid field could be introduced to improve the overall simulation stability.

In conclusion, a three dimensional CFD approach for deepwater riser VIV simulation with different riser motion solvers has been presented. The long riser VIV response is based on the unsteady, incompressible Navier-Stokes equations in conjunction with a large eddy simulation (LES) model. And its validity and effectiveness to predict long riser VIV in uniform and shear current have been demonstrated through case studies and comparisons to the published experimental data.

REFERENCES

ASME B 31.4, 2002, “Pipeline Transportation Systems for Liquid Hydrocarbon and Other Liquids”, 2002 Edition, August, 2002.

ASME B 31.8a, 2001, “Gas Transmission and Distribution Piping Systems”, 2001 Edition, November, 2001.

API RP 1111, 1999, "Design, Construction, Operation, and Maintenance of Offshore Hydrocarbon Pipelines", 3rd Edition, July, 1999.

API RP 2RD, 1998, “Design of Risers for Floating Production Systems (FPSs) and Tension-Leg Platforms (TLPs)”, June, 1998

API Specification 5L, 2000, "Specification for Line Pipe", 42nd Edition, January, 2000.

API Bulletin 5C3, 1994, “Bulletin on Formulas and Calculations for Casing, Tubing, Drill Pipe, and Line Pipe Properties”, 6th Edition, November, 1994

Blevins, R.D., 1990, Flow-Induced Vibrations, Second Edition. Van Nostrand Reinhold.

Chen,.H.C., Patel, V.C., 1988, “Near-wall turbulence models for complex flows including separation,” AIAA Journal, Vol 26, pp 641-648.

Chen, H.C., Patel, V.C. 1989, “The Flow around Wing-Body Junctions,” Proceedings of the 4th Symposium on Numerical and Physical Aspects of Aerodynamic Flows, Long Beach, CA, 16-19 January.

Chen, H.C., Patel, V.C. and Ju, S., 1990, "Solutions of Reynolds-Averaged Navier-Stokes Equations for Three-Dimensional Incompressible Flows," Journal of Computational Physics, Vol. 88, No. 2, pp. 305-336.

Chen, H.C., Chen, C.R., Mercier, R., Pontaza, J.P., 2006, "CFD Simulation of Riser VIV", MMS and OTRC Project Report 32558/22820/CE & 32558/2282A/SC, October, 2006.

Chen, Z.S. Kim, W.J., 2010, "Numerical Study of Vortex-Induced Vibration for Flexible Riser and Pipe Models," Proceedings of the 20th International Offshore and Polar Engineering (ISOPE) Conference, Beijing, China, June 2010.

Chaplin, J.R., Bearman, P.W., Cheng, Y., Fontaine, E., Graham, J.M.R., Herfjord, K., Huera, F.J., Isherwood, M., Lambrakos, K., Larsen, C.M., Meneghini, J.R., Moe, G., Pattenden, R.J., Triantafyllou, M.S., Willden, R.H.J. 2005, "Blind Prediction of Laboratory Measurements of Vortex-Induced Vibrations of a Tension Riser," Journal of Fluids and Structures 21,pp. 25-40.

Constantinides, Y., Oakley, O.H., 2008a, "Numerical Prediction of VIV and Comparison with Field Experiments," Proceedings of the ASME 27th International Conference on Offshore Mechanics and Arctic Engineering (OMAE), Estoril, Portugal.

Constantinides, Y., Oakley, O.H., 2008b, "Assessment of Empirical VIV Analysis Tools and Benchmark with Experiments," Proceedings of the ASME 27th International Conference on Offshore Mechanics and Arctic Engineering (OMAE), Estoril, Portugal.

Holmes, S., Oakley, O.H., Constantinides, H. 2006, "Simulation of Riser VIV Using Fully Three Dimensional CFD Simulations," OMAE 2006-92124, 25th International Conference on Offshore Mechanics and Artic Engineering, Hamburg, Germany.

Huang, K. and Chen, H.C., 2006, Ultra Deepwater Riser Interference Analysis by Using a Time Domain Simulation Approach with VIV Effect, Proceedings of D.O.T XVIII (2006) Conference, Houston, TX, November 2006.

Huang, K. Chen, H.C., Chen, C.R., 2007a, "Deepwater Riser VIV Assessment by Using A Time Domain Simulation Approach," Proceedings of the Offshore Technology Conference, OTC 18769, Houston, TX, May 2007.

Huang, K. Chen, H.C., Chen, C.R., 2007b, "Riser VIV Analysis by a CFD Approach," Proceedings of the 17th International Offshore and Polar Engineering (ISOPE) Conference, Lisbon, Portugal, July 2007.

Huang, K., Chen, H.C., Chen, C.R., 2007c, "Time-Domain Simulation of Riser VIV in Shear Current," Proceedings of 26th International Conference on Offshore Mechanics and Arctic Engineering (OMAE) Conference, OMAE 29363, San Diego, California, June 2007.

Huang, K., Chen, H.C., Chen, C.R., 2007d, "A Three Dimensional CFD Approach for Deepwater riser VIV Simulation," Proceedings of 9th International Symposium on Fluid Control, Measurement and Visualization (FLUCOME), Tallahassee, Florida, September 2007.

Huang, K. Chen, H.C., Chen, C.R., 2008, "Riser VIV Induced Fatigue Assessment by a CFD Approach," Proceedings of the 18th International Offshore and Polar Engineering (ISOPE) Conference, Vancouver, Canada, July 2008.

Huang, K. Chen, H.C., Chen, C.R., 2009a, "Vertical Riser VIV Simulation in Shear Current," Proceedings of the 19th International Offshore and Polar Engineering (ISOPE) Conference, Osaka, Japan, July 2009.

Huang, K., Chen, H.C., Chen, C.R., 2009b, "Vertical Riser VIV Simulation in Uniform Current," Proceedings of 28th International Conference on Offshore Mechanics and Arctic Engineering (OMAE) Conference, OMAE 79349, Honolulu, Hawaii, June 2009.

Huang, K. Chen, H.C., Chen, C.R., 2010, "Flexible Catenary Riser VIV Simulation in Uniform Current," Proceedings of the 20th International Offshore and Polar Engineering (ISOPE) Conference, Beijing, China, June 2010.

Huang, K. Chen, H.C., Chen, C.R., 2011, "Flexible Catenary Riser VIV Simulation in Uniform Current," Proceedings of the 21th International Offshore and Polar Engineering (ISOPE) Conference, Hawaii, USA, June 2011.

Huse, E., 1993, Interaction in Deep Sea Riser Arrays, Proc. Of Offshore Technology Conference, OTC paper 7237, Houston, TX, May 1993.

Huse, E., 1996, "Experimental Investigation of Deep Sea Riser Interaction," Proc. Of Offshore Technology Conference, OTC paper 8070, Houston, TX, May 1996.

Jhingran, V., Jaiswal, V., Vandiver, J.K., 2008, "Spatial Variation of Drag on Long Cylinders in Shear Flow," Proceedings of the ASME 27th International Conference on Offshore Mechanics and Arctic Engineering (OMAE), Estoril, Portugal.

Lucor, D. Imas, L., Karniadakis, G.E., 2000, "Vortex Dislocations and Force Distribution of Long Flexible Cylinders Subjected to Sheared Flows," Journal of Fluids and Structures, Vol 15, pp 641-650.

Lucor, D. Mukundan, H, Triantafyllou, M.S., 2006, "Riser Modal Identification in CFD and full-scale Experiments," Journal of Fluids and Structures, Vol 22, pp 905-917.

Meneghini, J.R., Saltara, F., Fregonesi, R.A., Yamamoto, C.T., Casaprima, E., Ferrari, J.A., 2004, "Numerical Simulations of VIV on Long Flexible Cylinders Immersed in Complex Flow Fields," European Journal of Mechanics B/Fluids, Vol 23, pp 51-63.

Newman, D., Karniadakis, G.E., 1996, "Simulations of Flow Over a Flexible Cable: A Comparison of Forced and Flow-Induced Vibration," Journal of Fluids and Structures, Vol 10, pp 439-453.

Pontaza, J.P., Chen, C.R., Chen, H.C., 2004, "Chimera Reynolds-averaged Navier-Stokes simulations of vortex-induced vibration of circular cylinders," Proceedings of the International ASCE Conference: Civil Engineering in the Oceans VI, pp 166-176.

Pontaza, J.P., Chen, C.R., Chen, H.C., 2005a, "Simulations of high Reynolds number flow past arrays of circular cylinders undergoing vortex-induced vibrations," Proceedings of the 15th International Offshore and Polar Engineering (ISOPE) Conference, pp 201-207.

Pontaza, J.P., Chen, H.C., Chen, C.R., 2005b, "Numerical simulations of riser vortex-induced vibrations," Proceedings of the 2005 Society of Marine Engineers and Naval Architects (SNAME) Conference, D52, pp 1-12.

Pontaza, J.P., Chen, H.C., Reddy, J.N., 2005c, "A local-analytic-based discretization procedure for the numerical solution of incompressible flows," International Journal for Numerical Methods in Fluids Vol 49, pp 657-699.

Pontaza, J.P., Chen, H.C., 2006, "Three-dimensional numerical simulations of circular cylinders undergoing two degree-of-freedom vortex-induced vibrations," OMAE 2006-92052, 25th International Conference on Offshore Mechanics and Artic Engineering, Hamburg, Germany.

Pontaza, J.P., Menon, R.G. and Chen, H.C., "Three-Dimensional Numerical Simulations of Flow Past Smooth and Rough/Bare and Helically Straked Circular Cylinders, Allowed to Undergo Two Degree-of-Freedom Motions," OMAE 2007-29366, Proceedings of 26th International Conference on Offshore Mechanics and Artic Engineering, June 10-15, 2007, San Diego, California, USA.

Pontaza, J.P., Chen, H.C., "Three-Dimensional Numerical Simulations of Circular Cylinders Undergoing Two Degree-of-Freedom Vortex-Induced Vibration," ASME Journal of Offshore Mechanics and Artic Engineering, Vol. 129, No. 3, pp. 158-164, August 2007.

Tognarelli, M.A., Slocum, S.T., Frank, W.R., Campbell, R.B. 2004, "VIV Response of a Long Flexible Cylinder in Uniform and Linearly Shear Currents," Proceedings of the Offshore Technology Conference, OTC 16338, Houston, TX, May 2004.

Tognarelli, M.A., Taggart, S., Campbell, M., 2008, "Actual VIV Fatigue Response of Full Scale Drilling Risers: With and Without Suppression Devices," Proceedings of the ASME 27th International Conference on Offshore Mechanics and Arctic Engineering (OMAE), Estoril, Portugal.

Trim, A.D., Braaten, H., Lie, H., Tognarelli, M.A., 2005, "Experimental investigation of vortex-induced vibration of long marine risers," Iournal of Fluids and Structures, Vol 21, pp 335-361.

Willden, R.H.J., Graham, J.M.R, 2001, "Numerical Prediction of VIV on Long Flexible Circular Cylinders," Journal of Fluids and Structures, Vol 15, pp 659-669.

Willden, R.H.J., Graham, J.M.R, 2004, "Multi-modal Vortex-Induced Vibrations of a Vertical Riser Pipe Subject to a Uniform Current Profile," European Journal of Mechanics B/Fluids, Vol 23, pp 209-218.

Williamson, C.H.K., Roshko, A., 1988, "Vortex Formation in the Wake of an Oscillating Cylinder," European Journal of Mechanics B/Fluids, Vol 2, pp 355-381.

Williamson, C.H.K., Jauvtis, N., 2004, "A High-amplitude 2T Mode of Vortex-Induced Vibration for a Light Body in XY Motion," European Journal of Mechanics B/Fluids, Vol 23, pp 107-114.

Vandiver, J.K., 1993, "Dimensionless Parameters Important to the Prediction of Vortex-Induced Vibration of Long, Flexible Cylinders in Ocean Currents," Journal of Fluids and Structures, Vol 7, pp 423-455.

Vandiver, J.K., Li, L., 2003, "Shear7 V4.3 Program Theoretical Manual," September 2003.

Yamamoto, C.T., Meneghini, J.R., Saltara, F., Fregonesi, R.A., Ferrari, J.A., 2004, "Numerical Simulations of Vortex-Induced Vibration on Flexible Cylinders," Journal of Fluids and Structures, Vol 19, pp 467-489.

APPENDIX A

This appendix documents the results during the riser motion solver integration to the parallel fluid solver.

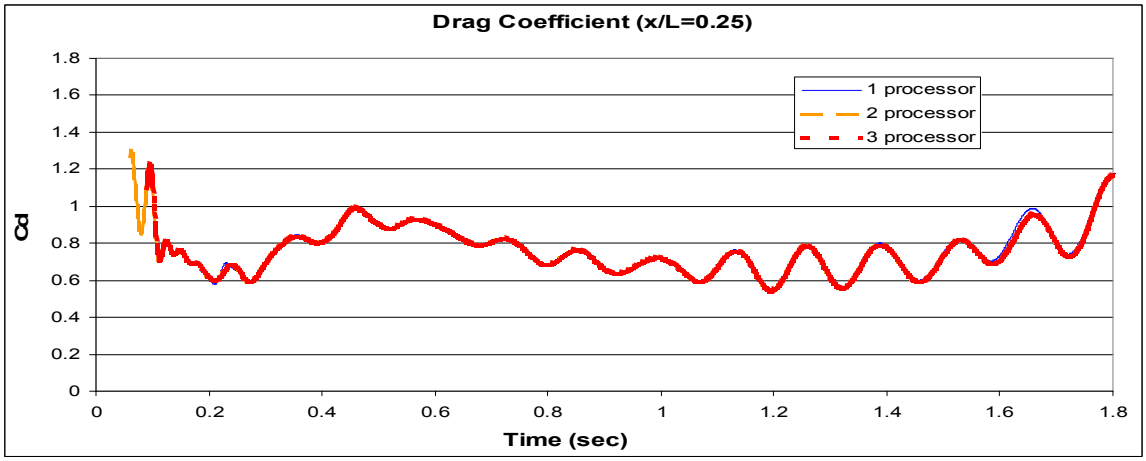

Fig. 128 Drag Coefficient Time History Comparison

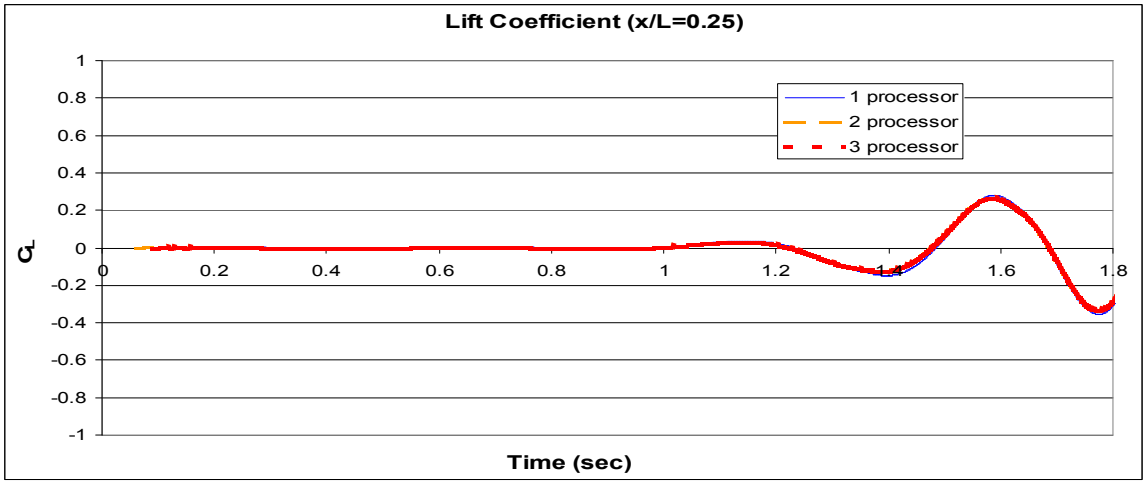

Fig. 129 Lift Coefficient Time History Comparison

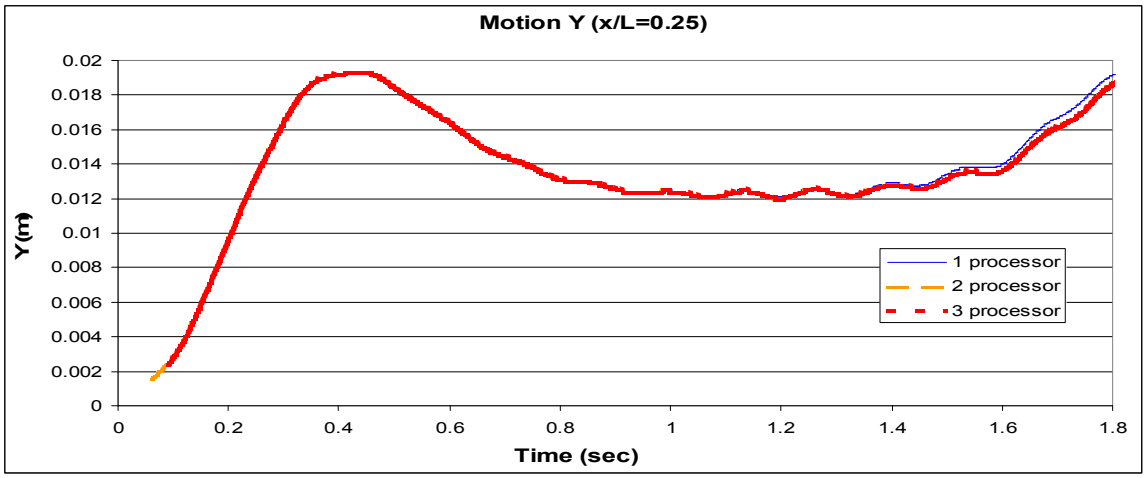

Fig. 130 Motion Y Time History Comparison

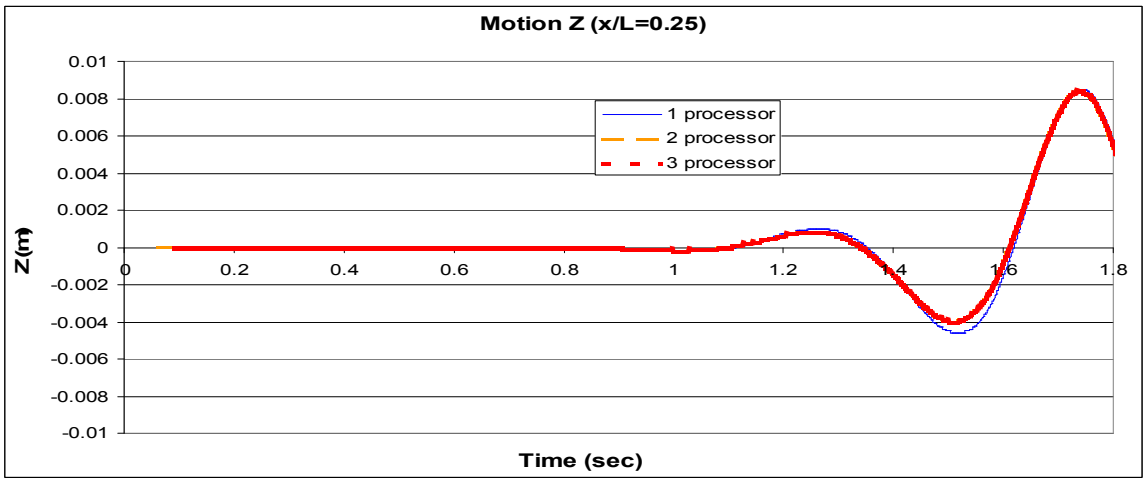

Fig. 131 Motion Z Time History Comparison

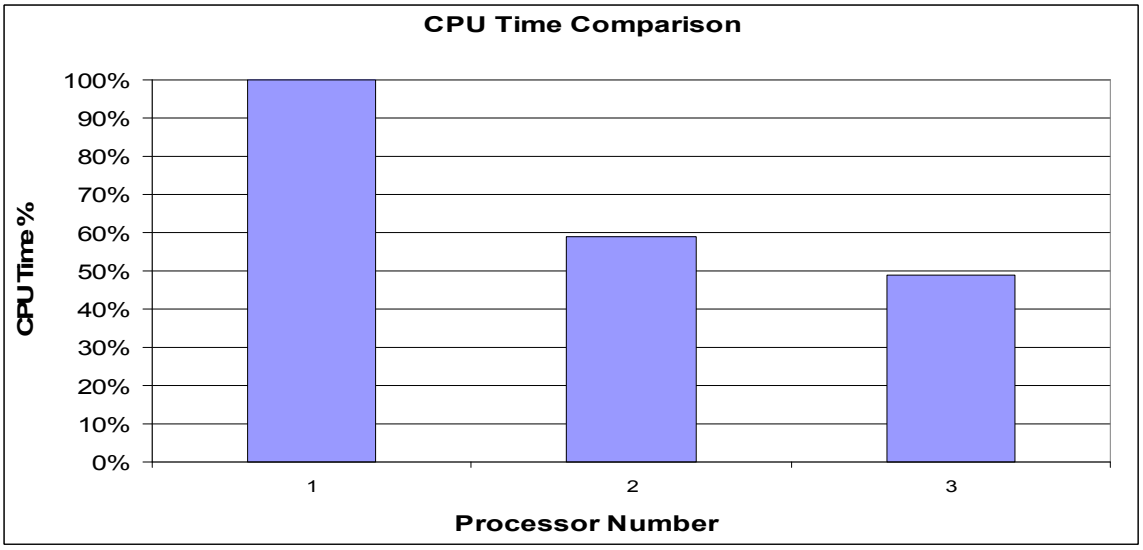

Fig. 132 Normalized Computational Time

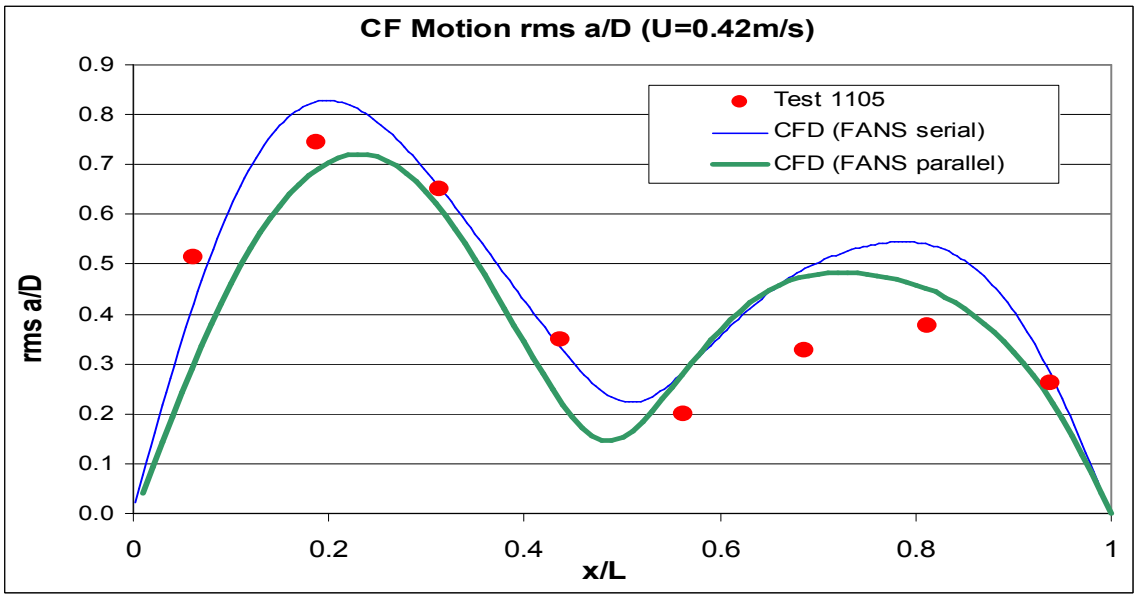

Fig. 133 Cross Flow rms a/D comparison

VITA

Zhiming Huang received his Bachelor of Science degree in thermal engineering from Tsinghua University in Beijing in 1994. He entered the Civil Engineering program at University of Houston in May 1996 and received his Master of Science degree in May 1998. He has more than 10 years experience in the oil and gas industry, and his research interests which include offshore floating platform hydrodynamics, deepwater riser vortex induced vibrations (VIV), and CFD simulations of fluid-structure interaction.

Mr. Huang may be reached at KevinHuang_01@hotmail.com, or at mail address: Department of Civil Engineering, Texas A&M University, 3136 TAMU, College Station, Texas 77843-3136, USA.